THE UNIVERSITY OF QUEENSLAND
AUSTRALIA

Mathematical Modelling of Axon Guidance in Chemical Gradients

BY

HUYEN THANH NGUYEN

Bachelor of Science (Hons) in Physics

A thesis submitted for the degree of Doctor of Philosophy

at The University of Queensland in 2015

Queensland Brain Institute

Abstract

Correct wiring is crucial to the proper functioning of the nervous system. Key signals guiding growth cones, the motile tips of developing axons, to their targets are molecular gradients. The receptors on the membrane of the growth cone bind stochastically with guidance molecules in the environment, giving an estimate of the direction of the gradient. The growth cone then executes biased random movements to navigate toward the chemoattractant source or away from the chemorepellent source. This thesis addresses two questions: 1) how the positioning and diffusion of receptors on the growth cone membrane affect the accuracy of gradient estimation, 2) how trajectories are influenced by chemical gradients.

Membrane receptors can diffuse freely on the membrane, smearing out the directional information about the gradient. It was unknown how the positioning and diffusion of receptors affect the estimate of the gradient. To address question (1) above, we utilise an ideal-observer approach, assuming that the growth cone can perform maximum likelihood estimation of the gradient based on the stochastic binding patterns with ligand molecules. The performance of gradient sensing is measured by the Fisher Information between the binding pattern and the gradient direction. The quality of gradient sensing decreases with higher diffusion constant of the receptors and improves with higher concentration. We then extend to a two-dimensional model of an elliptical growth cone with a general prior distribution. With a random uniform distribution of receptors, the shape of the growth cone can introduce bias in the gradient estimate. This bias can be corrected by a non-uniform distribution of receptors with higher density near the minor axis of the growth cone.

Besides stochastic gradient sensing, growth cones also trace highly stochastic trajectories, and it is unclear how molecular gradients bias their movement. We then introduce a mathematical model of a correlated random walk based on persistence, bias and noise to describe growth cone trajectories, constrained directly by measurements of the detailed statistics of growth cone movements in both attractive and repulsive gradients in a microfluidic device. This model explains the long-standing mystery that average axon turning angles in gradients *in vitro* plateau very rapidly with time at relatively small values of 10-20°. This work introduces the most accurate predictive model of growth cone trajectories to date, and calls into question the ability of molecular gradients alone to provide reliable guidance cues for growing axons.

Declaration by Author

This thesis is composed of my original work, and contains no material previously published or written by another person except where due reference has been made in the text. I have clearly stated the contribution by others to jointly-authored works that I have included in my thesis.

I have clearly stated the contribution of others to my thesis as a whole, including statistical assistance, survey design, data analysis, significant technical procedures, professional editorial advice, and any other original research work used or reported in my thesis. The content of my thesis is the result of work I have carried out since the commencement of my research higher degree candidature and does not include a substantial part of work that has been submitted to qualify for the award of any other degree or diploma in any university or other tertiary institution. I have clearly stated which parts of my thesis, if any, have been submitted to qualify for another award.

I acknowledge that an electronic copy of my thesis must be lodged with the University Library and, subject to the policy and procedures of The University of Queensland, the thesis be made available for research and study in accordance with the Copyright Act 1968 unless a period of embargo has been approved by the Dean of the Graduate School.

I acknowledge that copyright of all material contained in my thesis resides with the copyright holder(s) of that material. Where appropriate I have obtained copyright permission from the copyright holder to reproduce material in this thesis.

Publications during candidature

1) J. Yuan, S. Chan, D. Mortimer, **H. Nguyen**, G.J. Goodhill, "Optimality and saturation in axonal chemotaxis," *Neural Computation*, vol 25, no. 4, pp. 833-53, 2013.

2) **H. Nguyen**, P. Dayan, G.J. Goodhill, "How Receptor Diffusion Influences Gradient Sensing," *Journal of Royal Society Interface*, vol 12: 20141097, 2015. DOI: 10.1098/rsif.2014.1097

3) **H. Nguyen**, P. Dayan, G.J. Goodhill, "The Influence of Receptor Positioning on Chemotactic Information," *Journal of Theoretical Biology*, vol 360, pp. 95-101, 2014.

4) Z. Pujic, **H. Nguyen**, N. Glass, J. Cooper-White, G.J. Goodhill, (in press) "Axon guidance studies using a microfluidics-based chemotropic gradient generator," in *Chemotaxis: Methods and Protocols (Methods in Molecular Biology)* (T. Jin and D. Hereld, ed.), Springer.

5) **H. Nguyen**, P. Dayan, Z. Pujic, J. Cooper-White, G.J. Goodhill, "A mathematical model explains saturating axon guidance responses to molecular gradients" resubmitted to eLife.

Publications included in this thesis

Publication 2 - incorporated as Chapter 3

Contributor	Statement of contribution
H. Nguyen	Designed research (80%) Performed research (80%) Wrote the paper (60%)
P. Dayan	Designed research (10%) Performed Research (10%) Wrote the paper (20%)
G.J. Goodhill	Designed research (10%) Performed Research (10%) Wrote the paper (20%)

Publication 3 - incorporated as Chapter 4

Contributor	Statement of contribution
H. Nguyen	Designed research (20%) Performed research (70%) Wrote the paper (60%)
P. Dayan	Designed research (40%) Performed Research (15%) Wrote the paper (20%)
G.J. Goodhill	Designed research (40%) Performed research (15%) Wrote the paper (20%)

Publication 4 - incorporated as Chapter 5

Contributor	Statement of contribution
Z. Pujic	Performed Experiments (20%) Wrote the paper (80%) Designed research (20%)
H. Nguyen	Performed experiments (70%) Analysed data (100%) Wrote the paper (10%) Designed research (20%)
N. Glass	Performed Experiments (10%)
J. Cooper-White	Designed research (30%)
G.J. Goodhill	Wrote the paper (10%) Designed research (30%)

Publication 5 - incorporated as Chapter 6

Contributor	Statement of contribution
H. Nguyen	Performed experiments (100%) Analysed data (80%) Wrote the paper (60%) Designed research (40%)
P. Dayan	Wrote the paper (20%) Analysed data (20%) Designed research (10%)
Z. Pujic	Designed research (10%)
J. Cooper-White	Designed research (10%)
G.J. Goodhill	Wrote the paper (20%) Designed research (30%)

Contributions by others to the thesis

None

Statement of parts of the thesis submitted to qualify for the award of another degree

None

Acknowledgements

I would like to thank all the wonderful people who have helped and supported me during my PhD. In particular, I would like to thank my primary supervisor, Professor Geoff Goodhill for his intellectual support, patience, encouragement over the years and the many opportunities he gave me. To my associate advisor, Professor Peter Dayan, I would like to thank you for your many insightful questions and suggestions, for your patient and dedicated support and the wonderful time I had at the Gatsby Unit of Computational Neuroscience.

To Zac Pujic, for being a truly inspiring and supportive mentor in my lab work showing me what it is like to be a real biologist. I appreciated all the times you were willing to give me remote guidance at the odd hours in the lab, your unique sense of humour and the many very interesting discussions we have had about science and everything else.

To Lilach Avitan and Natalie Lee, the two best friends I have at QBI, you are my role models and have given me invaluable personal support and inspiration. I admire your determination, unwavering optimism and tenacity. To other members of the Goodhill Lab: Beth Kita, Nick Hughes, Brendan Bicknell, Biao Sun and Pranesh Padmanabhan and our collaborators the Cooper-White Lab for your friendship and technical support.

To my parents and family, I feel deeply grateful for letting me pursue further study in a field you do not understand and respecting my choice and freedom. Your encouragement and support for my academic pursuit has been wonderful.

I am thankful for all the people at QBI who have made it a stimulating and comfortable environment to work, where I have been exposed to many interesting ideas and the fascinating progress of the field.

I am thankful to V.S. Ramachandran whose book ”Phantoms in the Brain” sparked my interest in the fascinating field of neuroscience and started me on this journey.

This work was made possible through a UQ Internatiional Postgraduate Scholarship.

Key words

Growth cone, Axon guidance, Gradient sensing, Bayesian inference, Microfluidics.

Australian and New Zealand Standard Research Classifications (ANZSRC)

110905, Peripheral nervous system, 40%

010202 Biological Mathematics 60%

Fields of Research (FoR) Classification

1109 Neuroscience 40%

0102 Applied Mathematics 60%

Contents

List of Figures

Abbreviations

APTES	(3-Aminopropyl)triethoxysilane
CaM	calmodulin
CaMKII	calmodulin-dependent protein kinase II
cAMP	cyclic adenosine monophosphate
cAR1	cAMP Receptor
CICR	calcium-induced calcium release
CN	calcineurin
CNS	central nervous system
DRG	dorsal root ganglia
ECM	extracellular matrix
EGFR	epidermal growth factor receptor
FI	Fisher Information
H	High solution
IgG	Immunoglobulin G
IICR	InsP3R-induced calcium release
$InsP_3$	inositol-1,4,5 -triphosphate
kDA	kilodalton
K_D	dissociation constant
L	Low solution
MAP	maximum a posteriori
MGM	microfluidic growing medium
MLE	maximum likelihood estimate
MSD	mean square displacement
mRNAs	messenger RNAs

μM	micromolar
μL	microlitre
mL	millilitre
NGF	nerve growth factor
nM	nanomolar
nL	nanolitre
NT-3	neurotrophin-3
P	postnatal
PBS	phosphate buffered saline
PDMS	polydimethylsiloxane
PDGF	platelet-derived growth factor
PKA	protein kinase A
PNS	peripheral nervous system
PS	Penicillin-Streptomycin
RCF	relative centrifugal force
Trk	tropomyosin-related kinase
SCG	superior cervical ganglia
SNR	signal-to-noise ratio
TCP	tissue culture plate

Symbols

T	time	s
r_-	off-rate	s^{-1}
r_+	on-rate	s^{-1}
K_D	Dissociation constant	Molar
C	Concentration	Molar
N	Number of receptors	No unit
T^U	Unbound time	s
T^B	Bound time	s
D	Diffusion constant	m^2s^{-1}
R	Growth cone radius	m
s	Magnitude of gradient	1/m
$\vec{r}$	Position of receptor	m
S	Straightness index	No unit
θ	Heading direction	Rad
ϕ	Growth cone angle	Rad
$\Delta\theta$	Bearing change	Rad
ξ	Noise in bearing change	Rad
γ	Normalised concentration	No unit
μ	Dimensionless gradient	No unit
$\mathcal{L}$	Likelihood function	
$\mathcal{I}$	Fisher Information	
$\text{argmax} f(x)$	the value of x for which $f(x)$ is maximised	

Chapter 1

Introduction

The brain is an extraordinarily complex organ that consists of billions of neurons, many of which connect with thousands of others. Brain function relies critically on the correct wiring among neurons during early development. Axon guidance is the process by which neurons extend axons to each other, to muscles and to glands – their synaptic partners. Extracellular molecular cues are the critical signals that initially direct axons to their targets before synaptic connections can be established and refined [1–3]. One of the key signals is molecular gradients, i.e. graded distributions of guidance cues that attract or repel axons. This thesis is concerned with axon guidance by chemotaxis - the process in which axons follow molecular gradients to navigate in the environment to reach their synaptic targets.

Chemotaxis is a widespread fundamental biological process commonly shared by many organisms [4–7]. There are two mechanisms for detecting gradients: temporal and spatial sensing. Organisms employing temporal sensing compare the concentration over time as they move in the concentration field. Meanwhile, spatial sensing entails detecting differences in receptor occupancy across the organism's surface [6]. The external gradient of ligand molecules, through asymmetric activation of membrane receptors, is translated into an intracellular gradient of signalling molecules, which eventually leads to movement. Due to the inherently stochastic nature of ligand-receptor interaction, the receptor signal is noisy. Chapters 3 and 4 in this thesis address the question of the upper limits of spatial gradient sensing.

1.1 Significance

Understanding axon guidance is of great clinical interest for several reasons. On the one hand, defective axon guidance can lead to aberrant connectivity and is believed to result in major brain disorders [8]. For example, loss of function mutations in the axon guidance receptor Robo3 leads to axonal midline crossing defects that underlie horizontal gaze palsy with progressive scoliosis (HGPPS), a rare brain disorder [9]. Indirectly, mutations in guidance receptor genes or misregulation of guidance cues have been associated with many neurological disorders such as Parkinson's disease, autism, dyslexia and schizophrenia [10–13]. The causative links between the molecular mechanisms that underlie abnormal connectivity and brain disorders are immensely complex and poorly understood. Understanding axon guidance in normal development will provide insight into how axonal miswiring might cause disease, that will help the development of therapeutic treatment of brain disorders.

On the other hand, one of the most fundamental questions in neurobiology is understanding mechanisms underlying the success of regeneration in the peripheral nervous system (PNS) and the failure in the central nervous system (CNS) to promote regeneration after injury. Axon guidance molecules play a complicated role in the central nervous system after injury, such as promoting and inhibiting axon regeneration, modulating astrogliosis and tissue response to injury [10]. Ultimately, it is hoped that the knowledge gained in understanding axon guidance *in vivo* and *in vitro* will be utilised to encourage proper axon regeneration after injury.

1.2 Growth cones

A highly motile, complex structure called the growth cone is the navigator at the distal tip of an extending neurite which will later mature into an axon or a dendrite. The growth cone explores the molecular landscape, interprets extracellular signals and implements motility in the appropriate direction. The motility process starts when signal molecules bind to receptors, triggering downstream signalling events, leading the growth cone to rearrange its cytoskeletal components and change direction [2].

Growth cones share many similar behaviours with many chemotactic eukaryotic cells, such as leukocytes accumulating in an inflammatory response, and the slime mould *Dictyostelium* aggregating toward a cAMP source [5, 6, 14, 15]. Growth cones and eukaryotic cells also share the major signal transduction pathways [16]. However, because growth cones are tethered to the cell by the axon, their movements have some unique characteristics. Some of the models applied to growth cones and other eukaryotic cells will be reviewed in this thesis.

1.3 The role of mathematical modelling in understanding axon guidance

A tool that has been useful in expanding our understanding of eukaryotic and growth cone chemotaxis is mathematical modelling. For example, the understanding of *Dictyostelium* and leukocyte chemotaxis has become strikingly quantitative, with detailed hypotheses being tested thanks to a fruitful interaction between theory and experimentation (e.g. [17–21]). Quantitative modelling forces precise hypotheses instead of possibly vague qualitative predictions [22]. Mathematical models can potentially capture complex phenomena by relatively simple equations and allow a thorough examination of the consequences of particular assumptions, leading to new insights and clarity [19, 22].

In the context of axon guidance, although much is known about the molecular mechanisms of growth cone chemotaxis, the computational principles are still lacking. It is critical to understand axon guidance quantitatively to determine the limits of guidance due to gradients. This quantitative understanding will help predict the quality of guidance *in vivo* under normal and abnormal conditions and contribute to the ability to optimise applied gradients for promoting nerve regeneration. This thesis aims to investigate the constraints on gradient sensing and guidance. We divide the thesis into two parts: the ultimate limits imposed by the physical properties of receptors and the limits due to growth cone motility noise and tension. The *in vitro* data give us insight into whether gradients alone are sufficient to guide axons *in vivo* or what other factors might be needed for reliable guidance.

In the first half, the growth cone is modelled as an abstract idealised ‘sensing device’. This analysis of gradient sensing can be validly applied to other chemotactic cells. The state of the environment is never 100% certain to the growth cone. The best it can do is to assign probabilities to different possible states of the environment conditioned on the sensory information it receives. We treat gradient sensing as a Bayesian inference problem: in this context, given a noisy signal that is the binding pattern, the growth cone has to infer the direction of the gradient. The positioning and movement of its ‘sensors’, the membrane receptors, can have an effect on the accuracy of this inference process. In contrast, the growth cone’s movement has unique characteristics not present in other systems, most importantly the constraint by mechanical tension generated by the axon. In this thesis, we will address the following topics:

- In chapter 2, we review of the current understanding of the growth cone, the inference framework of gradient sensing, models of growth cone motility and existing axon guidance assays for investigating such questions.

- In chapter 3, we present an abstract model of gradient sensing by maximum likelihood estimation by a one-dimensional growth cone with receptors that can freely diffuse on its surface. We provide an analysis of how the random movements of receptors can affect the quality of gradient sensing.

- In chapter 4, we extend the previous model to a two-dimensional model of a sensing device that has some prior information about the gradient. We then apply a Bayesian analysis to investigate the role of receptor positioning on computing the posterior distribution of the gradient.

- In chapter 5, we next introduce a new axon guidance assay that allows us to observe multiple cells simultaneously over an extended period of time. We characterise the gradient and the guidance responses of superior cervical ganglion axons to nerve growth factor (NGF) gradients. This forms the basis for the next chapter.

- In chapter 6, we analyse the trajectories of growth cones in NGF gradients and develop a phenomenological model to describe their trajectories. We explain why *in vitro*, turning response saturates very quickly with time at small values and offer some new hypotheses about *in vivo* guidance.

Overall, the thesis provides insights into the physical limits of sensing from receptor-ligand binding that are applicable to all eukaryotic chemotactic systems and proposes the critical requirements of substrate adhesion and small motility noise for reliable turning *in vivo*. It provides a unifying explanation for the general phenomenon of weak turning in many qualitative *in vitro* studies and stimulates new ideas to gain a deeper understanding of axon guidance.

Chapter 2

Literature Review

At the tip of a growing axon or dendrite is a highly motile, complex structure called the growth cone, which senses the environment and implements motility. In this chapter we will briefly review the current knowledge of growth cone chemotaxis and the relevant culture assays and mathematical models that will help us gain a deeper understanding of gradient sensing and motility.

2.1 Growth cones and nervous system development

2.1.1 The chemotropic hypothesis of axon guidance

The neuroscientist Santiago Ramon y Cajal discovered growth cones in his studies of embryos and published the first histological staining images of them in 1890 [23]. In 1910, Ross Harrison made the landmark finding that neurons can be cultured outside the body and observed the first living growth cones in tissue culture [23]. Images of live growth cones *in vivo* were first reported by Carl Speidel in 1933 [24].

Cajal proposed the prescient ‘chemotropic hypothesis’ that growth cones lead the way for axons to navigate through the embryo in response to attractants to reach their targets. In contrast, *in vitro* studies led Paul Weiss to propose the ‘contact guidance’ hypothesis, which stipulates that what is important in axon guidance is the mechanical properties of the local environment of the growing axon [25]. Due to the lack of direct evidence, the chemotropic hypothesis languished until the 1960s when Roger Sperry revived the research into chemical guidance of growing and regenerating axons [26]. He proposed that axons carry chemical tags that match them with the target neurons with specific affinities. Based on his insightful experiments in frogs, he also hypothesised the existence of gradients of chemical signals that explained the topographic projection of retinal axons into the tectum [26].

In the 1980s, Andrew Lumsden and Alun Davies discovered a target-derived signal from the whisker pad epithelium of mice that elicited and attracted the growth of neurites from innervating trigeminal sensory neurons, a finding that lent support to the chemotropic hypothesis [27]. Advances in biochemistry, molecular biology and studies of embryonic tissue *in vitro* and *in vivo* led to the first discovery of truly chemotropic molecules. Tessier-Lavigne and colleagues detected diffusible signals in the floor plate of chick embryos that attracted commissural axons and later identified them as netrins [28, 29]. These findings have inspired a rapid expansion of understanding of axon guidance that followed in recent decades.

2.1.2 The structure and dynamics of growth cones

In order to understand axonal chemotaxis, we first summarise key knowledge of the growth cone, the major player in this process. The mammalian growth cone has a diameter of about 5-20 μm and consists of three regions: the central (C) region rich in stable, bundled microtubules, the peripheral (P) domain containing long, bundled actin filaments which form the filopodia and mesh-like F-actin networks forming the lamellipodia, and the transition (T) zone between the previous two regions [30] (Fig 2.1). This cytoskeletal network is highly dynamic. Filopodia continuously extend and retract and lamellipodia dynamically change shape. Microtubule tips projecting from the C-domain to the P-domain constantly add and subtract subunits at the tip. The actin network undergoes retrograde flow and depolymerises behind the leading edge, releasing actin subunits to the front for polymerisation [30].

Actin plays a key role in growth cone migration. The continuous treadmilling of F-actin provides the motor to drive movement. F-actin retrograde flow is driven by the motor protein myosin II and the push from F-actin polymerisation in the P-domain. Compression by myosin II in the T-zone buckles the F-actin bundles. These actin fragments are recycled to the periphery

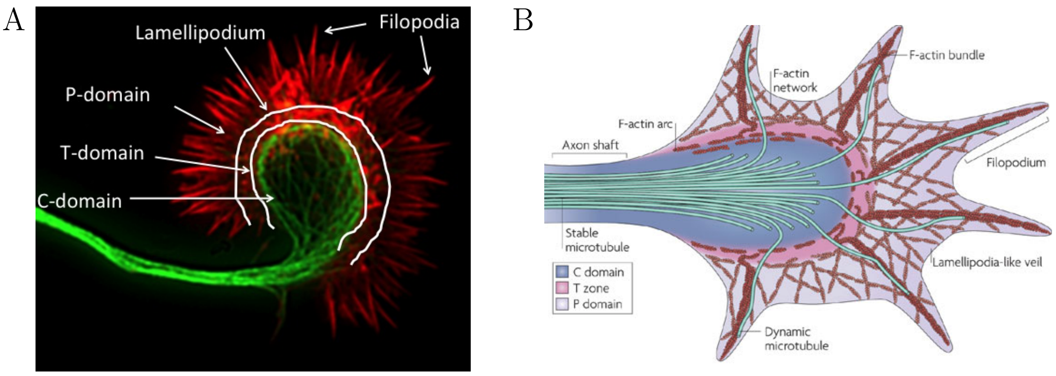

FIGURE 2.1: **The growth cone**. A. Fluorescence image of a growth cone adapted from [31]. Actin filaments (red) are stained with phalloidin and form the lamellipodium and filopodia. Microtubules (green) are stained with anti-tubulin antibodies and form the axon and central region of the growth cone. Between the periphery (P-domain) and centre (C-domain) is the transitional (T) zone. B. The structure of the growth cone, adapted from [30]. The P domain contains long, bundled actin filaments which form the filopodia and a mesh of F-actin that forms the lamellipodia. In the C-domain, stable bundled microtubules form the axon shaft and splay out in the growth cone.

for actin polymerisation at the leading edge [32]. The 'clutch' hypothesis or the 'substrate-cytoskeletal coupling' model proposes the mechanism for actin dynamics to drive growth cone advance [33]. The growth cone plasma membrane contains receptors that bind to adhesion molecules on other cells or the extracellular matrix (ECM). Receptor clustering can lead to persistent bonds and form large adhesive contacts with intracellular complexes. These adhesion points stimulate actin filament polymerisation to protrude from the leading margin, stabilise the newly extended protrusions and tether actin filaments to the substrate. This slows down the retrograde flow that normally pulls actin rearward toward depolymerisation, providing the tension to pull the growth cone forward. Adhesion at the back of the growth cone weakens and the growth cone turns into the cylindrical shape of the axon [33].

The coupling to the substrate generates a tension which is critical for growth [33]. Tension in the growth cone appears to be dependent on two main properties of the substrate: stiffness and ECM components. Firstly, *in vitro* studies have shown that traction force increases on stiffer substrates [34]. CNS and PNS neurons have different sensitivities on substrate stiffness due to adaptation to their natural environments [34]. Secondly, detailed force measurements have found that axons on less adhesive surfaces exert more tension [35]. Thus the substrate can have profound impact on how growth cones respond to guidance cues. Biophysical models have illuminated the possible impacts of tension force, axonal viscosity and adhesion to axon outgrowth [36–38]. Our mathematical model will later reveal the importance of tension and make useful predictions about how different ECM environments might affect turning due to gradients.

2.1.3 The diversity of guidance cues

The journey by which an axon extends from its cell body and travels through the embryo to its target involves a vast number of molecules and pathways working together to ensure the proper connections can be made [1–3, 39]. In recent decades, great progress has been made in identifying the molecules and pathways involved in axon guidance. Although this is not a focus of the thesis, for completion we briefly summarise the key players in the molecular processes.

In the late 1980s and early 1990s, advances in genetic and biochemical screens led to the discovery of a plethora of guidance cues and their receptors. The canonical guidance cues include Netrins/Unc-6, Slits, Semaphorins, and Ephrins [2]. Guidance molecules also include morphogens, secreted transcription factors, neurotrophic factors and neurotransmitters [30]. The diverse functions of guidance cues, their ability to combine and interact at the membrane and intracellular levels, combined with alternative mRNA splicing and post-translational modifications of receptors and ligands, results in a vast repertoire of different signals [2].

As the growth cone traverses the developing brain, it likely detects multiple cues along its path. The cues can be diffusible or substrate-bound [2] (Fig 2.2). For example, gradients of diffusible netrins are crucial in the control of spinal cord development *in vivo* [29], while gradients of membrane-bound ephrins are involved in the control of topographic mapping *in vivo* [40]. Guidance cues can be permissive/attractive to direct axons to the right target or inhibitory/repulsive to prevent axons from approaching incorrect targets. While permissive extracellular matrix proteins such as laminin or cell adhesion molecules such as the immunoglobulin superfamily (IgS) can act as adhesive molecules and chemoattractants [41], nonpermissive surface bound molecules such as Slits and Ephrins can inhibit growth cone migration [30]. However, the response of attraction or repulsion is not simply an intrinsic property of the cue, but the specific receptors and the signalling pathways activated [2].

In chapters 5 and 6, we studied the responses of peripheral axons to gradients of nerve growth factor (NGF) to characterise the trajectories, thus NGF is briefly introduced here. First studied in detail in the 1940s by Rita Levi-Montalcini and Viktor Hamburger, neurotrophic factors

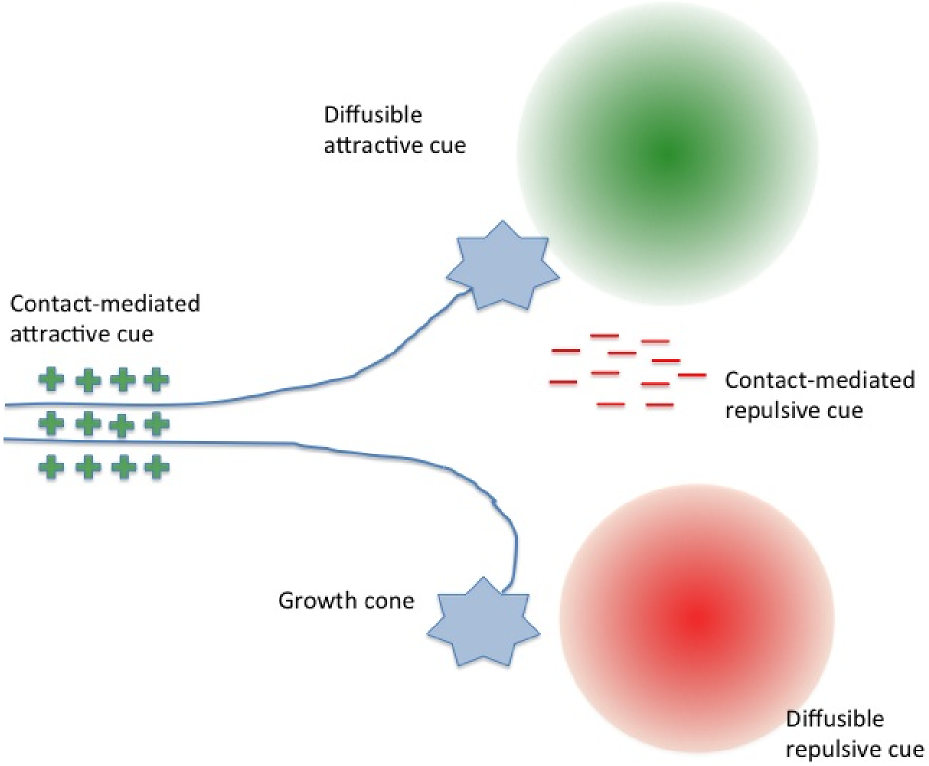

FIGURE 2.2: **Axon guidance**. The growth cone can grow on permissive substrates containing a contact-mediated attractive cue or is inhibited by a repulsive/inhibitory cue. The growth cone can be attracted by diffusible gradients of attractants (green) or repulsed by gradients of repellents (red).

are target-derived and essential for neuronal survival and maintenance [42–44]. In mammals, neurotrophins such as nerve growth factor (NGF), brain-derived neurotrophic factor (BDNF) and neurotrophin-3/4 (NT-3) can also have guidance properties [45]. They bind to the Trk family of tyrosine kinase receptors, TrkA, TrkB and TrkC respectively. The neurotropic property was not discovered until 1978, in *in vitro* experiments where chick dorsal root ganglion neurons turned towards NGF from a pipette tip [46]. Since that study, NGF has been widely used to investigate further details of growth cone chemotaxis.

2.1.4 Downstream signalling pathways of guidance cues

Guidance receptors are linked to molecular switches such as Rho-family GTPases. These include RhoA, Rac1 and Cdc42, which provide the link between upstream directional cues and downstream cytoskeletal network [47]. They activate pathways that control the organisation and distribution of actin filaments. It is believed that they can either increase actin polymerisation for protrusion or enhance depolymerisation and actomyosin contraction for retraction [48].

Repulsive cues such as Semaphorin3A induces translation of GTPase RhoA, which promotes actin depolymerisation, reducing protrusion and adhesion. Attractive cues switch off RhoA and switch on Rac1 and Cdc42, which promotes actin filament polymerisation and formation of adhesion points [48]. The complex crosstalk of these molecules has been a rich source of mathematical models that can help constrain which of the many proposed interaction schemes are consistent with observed dynamics of the proteins [49–51].

Classical second-messenger molecules such as Ca^{2+} and the cyclic nucleotides are also known to play key roles in governing guidance response. Their interactions are complex and are reviewed in [52]. Here we only emphasise the key pathways. Many studies have shown that transient or sustained global increase in intracellular calcium concentration, i.e. depolarisation, can slow or halt axon outgrowth [53–57] while a lowered concentration has the opposite effect [57, 58]. Localised calcium signals can promote growth cone turning by enhancing protrusion and stabilisation of filopodia [59–62]. However, a consistent directional guidance effect can only happen when there is a stable asymmetry in the calcium concentration pattern across the growth cone [60, 62, 63]. The exact identity of calcium channels that give rise to spontaneous calcium transients in growth cones and filopodia are still elusive [62]. As they are unaffected by voltage-dependent calcium channel (VDCC) blocking, they are probably not VDCC [64, 65].

Binding of guidance cue to the receptors activates the transient receptor potential family of non-selective cationic channels, causing an initial influx of calcium that depolarises the neuron sufficiently to trigger VDCCs [66, 67]. This leads to the influx of calcium via VDCC and the release of calcium from from the endoplasmic reticulum into the cytoplasm [68]. In an extracellular gradient of guidance cue, the asymmetric binding of ligand molecules and receptors results in an intracellular calcium gradient. Under normal conditions, a steep intracellular calcium gradient is likely to lead to attraction, while a shallow intracellular calcium is likely to result in repulsion [60, 62, 69].

There are two main mechanisms for triggering release of calcium from intracellular stores: inositol trisphosphate (IP3)-induced Ca^{2+} release (IICR) [70] and Ca^{2+}-induced Ca^{2+} release (CICR) [71]. It has been proposed that the method of calcium entry is the determinant of turning: calcium entry involving both CICR and IICR leads to an attractive response, while Ca^{2+} signals without store entry results in a repulsive response [72, 73].

Upon entry into the cell, calcium binds to calmodulin to form a calcium/calmodulin complex [74]. Two downstream effects are calcium/calmodulin dependent protein kinase II (CaMKII) and calcineurin (CaN). Having a higher affinity for calcium/calmodulin, CaN responds more strongly than CaMKII at low calcium concentration while CaMKII dominates at high calcium levels [75]. The ratio CaMKII:CaN is the determinant of whether the guidance response is attraction or repulsion [75].

Ca^{2+}-dependent responses can be further modulated by the cAMP pathway. cAMP activates and cGMP inactivates voltage-dependent Ca^{2+} channels [76, 77]. cAMP also enhances calcium-induced-calcium-release from intracellular calcium stores, while cGMP inhibits it [72]. An extracellular gradient of cAMP can promote attraction [78] whereas lowering the cAMP/cGMP ratio can switch attraction to repulsion [79–81]. A mathematical model was developed which can explain how the sign of the response is determined by the asymmetry in the CaMKII:CaN ratio between the two sides of the growth cone [61, 82]. This unifying mathematical model explains many apparently perplexing existing results and can predict guidance decisions across a wide range of conditions, providing important insights into the mechanisms of axon guidance.

Downstream effectors shift the imbalance in endocytosis and exocytosis and lead to an attractive or repulsive response [73]. Repulsive guidance cues induce asymmetric endocytosis on the up-gradient side of the growth cone whereas attractive cues induce asymmetric exocytosis [69, 83]. Asymmetric Ca^{2+} levels result in asymmetric activation of the Rho GTPases (attractive cues activate Rac and Cdc42, repulsive cues activate RhoA), leading to remodelling of the cytoskeleton and turning [84].

The binding of receptors to ligand molecules not only activates existing downstream molecular pathways but also local mRNA translation [85, 86]. This was discovered by severing the growth cone from the cell body and observing that it continued to exhibit chemotropic responses, indicating that the growth cone contains a semi-autonomous apparatus. The functional role of local mRNA translation was first demonstrated in *Xenopus* retinal ganglion cell axons separated from the soma. In these axons, translation inhibitors could block the attractive turning response in a gradient of netrin-1 [87] and the chemotropic "collapse" response of growth cones to Sema3A and Slit2 [87, 88]. Together, the above studies reveal remarkably diverse mechanisms employed by the growth cone to navigate the complex landscape of the embryonic brain.

2.2 A Bayesian framework for gradient sensing

One of the aims of this thesis is to gain a better understanding of gradient sensing by analysing how a growth cone might make the best use of the information from its receptors to estimate the state of the environment. The Bayesian inference framework has been very influential in addressing this general task of extraction of a signal from noise [89, 90], which is the first step in any chemotactic system. We now explain the fundamentals of Bayesian inference, the framework that underpins the analysis in the next two chapters.

Bayesian inference provides the framework for manipulating beliefs, i.e. how to update beliefs as new information arrives, in a consistent manner using Bayes theorem. At its core, Bayes theorem expresses the relationship between joint and conditional probabilities. For two random variables X and Y, the probability that X takes the value x, Y takes the value y is denoted $P(X = x, Y = y)$ and

$$\begin{aligned} P(X = x, Y = y) &= P(X = x|Y = y)P(Y = y) \\ &= P(Y = y|X = x)P(X = x) \end{aligned}$$

where the first term on the right hand side is known as the conditional probability that $X = x$, given that $Y = y$. Rearranging the equation above, we have

$$P(X = x|Y = y) = \frac{P(Y = y|X = x)P(X = x)}{P(Y = y)}$$

When applied to sensory processing

$$P(W|D) = \frac{P(D|W)P(W)}{P(D)}$$

where W is the state of the world and D is the data about the state of the world. $P(W)$ is the prior distribution of the state of the world, reflecting the observer's beliefs before a measurement. $P(D|W)$ is the likelihood function, in which the data and world state are related in a full probability model. $P(W|D)$ is the posterior distribution, or the updated belief about the world after the measurement.

Given the observation D, it is often necessary to report or act on an estimate of W that optimally describes the data in some sense. Bayesian decision theory formalises this process of choosing the best estimate. First, we define the loss function $l_D(W^*, \hat{W})$, which quantifies the cost associating with reporting $W = \hat{W}$ when the data were actually generated by $W = W^*$. Then the average or expected loss for reporting $\hat{W}$ is:

$$\mathcal{L}_D(\hat{W}) = \langle l_D(W^*, \hat{W}) \rangle_{p(W=W^*|D)} = \int l_D(\hat{W}, W^*) p(W = W^*|D) dW^*$$

The expected loss is integrated over all possible values of W^*, weighted by their probabilities given the data, and measures how much loss can be expected when $\hat{W}$ is chosen as the estimate. The optimal decision procedure has to choose a $\hat{W}$ that minimises this expected loss.

The binary loss function has the form:

$$l_D(\hat{W}, W^*) = 1 - \delta_{\hat{W},W^*} = \begin{cases} 1 & W^* \ = \hat{W} \\ 0 & \text{otherwise} \end{cases}$$

Using this loss function, the expected loss is:

$$\mathcal{L}_D(\hat{W}) = \int l_D(\hat{W}, W^*) p(W = W^*|D) dW^* = 1 - P(W = \hat{W}|D)$$

This quantity is minimised when $\hat{W}$ is chosen to be the maximum of the posterior distribution $P(W|D)$ or the *maximum a posteriori* (MAP) estimate:

$$\hat{W} = \underset{W}{\text{argmax}} P(W|D)$$

In the case that the prior is flat (uniform), then the MAP estimate reduces to the maximum likelihood estimate:

$$\hat{W} = \underset{W}{\text{argmax}} P(D|W)$$

The Bayesian framework has made important contributions to theoretical neuroscience and has been successful in building computational models for perception and sensorimotor control [91]. Bayesian modelling is aimed at predicting and systematising performance data, comparing performance to a benchmark, instead of explaining mechanisms [92, 93]. A theoretical observer is called an ideal observer if it can make optimal interpretations about the stimuli which give rise to sensory inputs, meaning that it achieves the best performance averaged over all stimuli [94].

The growth cone (or any other chemotactic cell) faces a statistical inference problem, and Bayesian Decision Theory is a useful approach to understand the best possible performance. A Bayesian model for axon guidance has been developed and has been successful in explaining the chemotactic efficiency of axons in shallow gradients as a function of concentration and gradient steepness [95]. This model analyses how a growth cone might make the best use of information from receptors to estimate the gradient. The growth cone is considered an ideal observer performing statistical inference by combining prior assumptions about the gradient with likelihood information coming from its binding patterns (Fig 2.3). Given a particular binding pattern, the growth cone infers the distribution over the gradient that gives rise to that binding pattern.

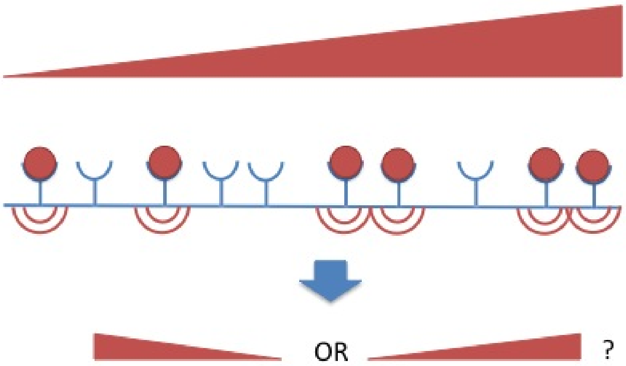

FIGURE 2.3: **Bayesian model of spatial gradient detection.** The model growth cone in [95]. The probability that receptors bind ligand molecules is determined by standard Michaelis–Menten kinetics and depends on the local concentration at the receptor. The growth cone then combines signals from individual receptors to optimally decide the gradient direction for that binding pattern.

In [95], the prior probability of the steepness is assumed to be symmetric and concentrated around 0. The likelihood function of each binding pattern for different concentrations and gradient steepnesses is the product of the binding probabilities of individual receptors. For a receptor at position $\vec{r}_i$, its binding probability using standard Michaelis–Menten kinetics is:

$$P(\text{receptor } i \text{ is bound}) = \frac{C(\vec{r}_i)}{C(\vec{r}_i) + K_D} \tag{2.1}$$

where $C(\vec{r}_i)$ is the ligand concentration at the i^{th} receptor's position and K_D is the dissociation constant, i.e. the concentration at which the binding probability is exactly half. Combining this likelihood function and the prior, they derived the posterior distribution of the gradient given a binding pattern. From the posterior probability, the *maximum a posteriori* estimate of the gradient can be obtained. The performance of the estimation (which translates to the guidance ratio) as a function of steepness $\mu = \nabla C/C$ and normalised concentration $\gamma = C/K_D$ can then be derived:

$$\text{Performance} \propto SNR = \mu\sqrt{\frac{\gamma}{(1+\gamma)^3}} \tag{2.2}$$

By using an assay that can generate gradients precisely, this prediction was confirmed quantitatively but up to an arbitrary constant by analysing growth cones' responses when both concentration and steepness were varied experimentally (Fig 2.4).

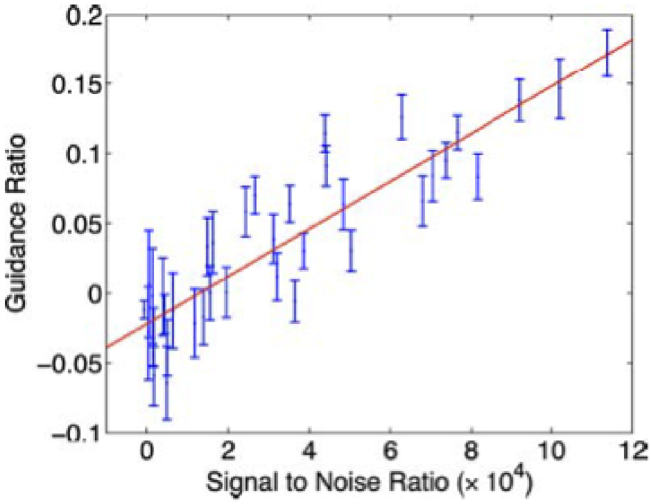

FIGURE 2.4: **A Bayesian model of growth cone chemotaxis**. The experimentally measured chemotactic efficiency (guidance ratio) of rat dorsal root ganglion neurites is predicted by a Bayesian model of axon guidance. The guidance response increases linearly with the signal-to-noise ratio in equation 2.2, which depends on the background concentration and gradient steepness. (Image from [95])

Similar works using a flat prior investigated the role of receptor cooperativity in spatial gradient sensing [96], the information loss during the various stages of directional sensing [97], the effect of geometry and internal bias on gradient sensing [98] and the bias in sensing of weak gradients by elliptical cells [99].

The presence of the prior distribution allows examining different assumptions about the initial bias of the cell, for example: unpolarised cells newly introduced to a gradient or polarised cells that have been exposed to the gradient for a long time or have a spontaneous intracellular bias toward a particular direction. It is known that the growth cone's behaviour is dependent on the history of previous stimulation [100]. Similarly, the response of *Dictyostelium* cells to extracellular signals is strongly dependent on the initial intracellular bias [20]. Many observations are consistent with the possibility that polarised cell morphology or asymmetries in the distribution of signalling components are ways that prior information might be represented [6, 101–104]. We will later analyse the interactions between the likelihood function and the prior bias for a general sensing device in chapter 4.

In all these models, it is assumed that receptors are stationary on the cell surface. However, recent advances in single-molecule tracking techniques have allowed observing movement of single molecules in the plasma membrane, showing that the membrane is a compartmentalised fluid [105]. Receptors are generally in constant motion in the membrane and undergo diverse modes of diffusion. This movement smears out the positional information in each receptor. In chapter 3, we will extend this framework to understand how receptor diffusion can affect the quality of gradient sensing.

2.3 Models of growth cone movement

Analysing growth cone trajectories in gradients is crucial to our understanding of axon guidance. It is critical to investigate the key factors impacting growth cone trajectories to determine the principles and limits of guidance due to gradients. This quantitative understanding will help predict axon trajectories *in vivo* under normal and abnormal conditions, contributing to the ability to optimise gradients for promoting nerve regeneration after injury. There is a wealth of related mathematical models of cell motility in general and growth cone motility in particular. In chapter 6, we will construct a model of growth cone trajectories in attractive and repulsive gradients that has been matched to experimental data. Here a review of motility models in other systems will be presented before focusing on growth cones.

2.3.1 Random walk models of cell motility

A widely-used phenomenological framework in describing cell motility is random walk theory. The beginning of random walk theory came from the observation that pollen particles undergo Brownian motion or simple random walks, formally described by Einstein in 1905 [106]. Simple random walks are uncorrelated and unbiased, where each step is independent of previous ones and uniformly distributed in random directions. Przibram in 1913 demonstrated that this model described the random motion of protozoa [107].

Furth studied the motility of protozoa in more detail and found that his data were not well modelled by a simple random walk [108]. He considered a random walker on a lattice, and gave directional persistence in the form of a bias towards stepping in the similar direction as the previous step. Correlated random walks imply that consecutive steps are correlated, which is termed persistence [109]. It is globally unbiased in the sense that there is no overall preferred direction. Since most animals and cells have a tendency to move forward, correlated random walks have been widely applied to model random movements in fibroblasts, amoeba and migrating animals [110–114]. In many models, the steps are correlated via a non-uniform distribution of turning angles between successive steps.

Paths that exhibit a consistent bias in the preferred direction are termed biased random walks. The bias may be due to anisotropy in the environment such as gravity [115] or chemical gradients [116, 117]. A global directional bias can be introduced by making the probability of moving in a certain direction greater or making paths in the biased direction longer. While bacteria move in random directions and have longer run lengths in the direction of the gradient[118, 119], leukocytes change their direction asymmetrically in preference for directions up the gradient while the run lengths are independent [115, 120].

Another popular type of random walk to describe motility is a Levy walk, which consists of random walks where short jumps are separated by infrequent long steps. The step length distribution is given by $P(s) \approx s^{-\mu}, 1 < \mu < 3$. The mean square displacement (MSD) in Levy motion is super-diffusive, meaning that as a function of time t, $MSD(t) \propto t^{\alpha} (\alpha > 1)$ while a correlated random walk eventually reaches normal diffusion over long times. Levy walks in marine animals have an exponentially decreasing distribution of step-lengths which may represent an optimisation of foraging in a heterogeneous prey field [113].

2.3.2 Random walk models of growth cone trajectories

Several random walk models have been formulated to describe the trajectories of growth cones. The presence of the axon that tethers the growth cone to the cell body or the branch point causes the growth cone to move in a relatively straight path. Growth cone movements were first quantitatively analysed in [121]. The movement was separated into elongation and nonelongation elements and these were found to be almost completely independent of each other. Katz [122] found that growth cones moved in relatively straight paths even though the instantaneous movements could be highly erratic. The trajectories were well-approximated by an uncorrelated random walk with drift which represented the tendency to elongate.

Due to the tendency of axons to grow fairly straight, correlated random walks with persistence in motion direction have been the popular choice. A common way to achieve correlation between successive steps is through a non-uniform turning angle distribution. Pearson *et al.* [123] used a correlated random walk model to describe the trajectories of rat pyramidal neurons. The instantaneous turning angle θ is a function of the arc length s from the axon's initiation point. Without a gradient, the position of the growth cone is parameterised by s:

$$\begin{aligned} dx(s) &= \cos\theta(s)ds \\ dy(s) &= \sin\theta(s)ds \\ d\theta(s) &= D_\theta dW_\theta(s) \end{aligned}$$

where $D_\theta dW_\theta(s)$ is a Weiner process. The turning angles of embryonic rat hippocampal neurons had small variance, leading to fairly straight paths. However, they did not have data with the gradient to further develop this model. Maskery *et al.* [124] analysed growth cone pathfinding patterns and found that they exhibit both deterministic (smooth forward motion) and stochastic (frequent pauses and sudden directional changes) components. They simulated growth cone contact with a repulsive cue and measured the resultant turn angle (Fig 2.5). Migration is described by two equations representing migration in the direction of axonal outgrowth (Δy_{ct}) and in the orthogonal direction (Δx_{ct})

$$\Delta x_{ct} = e_{xt}$$

$$\Delta y_{ct} = e_{yt} + \Delta y_{avg}$$

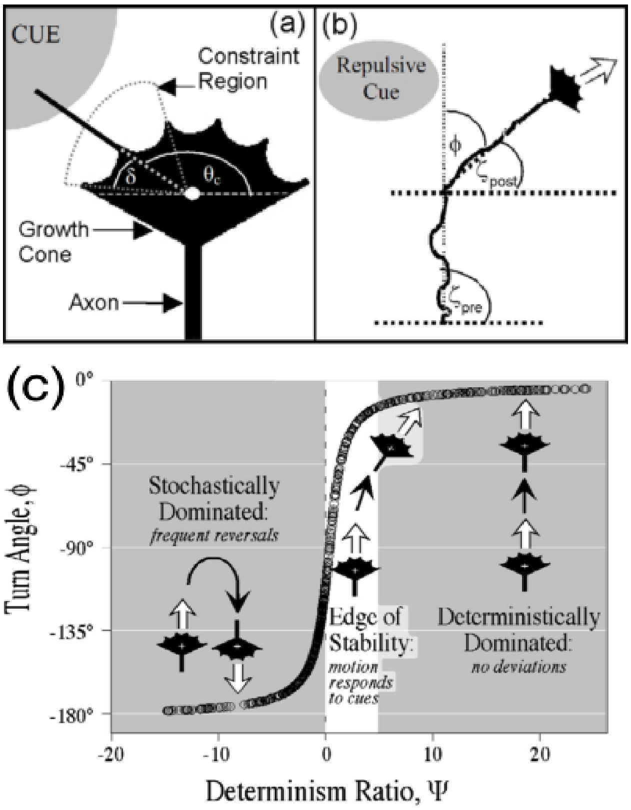

FIGURE 2.5: **A model of contact-mediated repulsion in [124].** The schematic of growth cone movement adapted from [124]. An angular region of size 2δ centred around the filopodium that contacts the repulsive cue defines the constraint region that the growth cone cannot migrate into. The turning angle is ϕ. The determinism ratio Ψ is defined as $\tan^{-1}(\pi/2 - \phi)$. In the stochastically dominated region $\phi < -90°$ and the growth cone collapses. In the edge of stability region, deterministic and stochastic motions are balanced and guidance is achieved. In the deterministically dominated regime, the growth cone largely migrates forward without much guidance influence.

e_{xt} and e_{yt} are drawn from independent and normal random distributions with zero means and constant standard deviations, and Δy_{avg} is the average speed in the y direction. Filopodia extend and retract randomly at some constant rates. When a filopodium contacts the target, repulsion is elicited. To model the effect of a contact-dependent repulsive cue at angle θ_c, they blocked migration within a small region around the direction of contact $\theta_c \pm \delta$. The determinism ratio Φ is defined as

$$\Phi = \tan^{-1}(\pi/2 - \phi)$$

where ϕ is the final turning angle. If $\Phi \ll 0$, the growth cone is stochastically dominated, or it frequently reverses irrespective of the cue. If $\Phi \gg 0$, the growth cone is deterministically dominated or it travels forward with little influence by the gradient. They found that only if stochastic and deterministic elements are comparable (i.e. $\Phi \approx 0$) can the growth cone be guided properly. Although it is an interesting conceptual model, it has not been directly compared to experimental data.

Odde *et al.* [125] analysed the motion of neonatal rat growth cones and found that the experimentally sampled trajectories could be well described by:

$$\begin{aligned} x_t &= \phi_x x_{t-1} + a_{x,t} + \theta a_{x,t-1} \\ y_t &= \phi_y y_{t-1} + a_{y,t} + \theta a_{y,t-1} \end{aligned}$$

where ϕ_x, ϕ_y are constants and $a_{x,t}, a_{y,t}$ are Gaussian distributed random noise terms. However, they had a very limited data set of 6 growth cones and did not have gradient conditions.

In another model that simulates axon growth in the tadpole spinal cord [126], the axon growth angle depends on the tendency to turn towards the gradient angle and noise. The position of the growth cone at timestep n is (x_n, y_n) and the heading direction of the n^{th} step is θ_n. With a gradient pointing in the x direction, the growth cone's position is governed by three equations:

$$\begin{aligned} x_{n+1} &= x_n + \Delta\cos(\theta_n) \\ y_{n+1} &= y_n + \Delta\sin(\theta_n) \\ \theta_{n+1} &= (1-\gamma)\theta_n + \mu(\bar{y} - y_n) + \xi n \end{aligned}$$

where ξ is a random variable uniformly distributed in the interval $[-\alpha, \alpha]$, Δ is a fixed step size, γ represents the tendency to align with the gradient. The parameter $\bar{y}$ represents the position of an attractor with strength μ. The parameters were found to match the empirical spatial distribution of axons and tortuosities. The noise term is small ($\alpha = 2-5°$), leading to straight, realistic looking paths. This model was based on data from anatomical images of axons in the spinal cord while the growth process was not recorded. Thus important information about actual growth cone movements was lacking.

2.3.3 Models based on ligand-receptor binding or filopodial activity

Other models include possible mechanisms of how trajectories are achieved. In an early model of the retino-tectal projection [127], inspired by Sperry's hypothesis, Gierer proposed that retinal as well as tectal tissues contain gradients in two directions and retinal axons originating at coordinates u, v interact with tectal tissue at position x, y to generate a potential $p(x, y, u, v)$. The trajectory of each axon will follow gradient descent of this function to reach the position of minimal potential. Due to the lack of precise measurements of gradients *in vivo* and the unknown form of the function p, this hypothesis has not been confirmed.

Buettner and colleagues' models in the 1990s aimed to describe dynamics of *in vitro* growth cones from measurements of growth cone movements on different substrates [128–130] . The growth cone is modelled as a circular disk with filopodial sticks. Filopodia extend and retract with a constant rate, switching between these two phases according to a gamma distribution. Buettner *et al.* studied how filopodial initiation, growth and collapse influence the probability of contacting a target cell [128]. The motion of the growth cone is modelled as a two-step process in which it wanders randomly until it contacts an attractive cue that triggers filopodial dilation. The growth cone then retracts its other filopodia and flows along the filopodium that contacts the cue. On uniform regions of the substrate, the growth cone moves with a velocity that decreases exponentially with time but fluctuates and occasionally resets. Filopodial dilation is governed by an extension and retraction rate and is initiated when sufficient filopodia have contacted the cue. This model qualitatively described growth cone behaviours *in vitro*; however, more quantitative measurements of movement statistics were not made.

Li *et al.* simulated trajectories by assuming the turning angle of the growth cone is in proportion to the angle between the neurite and the resultant filopodial tension [131]. Filopodia are randomly initiated and exert tension on the main body of a growth cone. When the forces pulling the growth cone apart exceeds a certain threshold, the growth cone bifurcates. The model could generate qualitatively realistic-looking neuronal morphology although a more quantitative comparison with data was lacking.

To simulate growth cone movements in gradients, another set of models has concentrated on how asymmetric receptor binding across the growth cone might be used as a turning signal. Aeschlimann [132] proposed a model in which filopodia act as both sensors and motors, pulling the growth cone in different directions. The axon stretches or, above some force threshold, lengthens through inelastic extension. Filopodia contact guidance cue molecules, leading to an elevation in intracellular calcium. The probability of initiating a filopodium at any location is determined by the calcium concentration. The asymmetric binding on the growth cone surface results in an asymmetric calcium and filopodia distribution, leading to movements biased in the gradient direction.

In a similar model [133], Goodhill *et al.* considered an idealised growth cone consisting of a two-dimensional semi-circular body from which one-dimensional filopodia extend and retract. Both the surface of the growth cone body and the filopodia are covered with receptors at random locations. The growth cone is divided into bins of equal size. The probability of generating a new filopodium is a function of receptor binding in each bin. As a new filopodium is generated, the oldest filopodium is retracted, maintaining a constant number of filopodia. The growth cone then moves a constant small distance, mostly in the forward direction but with a slight deviation to the side with more filopodia. This model aimed to explain the rapid turning in steep gradients and more gradual turning in shallow gradients. In both this model and the previous one, the statistics of growth cone movements in this model was not compared with experimental data.

The work of Xu *et al.* [134] is an extension of the model in [133]. At each timestep, the growth cone's movement is a combination of the current heading and a gradient signal from receptors. The gradient signal requires spatial and temporal averaging of the stochastic receptor-binding signal. Once a receptor-binding density as a function of angle around the growth cone has been calculated, the growth cone picks the direction in which this is maximum and calculates a weighted average with the current direction. This model explains well the different chemotactic efficiency of explants of thousands of cells at different guidance molecular concentrations. However, the aim was to simulate the behaviour of populations of thousands of neurites, instead of individual ones.

In a recent model [135], it was assumed that sensors on the filopodia of the growth cone can detect the gradient direction. The growth cone then sums all the gradient estimation vectors from its sensors and changes its position by that vector. However, it is not clear in this model how the sensors (supposedly receptors) can detect the gradient itself. The model is slightly unrealistic in that it is an entirely deterministic model of growth cone trajectories.

2.3.4 Models based on the concentration field's effect on velocity

A third group of models considers the possibility that the velocity of the growth cone is influenced by gradients. van Ooyen and colleagues developed a model whereby the velocity of the growth cone is influenced by the attractive gradient from the target cells and the chemoattractant and chemorepellant released from other growth cones and itself [136, 137]. In [136, 138], state vectors that represent the position or velocity of objects that interact with the concentration fields of chemotactic molecules are coupled to diffusion equations that describe the concentration fields of diffusible chemoattractants and chemorepellents.

Mortimer *et al.* [139] examined the possibility that growth rate is a function of gradient. Instead of sensing the gradient from the receptor binding across the growth cone, in shallow gradients, axons sense the gradient along the axon shaft and grow faster up than down the gradient. This model captures the chemotactic performance of explants growing in a gradient over a long time.

However none of these models has been closely compared with the details of experimentally measured trajectories in gradients. In particular, parameters such as variability in step sizes, the distribution of instantaneous turning angles, and straightness of real paths, have not been addressed. Thus the question of whether there is a model that can adequately capture all these characteristics of real trajectories remains open. Without such a model, it is difficult to determine if trajectories observed *in vivo* are in fact consistent with gradient guidance.

2.4 Assays for studying axon guidance

In order to build and test a quantitative model of growth cone trajectories in gradients, we needed a culture assay that can allow us to gather a large amount of data from many growth cones in a reproducible condition. Here we therefore review previous chemotaxis assays.

Understanding axon guidance requires a combination of *in vivo* studies in different animals models and *in vitro* studies with more controlled environments to exclude confounding factors. It is desirable to produce gradients in *in vitro* cell cultures that can mimic the gradient of proteins that axons encounter *in vivo*. Although the shape and nature of *in vivo* gradients are difficult to measure accurately, *in vitro* cultures are useful to create a controlled environment to study the mechanisms and responses to guidance cues. A number of assays have been developed towards this aim (reviewed in [140], [141]). Axon guidance assays can be divided into two main categories: diffusible and substrate-bound gradients. Here we only focus on the assays most commonly used and relevant to axon guidance.

2.4.1 Diffusion-based chemotaxis assays

Diffusion-based assays were first developed in the 1960s to study chemotaxis in a wide range of cell types (Fig 2.6). The early assays, including the Boyden, Zigmond and Dunn chambers, use two compartments separated by a porous membrane or by small channels [142–144]. The source chamber contains a higher concentration of chemotactic cue which diffuses into the sink chamber. The gradient due to the passive diffusion will have a directional effect on the cells growing nearby. The Boyden chamber, developed in 1962, consists of two compartments containing chemoattractant solutions of different concentrations separated by a filter membrane [142]. A gradient will form across the membrane by diffusion. Cells or axons respond to the gradient and actively migrate through the pores in the membrane. Widely used in the study of chemotaxis of leukocytes and fibroblasts, the Boyden chamber assay is useful in screening large numbers of cells and potential chemotactic factors [145–148]. By plating the cells in the upper chambers, this assay was used to separate cell bodies and axons to study the lysate of axons only. The axons were attracted towards nerve growth factor in the lower chamber while the somas were too large to go through the pores [149, 150]. However, the process of migration cannot be viewed in real-time and the gradient cannot be quantified precisely.

The Zigmond chamber consists of two wells of a chemotactic factor separated by a narrow space, sealed by a coverslip on which cells are growing. Diffusion between the two wells creates a gradient [143]. However, the gradient decays over time and disappears in roughly 90 minutes, limiting its use to only fast-responding cells [151–153]. The Dunn chamber works in a similar fashion and is made of two concentric circular wells containing two different concentrations of a chemotactic cue on a slide [144]. The two wells, one of which contains cells, are separated by a circular bridge and sealed by a coverslip where the cells can move from one well to the other. All three assays suffer from the same disadvantage that the gradient is unstable and decays over time.

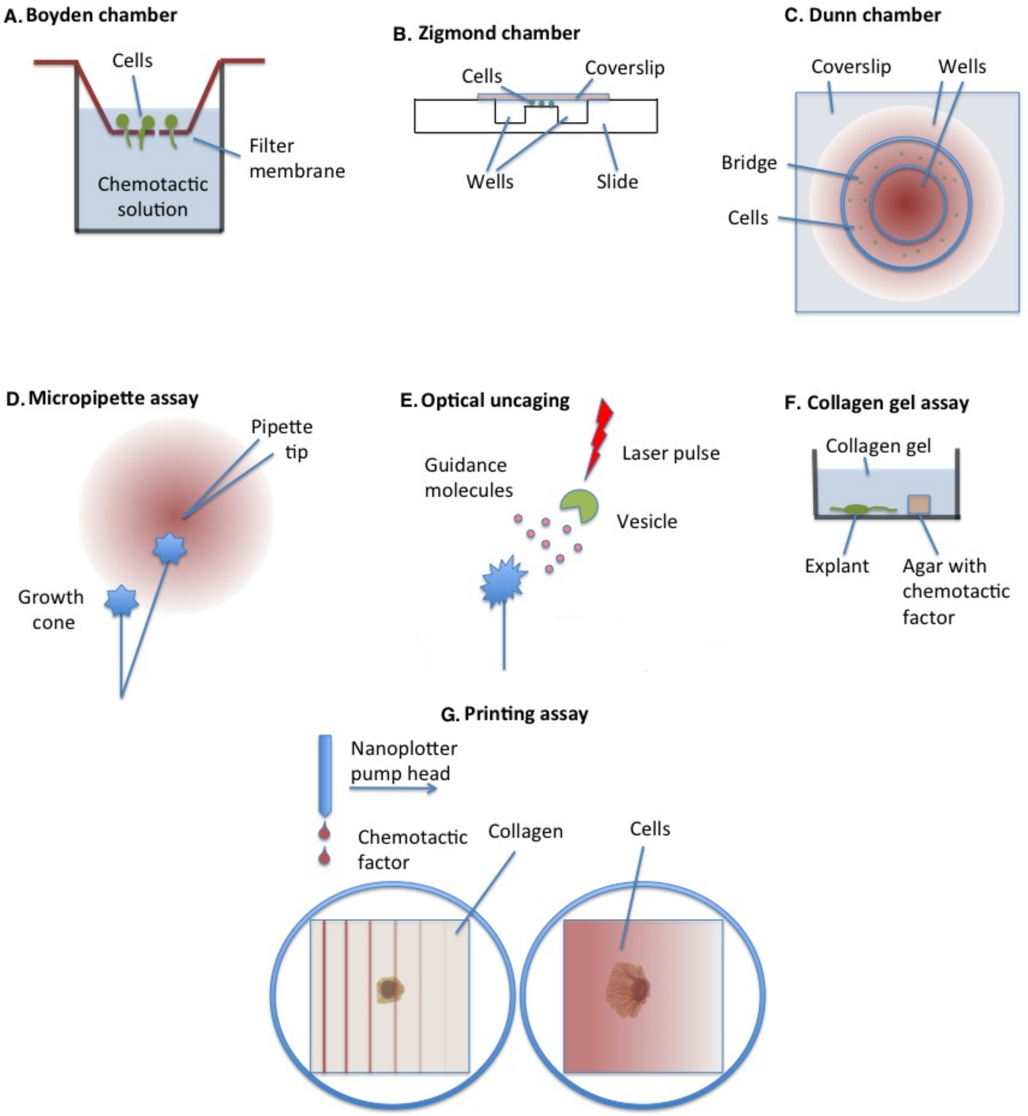

FIGURE 2.6: **Diffusion-based chemotaxis assays**. A-C. In the Boyden, Dunn and Zigmond chambers, the chemotactic factor diffuses from the source chamber to the sink chamber generating a gradient on which cells move. D. In the pipette assay, the chemotactic agent is released from a micropipette near the growth cone. E. The optical uncaging technique uses a laser pulse to release the guidance molecules from a lipid vesicle. F. In the collagen assay, an explant of cells is place in a collagen gel near a block of agar containing the chemotactic factor. G. The printing assay uses a pump to print out lines of different concentrations of a chemotactic factor on collagen gel. The cue then diffuse throughout the gel creating a stable gradient that can last for days.

Unlike previous assays, the micropipette assay relies on diffusion or ejection of the chemotactic factor from a small pipette tip. The precursor of the micropipette assay was developed as early as the 1880s, when Pfeffer observed bacterial chemotaxis by inserting a capillary containing a chemotactic cue into a bacterial solution and finding accumulation of bacteria at the tip of the capillary [154]. Methods in the 1970s relied on gravity to transfer the chemical from the pipette

[155]. The first study using the pipette assay showed the chemotactic effect of NGF on chick dorsal root axons [155]. To deliver small volumes with more control, the improved technique used compressed gas with a timer-driven gate to eject the guidance cue in a pulsatile fashion [78, 80]. This method allows manipulation by bath application of extra factors and has been very widely used in studying axon guidance [61, 79, 156, 157].

Optical uncaging of caged molecules (a light-sensitive version of the molecule) or encapsulated molecules in lipid vesicles is an alternative method to create local sources of guidance molecules with precise temporal and spatial resolution near or inside the growth cone [158–160]. This method has led to important understanding of the role of local elevations of calcium and IP_3 in steering growth cones [59, 161]. Recent methods allow manipulating the number of molecules released and have put a lower bound on the minimum number of Netrin-1 and Sema3A molecules required to achieve guidance [162]. However, only one axon can be observed per experiment, severely limiting the throughput of these techniques.

In the three-dimensional collagen gel assay, the cells of interest are grown in a tissue culture matrix made from extracellular matrix components such as collagen, laminin or matrigel. A gradient is generated by diffusion of a chemotactic factor secreted from cells or tissue in a gel block or by printing the cue directly on the gel [163–167]. A putative cue is determined to be attractive or repulsive based on the final distribution and lengths of axons. The classical 3D coculture assay using an explant of cells as the source of the factor of interest produces poorly quantified gradients. A 3D quantitative assay was designed to generate precise, reproducible and stable gradients. Lines of increasing concentration of a guidance cue are printed on a thin collagen gel where explants are embedded. The guidance molecules diffuse throughout the gel creating a smooth gradient that can last for days [166]. This study reveals extremely high sensitivity of dorsal root ganglion neurons to NGF gradients of very shallow steepness [166].

2.4.2 Substrate-bound chemotaxis assays

The second category of assays involves substrate-bound cues (Fig 2.7). The first studies using substrate-bound molecules appeared in 1970s using UV irradiation of neuronal culture substrates to denature proteins [168]. The patterned dishes showed the permissivity of laminin for axonal growth [169]. The stripe assay was developed by Friedrich Bonhoeffer and colleagues

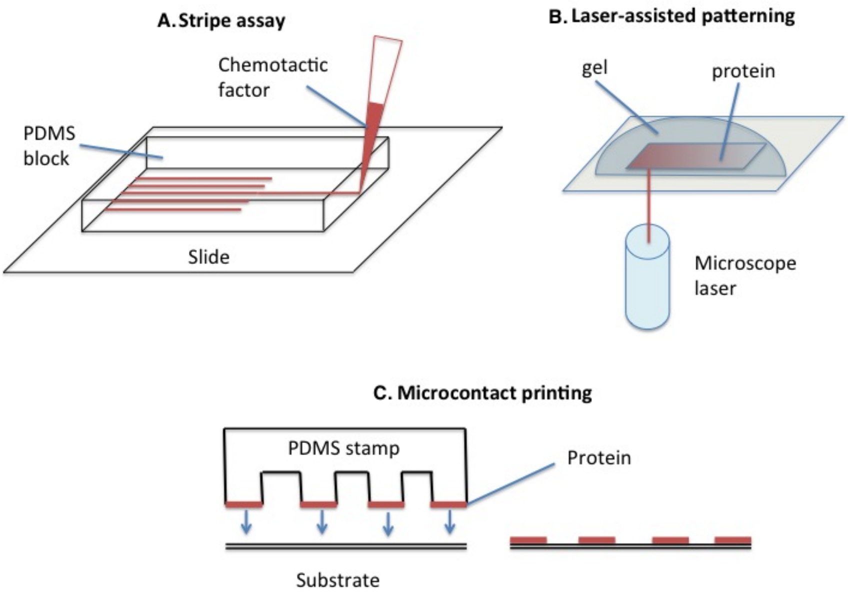

Figure 2.7: **Substrate-bound chemotaxis assays**. A. In the stripe assay, the chemotactic factor is sucked through the patterns of a PDMS block or a silicon matrix and adheres to a substrate. The PDMS block is then removed and cells are grown on the substrate. B. Laser-assisted patterning uses a microscope laser to crosslink a protein of interest in a block of gel with high precision. C. Microcontact printing uses a PDMS stamp soaked in the chemotactic factor to print the pattern on a substrate.

to study axon guidance in the context of the development of topographic maps in the chick retino-tectal system [170–173]. The assay uses a silicon matrix of channels filled with protein solution to create striped carpets on the culture substrate [174]. The stripe assay led to the discovery of new guidance cues and mechanisms in the thalamic, olfactory and hippocampal systems [175–177].

Patterning of the substrate can also be achieved by ink-jet printing [178]. Discontinuous gradients can be achieved by changing the number of drops per point [179]. Microcontact printing uses an engraved stamp soaked in the cue to print patterns on a substrate through contact. A gradient can be created by varying the spacings of stripes on the stamp. Using this technique, a study revealed growth cones of chick temporal retinal axons stop at distinct zones in ephrinA5 gradients of different steepnesses [180]. Continuous substrate-bound gradients can also be produced by microfluidic mixers which allow proteins to be adsorbed with non-uniform density to the substrate [181].

Bioactive molecules can be covalently immobilised on surfaces using photoimmobilisation. High-resolution gradients can be created by varying the intensity or the number of rastering scans of the laser to modulate the density of the molecule [182–184]. Another similar method exploits photobleaching of fluorescently tagged molecules to bind them to glass substrates via the generation of free radicals with sub-cellular resolution. This method was used to create a gradient of immobilised laminin peptides that could elicit axon guidance [185]. This method can be extended to more than one guidance cue by increasing the number of fluorescent tags and laser lines [185].

These patterning methods have recently been extended to three-dimensional assays. In the three-dimensional photolithographic patterning technique known as two-photon laser scanning lithography scans, a microscope laser scans over the regions of interest of a non-adhesive hydrogel soaked in a cell adhesion molecule resulting in its crosslinking to the hydrogel. This can create precise adhesive microenvironments to guide cell migration [186].

2.4.3 Microfluidics assays

Although the assays mentioned above have been useful in identifying new guidance cues and signalling molecules, they are not suitable for a more quantitative analysis largely because of their irreproducibility. Axonal response is often only characterised in a binary fashion (guidance vs. no guidance). A more quantitative understanding requires a stable, known concentration field and data from many growth cones under the same condition. In order to develop a quantitative analysis of growth cone movements in diffusible gradients, we developed a new microfluidic device based on the design in [181], which will be discussed in detail in Chapters 5 and 6. In this section, we describe the general principles of microfluidics and some results that have come from this technology.

Microfluidics is a new class of technologies that can overcome many of the shortcomings of previous assays. The term “microfluidics” refers to micron to millimetre sized devices that can process microscopic volumes of fluid through a series of channels and chambers [187]. They are becoming valuable tools for studies at the single-cell level for a variety of cell types, including neutrophils [188, 189], bacteria [190, 191], viruses [192, 193], cancer cells [194, 195], stem cells [196, 197], sperm [198, 199] and neurons [200, 201].

In general, the first step to building a microfluidic chip involves drawing the design using computer software. The design is printed out and used to create a photomask. This is placed

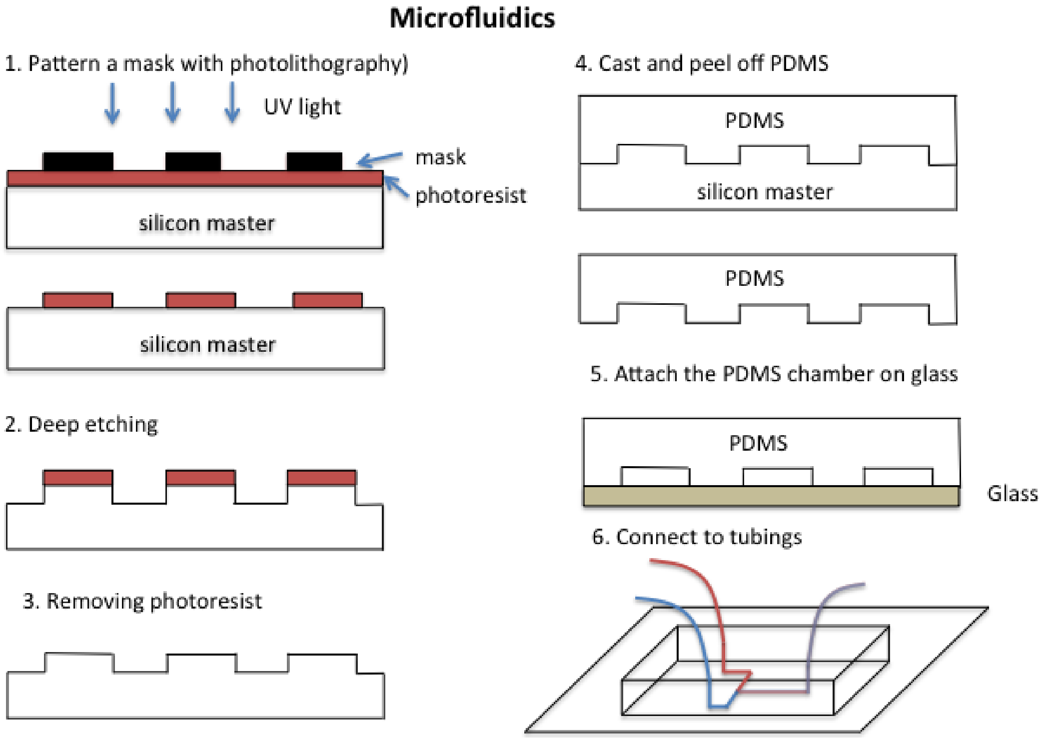

FIGURE 2.8: **Microfluidic assays**. A silicon master is patterned using photolithography. PDMS is poured on the master and peeled off after it has solidified. The PDMS stamp is attached on a glass or plastic substrate by surface activation using plasma.

over a silicon substrate coated with a thin layer of photoresist. When exposed to UV light, the photoresist will harden only in areas patterned on the mask and the rest will be washed away, leaving the pattern on the master mould. PDMS (Polydimethylsiloxane) is poured on the master and peeled off and bonded on plastic or glass (Fig 2.8). PDMS is optically transparent, biocompatible, permeable to gases and can be sterilised using standard techniques [201].

Stable concentration profiles can be created by using solutions of different concentrations flowing at a constant speed through microscopic channels. The solutions split and mix in different proportions to form a gradient which can be maintained indefinitely and is not subject to decay through diffusion. The microscopic flows are laminar, stable and maintain a concentration gradient across the chamber. The physics of laminar flow is well understood and the gradient can be predicted using modelling software, allowing the design of complex gradients.

Microfluidic technology presents an advantage over conventional *in vitro* techniques traditionally used in studying chemotaxis. They offer the ability to precisely control and create stable, reproducible gradients and to observe multiple cells simultaneously over long periods of time.

Microfluidics is cheap because the volume of expensive media can be limited [201]. Microfluidic devices are also capable of creating multiple gradients with user-defined spatiotemporal distribution.

Microfluidics has made valuable contributions to studying axon guidance. A flow-based microfluidic device revealed that axons of rat hippocampal neurons were oriented toward higher concentration of substrate-bound laminin [181]. Bound gradients of netrin-1 and brain-derived neurotrophic factor (BDNF) can polarise the initiation and turning of hippocampal neurons [202]. In another study, embryonic *Xenopus* spinal neurons were repelled by linear gradients of soluble BDNF and responded to the gradient's slope instead of the absolute concentration [203]. Whitesides *et al.* designed the devices that have been used for many biological applications, such as experiments on chemotaxis of human neutrophils, cancer cells and *Dictyostellium* [204]. We will later utilise this design for our study of superior cervical ganglion neurons in nerve growth factor gradients.

Chapter 3

How receptor diffusion influences gradient sensing

Apart from formatting, this chapter is identical to H. Nguyen, P. Dayan, G.J. Goodhill, ”How Receptor Diffusion Influences Gradient Sensing,” *Journal of Royal Society Interface*, vol 12: 20141097, 2015. DOI: 10.1098/rsif.2014.1097.

Abstract

Chemotaxis, or directed motion in chemical gradients, is critical for various biological processes. Many eukaryotic cells perform spatial sensing, i.e. detect gradients by comparing spatial differences in binding occupancy of chemosensory receptors across their membrane. In many theoretical models of spatial sensing, it is assumed for simplicity that the receptors concerned do not move. However, in reality, they undergo diverse modes of diffusion, and can traverse considerable distances in the time it takes such cells to turn in an external gradient. This sets a physical limit on the accuracy of spatial sensing, which we explore using a model in which receptors diffuse freely over the membrane. We find that the Fisher information carried in binding and unbinding events decreases monotonically with the diffusion constant of the receptors.

3.1 Introduction

Chemotaxis, involving movements that are oriented relative to chemical gradients, is an important and widespread phenomenon among eukaryotic cells. This mechanism is critical to neuronal growth cones navigating to their targets in the developing nervous system [5, 30], neutrophils migrating to the site of inflammation [14] and sperm cells swimming towards an egg [205]. In the first steps of chemotaxis, ligand molecules in the environment bind to membrane chemoreceptors, activating them and triggering downstream signalling events [4]. In spatial sensing, cells estimate the external concentration difference across their spatial extent, a comparison whose corruption by noise from the stochastic nature of ligand binding, and downstream signalling has been well studied [95, 96, 206–209]. In order to interpret information about binding, cells need to have information about the positions of the receptors concerned. These are generally in constant motion in the membrane, which is itself a highly complex structure that is compartmentalized on multiple scales [105, 210]. Receptors undergo diverse modes of diffusion, including fast and slow diffusion, confinement and drift [211–214]; further, differential fluidity of membrane lipids can affect the lateral movement of proteins embedded in it [105], and the diffusive properties of receptors can also be influenced by oligomerization or association with the membrane skeleton [211, 215]. Since movement of receptors due to diffusion represents a smearing out of the spatial information they can provide about local concentration, diffusion will reduce the accuracy of gradient sensing. However, the importance of this depends on exactly how much information is lost; a quantity that has not previously been calculated. Receptor diffusion also poses a challenge that cannot be addressed by previous models of gradient sensing which assume immobile receptors and a fixed binding probability for each receptor [96]. Snapshot measurements are no longer sufficient for the cell to infer the gradient as it has lost the information of how long each receptor has been unbound and where it has been, therefore the binding probability of the receptor. This requires the cell to integrate over time to estimate the gradient.

Here we model the effects of receptor diffusion on a one-dimensional ‘cell’, under the assumption that it is only bound receptors that signal and thus reveal their locations, leaving the cell uncertain about the locations of unbound receptors. We extend a previous model [216] which assumed that the cell has knowledge of the amount of time the receptors are bound and where the bindings happen. We compare the accuracy of gradient sensing for receptors which are

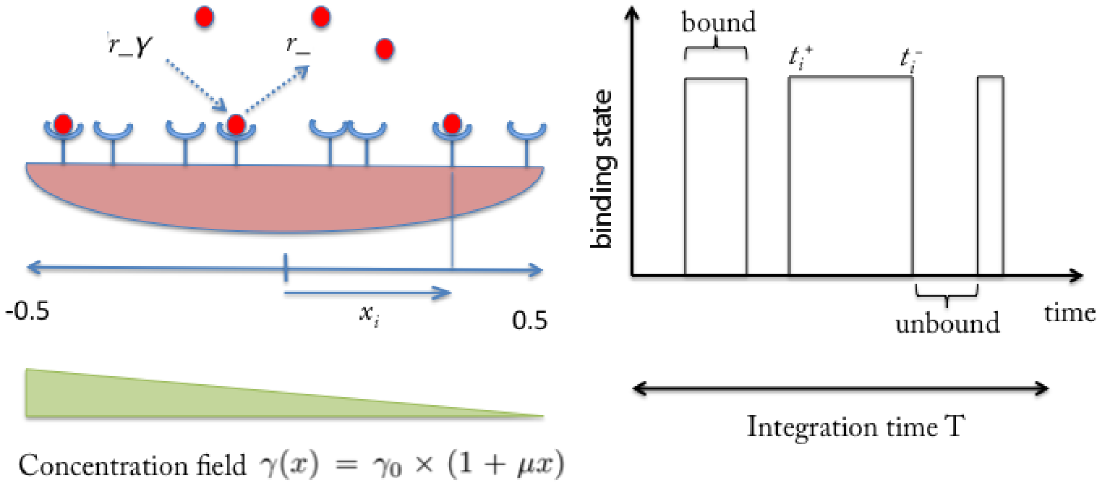

FIGURE 3.1: **Schematic of sensing model.** Ligand molecules bind to, and unbind from, receptors with transition rates r_+ and r_-, where $r_+ = r_-\gamma$ and γ is proportional to the ligand concentration. The cell collects information about bound receptors over an integration time T.

mobile versus immobile. We show analytically how receptor diffusion reduces the accuracy of gradient sensing, and demonstrate that the reduction increases monotonically with the diffusion constant.

3.2 Model

3.2.1 Immobile receptors

Previous models of gradient sensing assume receptors are immobile [95, 96, 99, 206, 217]. Each receptor has a fixed probability of binding with ligand molecules that depends on the local ligand concentration at the receptor's position. This gives a probability distribution over possible binding patterns. It allows the cell to estimate the gradient from a snapshot measurement of the binding pattern of all the receptors at a single instance. However, if the assumption of immobility is not imposed, each receptor will have changing probability of binding that depends on its motion of through the concentration field. This requires the cell to integrate information over time to sense the gradient. Endres [218] proposes a different model in which the cell integrates information over time from the binding and unbinding sequences to infer the gradient. It was later adopted by [216] to derive the upper limit on the information the cell can obtain assuming it knows both the unbound time and the number of bound/unbound transitions. We expand our current model based on that original model in [216] to examine the effects of receptor mobility.

We first describe the original model in [216] (Fig 3.1). The cell is represented as a one-dimensional array of uniformly distributed receptors whose binding and unbinding provide information about the concentration field that the cell experiences. The receptor state is modelled as a continuous time, two-state Markov process. The transition rate from bound to unbound is r_- and the transition rate from unbound to bound is $r_+ = Ck_+$, where C is the local concentration of ligand at the location of the receptor. The dissociation constant is $K_d = r_-/k_+$. Writing $\gamma = C/K_d$ for the dimensionless concentration, we have the relationship between the on- and off-rates: $r_+ = \gamma r_-$. The cell has N receptors at positions normalized by the cell diameter $\vec{x} = (x_1, x_2, ..., x_N) \in [-0.5, 0.5]$ and the linear concentration field is $\gamma(x) = \gamma_0 \times (1 + \mu x)$ with μ being the gradient, or the fractional change of the concentration, that the cell has to estimate.

It was assumed in [216] that all receptors start out unbound. The times of binding and unbinding events were written as t^+_{ji} and t^-_{ji}, where j is the j^{th} receptor and i is the i^{th} transition. Similarly, the positions of the receptors at those times were denoted x^+_{ji} and x^-_{ji}. The cell was assumed to know about the timings and positions of the binding/unbinding events of the receptors via downstream signalling mechanisms that were not specified.

This implies that binding and unbinding are Poisson processes with rates r_- and $r_-\gamma(x)$. For a Poisson process with rate r, the probability density of an event happening at a particular time t after another event at time 0 is $r\exp(-rt)$. Therefore, the probability density for the j^{th} receptor to remain bound from t^+_{ji} to t^-_{ji} is

$$P_b(t^+_{ji}, t^-_{ji}) = r_- \exp\left(-r_-(t^-_{ji} - t^+_{ji})\right)$$

and denoting $\gamma_j = \gamma(x_j)$, the probability density of it being unbound from t^-_{ji} to $t^+_{j,i+1}$ is

$$P_u(t^-_{ji}, t^+_{j,i+1}) = r_-\gamma_j \exp\left(-r_-(t^+_{j,i+1} - t^-_{ji})\gamma_j\right)$$

Therefore, the likelihood of observing a time series $\left\{t_{ji}^{+}, t_{ji}^{-}\right\}$ given concentration $\gamma(x_j)$ at the location of receptor j is:

$$\mathcal{L}(T_j^B, T_j^U, \gamma_j) \propto r_-^{M_j^*} (r_-\gamma_j)^{M_j} \exp\left(-r_-T_j^B - r_-T_j^U\gamma_j\right) \tag{3.1}$$

where M_j is the number of unbound-bound transitions, and M_j^* is the number of bound-unbound transitions (which is equal to M_j or $M_j - 1$ because each binding event apart from the last one must be followed by an unbinding event), T_j^U, T_j^B are the total time unbound and bound respectively for receptor j. The maximum likelihood approach is the optimal unbiased estimation and calculates the value of the parameter of interest that maximises the likelihood of observing the data. Recalling that $\gamma_j = \gamma_0(1 + \mu x_j)$ where μ is the gradient and setting the derivative of the loglikelihood to zero, the maximum likelihood estimate of the gradient is given by:

$$\mu_{MLE} = \frac{\sum_j \left(-r_-\gamma_0 x_j T_j^U + M_j x_j\right)}{\sum\limits_j M_j x_j^2} \tag{3.2}$$

This equation implies that the association between the receptor position and its unbound time carries gradient information, similar to a previous result that found unbound intervals carry concentration information [218]. As time increases, the variance of this estimate approaches the limit set by the Fisher Information:

$$\mathrm{var}(\mu_{MLE}) \geq \left\langle -\frac{\partial^2 \log P}{\partial \mu^2} \right\rangle^{-1} = \left\langle \sum\nolimits_j M_j x_j^2 \right\rangle^{-1} \tag{3.3}$$

As the average time it takes the receptor to become bound is $1/\gamma r_-$ and the average time the receptor remains bound is $1/r_-$, during the integration time T, the average number of unbound-bound transitions will approximately be:

$$\langle M_j \rangle \approx \frac{T}{\left(\frac{1}{r_-} + \frac{1}{\gamma_0 r_-}\right)} = \frac{T r_- \gamma_0}{\gamma_0 + 1}$$

Hence the Fisher Information can be approximated as:

$$\mathcal{I} = \left\langle -\frac{\partial^2 \log P}{\partial \mu^2} \right\rangle \approx \left(\sum\nolimits_j \frac{T r_- \gamma_0}{\gamma_0 + 1} x_j^2 \right)^{-1} \tag{3.4}$$

3.2.2 Mobile receptors

We now consider the more realistic case in which receptors are free to diffuse on the cell surface, starting from uniform randomly distributed initial positions. For simplicity, we consider the case that receptors continuously diffuse and ignore periods of confinement or drift. As unbinding events are independent of the receptor's position, their probability remains unchanged from above.

Binding events are treated as a Cox process, i.e. a inhomogeneous Poisson process whose intensity is also stochastic.

Consider a single receptor (thus temporarily ignoring subscript j) that starts from initial position $x(0) = x_0$ and diffuses freely by Brownian motion independently of the binding (although the binding is not independent of the motion). In this case, the binding rate $\lambda(t)$ is a function of the random position $x(t)$ of the receptor at time t: $\lambda(t) = r_-\gamma_0(1 + \mu x(t))$. We utilise the concept of the Brownian bridge: i.e., Brownian motion fixed at two ends $x(t_{i-1}^-) = x_{i-1}^-$ and $x(t_i^+) = x_i^+$. According to the Cox process, the conditional density of a binding event at t_i^+ given the unbinding time t_{i-1}^- and the path $\omega_i = (x_{i-1}^- ... x_i^+)$ of the receptor is:

$$p(t_i^+|t_{i-1}^-, \omega_i) = \lambda(x_i^+) \exp\left(-\int_{\omega_i} \lambda\left(x(t)\right) dt\right) \tag{3.5}$$

where the first term accounts for the binding at t_i^+ and the second for the absence of binding over the time period (t_{i-1}^-, t_i^+). Marginalizing over the unknown trajectory ω_i, the conditional likelihood given only the positions (x_{i-1}^-, x_i^+) at the unbinding and binding times is:

$$P(t_i^+|t_{i-1}^-, x_{i-1}^-, x_i^+) = \lambda(x_i^+)\mathbb{E}\left[\exp\left(-\int_{\omega_i} \lambda\left(x(t)\right) dt\right)\right] \tag{3.6}$$

where $\lambda(x) = r_-\gamma_0(1 + \mu x)$ is the binding rate, and the expectation is taken with respect to the diffusion bridge but subject to the boundary condition $-0.5 < x < 0.5$, as the receptors can only diffuse on the cell. We now proceed to find the expectation terms in the expression above:

$$\begin{aligned}\mathbb{E}\left[\exp\left(-\int_{\omega_i}\lambda\left(x(t)\right)dt\right)\right] &= \mathbb{E}\left[\exp\left(-\int_{\omega_i} r_-\gamma_0\left(1+\mu x(t)\right)dt\right)\right] \\ &= \exp\left(-r_-\gamma_0(t_i^+ - t_{i-1}^-)\right)\mathbb{E}\left[\exp\left(-r_-\gamma_0\mu\int_{\omega_i} x(t)dt\right)\right] \qquad (3.7)\end{aligned}$$

The receptors undergo Brownian motion: $x(t) = x_0 + \sqrt{D}W(t)$, where $W(t)$ is a standard Brownian motion and D is the diffusion constant. Only paths that satisfy the condition $-0.5 < x(t) < 0.5$ contribute to the expectation. We assume that the concentration is sufficiently high such that the probability of paths beyond this boundary is very small (i.e. $\left\langle t_{i+1}^+ - t_i^-\right\rangle D = \frac{D}{\gamma r_-} \ll R^2$ and R is the radius of the cell). This assumption implies that including such paths does not affect the calculation. We discretize t into n intervals of $\delta t = (t_i^+ - t_{i-1}^-)/n$:

$$\int_\omega x_s ds = \lim_{n\to\infty}\sum_{k=1}^n x_k\delta t$$

For brevity, we write $a = x_{i-1}^-$, $b = x_i^+$, $t_1 = t_{i-1}^-$, $t_2 = t_i^+$. The distribution of $x(t)$ at time $t \in (t_1, t_2)$ is normal with mean:

$$a + \frac{t-t_1}{t_2-t_1}(b-a)$$

and the covariance between $x(s)$ and $x(t)$ with $s < t$ is

$$D\frac{(t_2-t)(s-t_1)}{t_2-t_1}$$

Therefore x_k's are the components of a multivariate normal vector with mean:

$$\vec{X} = \left[a + \frac{\delta t}{t_2-t_1}(b-a), ...a + \frac{(n-1)\delta t}{t_2-t_1}(b-a), b\right]$$

and $n \times n$ covariance matrix:

$$\Gamma_{kl} = D\frac{1}{t_2-t_1}k(n-l)(\delta t)^2 \quad k < l$$

We know that the sum of the components of a multivariate normal vector has a univariate normal distribution with mean

$$\alpha = \sum_k X_k = na + \frac{n(n+1)/2}{t_2 - t_1}(b-a) \approx n(a+b)/2$$

and covariance

$$\beta^2 = \sum_{k,l} \Gamma_{k,l} = \delta t^2 n^2 (n+1)^2/12(t_2 - t_1) \approx Dn^2(t_2 - t_1)/12$$

Therefore $\int_\omega x_s ds$ is also a normal random variable with mean $(x_i^+ + x_{i-1}^-)(t_i^+ - t_{i-1}^-)/2$ and variance $D((t_i^+ - t_{i-1}^-)^3/12$. Thus $\exp\left(-r_-\gamma_0\mu \int_\omega x_s ds\right)$ follows a log-normal distribution with mean m and variance v:

$$\begin{aligned} m &= \exp(\beta^2/2 + \alpha) \\ &= \exp\left(\frac{r_-^2\gamma_0^2\mu^2 D(t_i^+ - t_{i-1}^-)^3}{24} - \frac{r_-\gamma_0\mu(x_i^+ + x_{i-1}^-)(t_i^+ - t_{i-1}^-)}{2}\right) \\ v &= (\exp(\beta^2) - 1)\exp(\beta^2 + 2\alpha) \end{aligned}$$

The likelihood of a full observation $\{t_i^+, t_i^-, x_i^+, x_i^-\}$:

$$\begin{aligned} &\mathcal{L}(t_i^-, x_i^-, t_i^+, x_i^+ ... x_0) \\ &\propto \prod_{i=1}^{M} r_- \exp\left(r_-(t_i^- - t_i^+)\right)\lambda(x_i^+)\, \mathbb{E}\left[\exp\left(-\int_{\omega_i} \lambda(x(t))ds\right)\right] \\ &\propto \exp\left(\sum_{i=1}^{M} r_-^2\gamma_0^2\mu^2 \frac{D(t_i^+ - t_{i-1}^-)^3}{24} - \frac{r_-\gamma_0\mu(x_i^+ + x_{i-1}^-)(t_i^+ - t_{i-1}^-)}{2}\right) \times \prod_{i=1}^{M}(1 + \mu x_i^+) \end{aligned} \tag{3.8}$$

The maximum likelihood estimate of the gradient is:

$$\mu_{MLE} = \frac{\sum_{i,j}^{M_j,N} \left(-r_-\gamma_0(x_{ji}^+ + x_{j,i-1}^-)(t_{ji}^+ - t_{j,i-1}^-)/2 + x_{ji}^+\right)}{\sum_{i,j}^{M_j,N} \left(-r_-^2\gamma_0^2 D(t_{ji}^+ - t_{j,i-1}^-)^3/12 + x_{j,i}^{+2}\right)} \tag{3.9}$$

A caveat of this calculation is that it assumes the cell knows the time series and locations of each receptor individually. That is, a pair of unbinding and binding events can be associated with each other, even though the receptor may have mingled with other receptors in the meantime. This is a reasonable assumption when diffusion is not too large or receptor density is low, such that the receptors are far enough apart and move sufficiently small distances for the cell to be able to distinguish between them after their unbinding period.

The Fisher information for this case is:

$$\mathcal{I}=\left\langle -\frac{\partial^2 \log P}{\partial \mu^2}\right\rangle = \left\langle \sum_{i,j}^{M_j,N}\left(-r_-^2\gamma_0^2 D\frac{(t_{ji}^+ - t_{j,i-1}^-)^3}{12} + x_{j,i}^{+2}\right)\right\rangle \tag{3.10}$$

As expected, we can see that as D increases, the Fisher Information decreases and when $D = 0$, this expression reduces to equation 3.3. This expression cannot be calculated analytically but needs to be approximated. In order to approximate the first term, we recall that $\langle M_j\rangle \approx Tr_-\gamma_0/(\gamma_0+1)$ and $t^+ - t^-$ is an exponentially distributed variable with mean $1/(r_-\gamma_0)$, thus $\langle (t^+ - t^-)^3\rangle = 6/(r_-\gamma_0)^3$. Thus

$$\left\langle -\sum_{i,j}^{M_j,N} r_-^2\gamma_0^2 \frac{D(t_i^+ - t_{i-1}^-)^3}{12}\right\rangle \approx -\frac{TND}{2(\gamma_0+1)} \tag{3.11}$$

We adopt the approach of [219] to approximate the second term as follows:

$$\left\langle \sum_{i,j=1}^{M_j,N} x_{ji}^{+2}\right\rangle \approx \sum_{j}^{N}\int_0^T r_- \langle b_j(t)\rangle\, x_j^2(t)dt \tag{3.12}$$

with

$$\langle b_j(t)\rangle = \frac{r_-\gamma(x_j(t))}{r_- + r_-\gamma(x_j(t))} \approx \frac{r_-\gamma_0}{r_- + r_-\gamma_0}$$

This approximation leads to:

$$\mathcal{I} = \left\langle -\frac{\partial^2 \log P}{\partial \mu^2}\right\rangle \approx \frac{TND}{2(\gamma_0+1)} + \left\langle \sum_{j}^{N}\int_0^T \frac{r_-\gamma_0}{1+\gamma_0} x_j(t)^2 dt\right\rangle \tag{3.13}$$

We now need to calculate $\langle x(t)^2\rangle$ subject to the boundary condition $-0.5 < x(t) < 0.5$. We employ the reflection principle to calculate this term. For a freely diffusing receptor without any boundary condition, the probability density function of $x(t)$ given the initial position x_0

is:

$$p(x_0, 0; x, t) = \frac{1}{\sqrt{2\pi D t}} \exp\left(-\frac{(x - x_0)^2}{2Dt}\right)$$

If the receptor is reflected back when it reaches the boundary ±0.5, then the probability density function of $x(t)$ is equal to that of a Brownian motion starting at x_0 plus those of its reflections across the boundary.

$$p(x_0, 0; x, t) = \frac{1}{\sqrt{2\pi D t}} \left[\exp\left(-\frac{(x - x_0)^2}{2Dt}\right) + \sum_{n=-\infty}^{\infty} \exp\left(\frac{(n - x_0 - x)^2}{2Dt}\right)\right]$$

We assume the receptors cannot diffuse too much while being unbound, thus we include only two reflection terms, the mean square displacement is:

$$\begin{aligned}\int_0^T \langle x(t)^2\rangle dt = \sqrt{DT/2\pi}\, &\exp(-\frac{(1.5 - x_0)^2}{2DT})(0.5 - x_0) + \exp(-\frac{(0.5 - x_0)^2}{2DT})(-1.5 + x_0)\\ &+ \exp(-\frac{(0.5 + x_0)^2}{2DT})(-0.5 + x_0) - \exp(-\frac{(0.5 - x_0)^2}{2DT})(0.5 + x_0)\\ &+ \exp(-\frac{(1.5 + x_0)^2}{2DT})(0.5 + x_0) - \exp(-\frac{(0.5 + x_0)^2}{2DT})(1.5 + x_0))\\ &+ 1/2(-(DT + (-1 + x_0)^2)\mathrm{erf}(\frac{-1.5 + x_0}{\sqrt{2DT}}) + (DT + (1 + x_0)^2)\mathrm{erf}(\frac{1.5 + x_0}{\sqrt{2DT}})\\ &- (\mathrm{erf}(\frac{0.5 + x_0}{\sqrt{2DT}}) + \mathrm{erf}(\frac{0.5 - x_0}{\sqrt{2DT}}))(2x_0 + 1))\end{aligned}$$

These approximations are good as long as $\frac{D}{\gamma r_-} \ll R^2$. Diffusion constants of relevant receptors such as epidermal growth factor receptor (EGFR) and platelet derived factor receptors (PDFR) are of order $10^{-2}\mu m^2/s$ while the dissociation constants are of order $10^{-1}s$, suggesting that this approximation is valid at K_d and higher concentrations [220–224].

We plot the quality of the approximations as a function of D in Fig. 3.2. Here, we used a discrete approximation to diffusion by initializing the positions of the receptors as uniform random numbers between -0.5 and 0.5 and, at each time step, making each move left or right a fixed amount $\sqrt{D}$, being 'reflected' if it hits -0.5 or 0.5. The probability of being bound at each time step is $r_-\gamma(x(t))$, if currently unbound, and the probability of becoming unbound is r_-, if currently bound. Each simulation is 20000 timesteps, the actual length of each timestep is arbitrary (we set it to 0.02 second). The off-rates of 0.001-0.01 per timestep are equivalent to 0.05-0.5/s. The unit of the diffusion constant is R^2/t, with R being the radius of the cell (5 μm) and t being the duration of each timestep. In a real cell with dimensions of $R = 5\mu m$

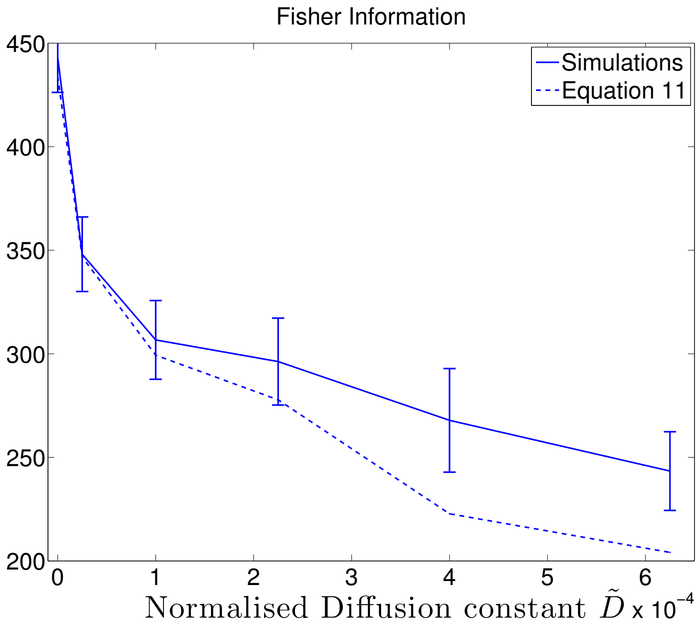

FIGURE 3.2: **Diffusion reduces information.** Comparison of Fisher Information as a function of the diffusion constant D between simulations and the approximation in equation 3.13 ($r_{-} = 0.002, \gamma_0 = 10$). The faster the receptors diffuse, the less information the measurement contains.

and receptor diffusion constant of $10^{-2}\mu m^2/s$, in a few minutes, the receptors will have a mean square displacement on the order of R^2. In our simulations, after 20000 timesteps, for example, with a diffusion constant of 10^{-4}, the mean square displacement of each receptor is $2R^2$, the same order of magnitude as real receptors. Thus, the parameters are biologically plausible. The approximations of the Fisher Information are within 20% of the empirical values, taken to be the variance of the maximum likelihood estimates over 2000 trials lasting 20000 timesteps. The quality of the approximation worsens as D increases because the estimation of $\langle x(t)^2 \rangle$ only included two reflection terms, whereas higher order terms might become more significant in that regime. The Fisher Information is the inverse of the variance of the estimates (Eq. 3). For example, if the Fisher Information $\mathcal{I} = 400$ for a gradient of 10 %, this means the lower limit on the variance is 0.0025 and the estimates will be a normal distribution with mean 10 % and standard deviation of 5%. Recalling that the Fisher Information sets the limit on how accurate the estimate of the gradient can be (Eq. 3), Fig 3.1 implies that when receptor diffusion is taken into account, the cell has to integrate over a longer time to achieve the same accuracy as without receptor diffusion.

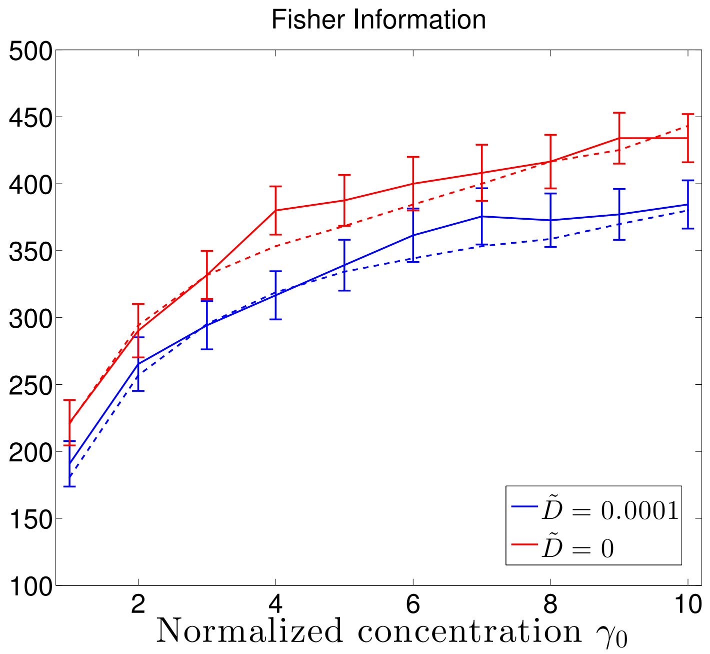

FIGURE 3.3: **Information increases with concentration.** The Fisher Information as a function of the normalized concentration γ_0 with $r_- = 0.005$. The solid lines represent simulations and the dashed lines represent approximations in equation 3.13. As γ_0 increases, more binding and unbinding events happen, resulting in greater Fisher information.

3.3 Delayed signalling

Fig 3.3 and 3.4 show that as the concentration or the off-rate increases, more binding and unbinding events will happen, so that the measurement contains more information.

So far, we have assumed that as soon as the receptors become bound, they start signalling immediately. However, in reality it takes time for the receptor to change its conformational state or for the downstream cytosolic molecules to be recruited to the activated receptor. Therefore there might be a delay between ligand binding and the initiation of the signalling cascade. It has been suggested that bound receptors slow down significantly so that the cell can pinpoint exactly where the extracellular signal is coming from [105]. Whether this has any benefit for gradient sensing is not clear. By calculating the Fisher information in the case that the receptors can still move freely after being bound, we find that the cell gains no extra information about the gradient if the bound receptors are immobilized. We now consider the consequence of a time delay between the binding event and the report of the location, implying that the latter does not reflect exactly where the receptor was at the time of binding. We denote the positions at which the transduction pathways for receptor i are activated and inactivated

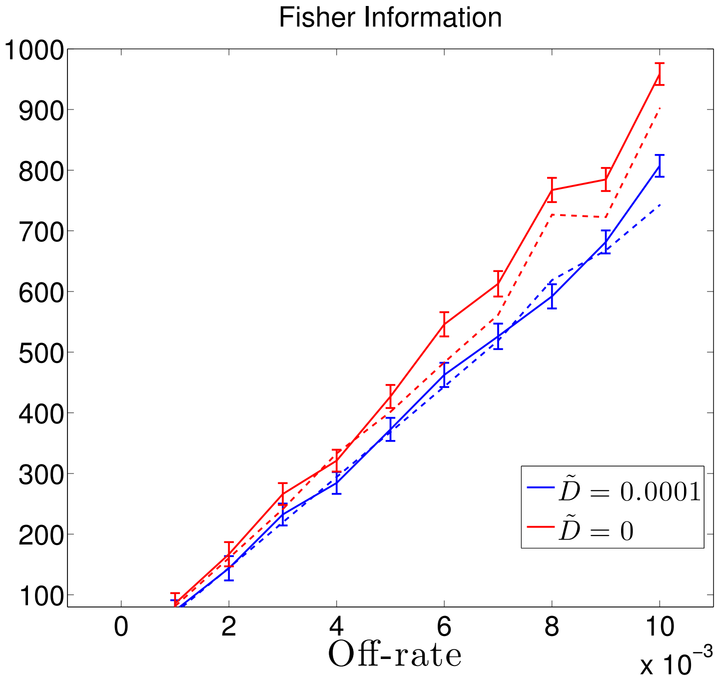

Figure 3.4: **Information increases with off-rate.** The Fisher Information as a function of the off-rate r_- with $\gamma_0 = 10$.

as y_i^-, y_i^+. Now, instead of knowing exactly where the binding and unbinding events occur on the surface, the cell only has access to partial information about these locations, represented by Gaussian distributions $x^+ \sim \mathcal{N}(y^+, \sigma_y), x^- \sim \mathcal{N}(y^-, \sigma_y)$. If we assume that the time delay t_d is constant (a stochastic delay is also possible), then the uncertainty in the location of the binding/unbinding events will be $\sigma_y = \sqrt{Dt_d}$. We can now examine how this extra noise adds to the uncertainty of the gradient estimate. The conditional probability of binding now has an expectation taken over all possible paths with all

$$
\begin{aligned}
&P(t_i^+|t_{i-1}^-, y_{i-1}^-, y_i^+, \sigma_y)\\
&= \mathbb{E}_{P(x_i^+, x_{i-1}^-)}\left[\lambda(x_i^+)\mathbb{E}_{P(\omega)}\left[\exp\left(-\int_{t_i^-}^{t_{i+1}^+}\lambda\left(x(t)\right)dt\right)\right]\right]\\
&\propto \int \exp\left(\frac{r_-^2\gamma_0^2\mu^2 D(t_i^+ - t_{i-1}^-)^3}{24} - r_-\gamma_0\mu\frac{(x_i^+ + x_{i-1}^-)(t_i^+ - t_{i-1}^-)}{2}\right)\\
&\times \gamma_0(1+\mu x_i^+)\exp\left(-\frac{(x_i^+ - y_i^+)^2 + (x_{i-1}^- - y_{i-1}^-)^2}{2Dt_d}\right)dx_i^+ dx_{i-1}^-\\
&= \exp(-C(y_i^+ + y_{i-1}^-) + C^2 D t_d))\gamma_0(1 + y_i^+\mu - CDt_d\mu)\\
&\times \exp\left(\frac{r_-^2\gamma_0^2\mu^2 D(t_i^+ - t_{i-1}^-)^3}{24}\right)
\end{aligned}
$$

where $C = r_-\gamma_0\mu(t_i^+ - t_{i-1}^-)/2$

The Fisher Information is now

$$
\mathcal{I}_{del} = \mathcal{I} - \left\langle \sum_{i,j}\left(-\frac{r_-^2\gamma_0^2(t_{j,i}^+ - t_{j,i-1}^-)^2}{2} + r_-\gamma_0(t_{j,i}^+ - t_{j,i-1}^-)\right)Dt_d\right\rangle \approx \mathcal{I}
$$

where $\mathcal{I}$ is the Fisher Information given in equation 3.10 since $\left\langle (t_{j,i}^+ - t_{j,i-1}^-)^2/2\right\rangle \approx 1/(r_-\gamma_0)^2$ and $\left\langle t_{j,i}^+ - t_{j,i-1}^-\right\rangle \approx 1/(r_-\gamma_0)$. This means the delay in signalling does not add any noise to gradient sensing. Thus surprisingly, in this framework, confining the cytoplasmic signal to the precise place where the extracellular signal was received (i.e. immobilizing the receptor following binding) is not substantially beneficial to the cell.

3.4 Discussion

The lipid bilayer that forms cell membranes has been investigated intensively. The traditional view of the membrane as a homogeneous fluid has been challenged and replaced by a more sophisticated model incorporating heterogeneous microdomains [105]. Membrane receptors display complex behaviour, including hop diffusion, drift and confinement [105]. In a gradient, receptors can have differential binding rate of ligand, changing diffusion constants among different populations of receptors or undergo redistribution [17, 225, 226]. The non-uniformity in motion has been hypothesized to be due to the existence of lipid rafts or the compartmentalization actin-based membrane-skeleton 'fences' and anchored transmembrane protein 'pickets'. These microdomains might serve as signalling platforms where the activated receptor can interact with cytosolic signalling molecules recruited to the cell membrane. Receptors might change their affinity with lipid rafts upon ligand binding and activate different signalling pathways depending on whether they are in a lipid raft or not. Thus receptor lateral diffusion allows the cell to have more flexibility to regulate receptor signalling. However, the impact of this lateral mobility is to reduce the positional information that receptors carry about the signal they receive from the environment.

The lateral diffusion of receptors can vary depending on receptor and cell type. However, well-known receptors in chemotaxis such as EGFR in human mammary epithelial cells, TrkA in growth cones and PDGF in fibroblasts have diffusion constants of the order of $10^{-10} cm^2/s$ [213, 221, 227]. In the typical time that it takes cells to respond to chemical gradients, i.e., around a few minutes, the mean square displacement of receptors can be comparable to cell size (several micrometers). These parameter ranges suggest that diffusion of receptors can contribute to a significant loss of information during that integration time.

Here we investigated the role of this receptor diffusion in spatial gradient sensing, exploring for simplicity the simple scenario in which receptors diffuse freely without periods of drift or confinement. We modelled the cell as a one dimensional array of independent chemoreceptors whose bindings with ligand molecules depend on their stochastic positions on the cell surface. We considered the regime of fast diffusion of the ligand molecules, and thus neglected rebinding of particles. We assumed that only bound receptors signal their positions to the cell, with the timings of the bindings also being known, either precisely or after a time delay. One possible biological signalling mechanism is a non-uniform distribution of signalling molecules such that the concentration is proportional to the distance from the receptor to the cell centre. However, there has not been experimental evidence to support this speculation. We also assume that when receptors are bound, downstream effectors are constantly activated. This might lead to further downstream reactions that produce signalling molecules in an accumulative manner. The bound time can then be estimated by the accumulated concentration of this end product.

We derived an approximation to the Fisher Information about the concentration gradient, and showed the approximation error to be small given a long integration time. One caveat with the model is that the cell has to associate times and positions with particular receptors. If the receptors are sparse and far apart, then this would be straightforward. However, if in a typical binding time the receptors can cross, then this is harder. It may be that the cell carries out a simpler computation that will underperform the maximum likelihood estimate. Alternatively, receptors may signal constitutively, and so provide a means of being tracked. The gradient measurement comes from a quantity that depends on both the unbound intervals and the receptor position (Eq 2). If the receptors can move and the cell only takes snapshot measurements, the cell has completely lost the information of how long each receptor has been unbound or where it has been. Receptor diffusion therefore necessitates integration of information over a time window, which is not necessary when the receptors are assumed to be immobile.

Interestingly, in another model [228], Iyengar and Rao found that there is a phase transition in the strategies as a function of receptor density and efficiency. At low receptor density, the optimal strategy is freely diffusing receptors. At higher density, the optimal solutions are either static receptors on a regular lattice grid or a mix of freely diffusing receptors and clusters. The model however assumes that each receptor can sample the environment directly at regular time intervals. Our model is more flexible in that the receptors do not sample the gradient itself but have to infer it from sequences of binding and unbinding events. We also do not impose measurements at regular intervals or known locations of receptors at all time.

Using both simulations and the analytical approximations, we found that receptor diffusion can cause a substantial reduction in the quality of gradient sensing. This quality reduces roughly linearly with the diffusion constant of the receptors. This is intuitive because the cell knows less about where the receptors have been before they became bound. Consistent with a previous paper [216], the performance increases with ligand concentration and the unbinding rate. This is to be expected, because the higher these parameters, the more binding/unbinding events occur and the more information the measurement contains. This model also assumes that the cell has infinite precision in measuring the binding delay. A more realistic mechanism for measuring time intervals by the production of second messenger molecules has been discussed in more detail in [216]. We have not considered the issue of noise coming from downstream signalling. We investigate the optimal possible performance only limited to noise due to ligand binding.

We also considered a more realistic model in which the binding events are not registered immediately by the cell, but only after a time delay. By the time the bound receptors start signalling, they will have moved to another position, implying that the cell will have lost precise knowledge as to where the binding events happened. However, this does not substantially affect the information the measurement carries. The information about the gradient is in the unbound time and the positions where the receptors become bound and unbound. As the time delay is constant, the unbound time is unchanged. The locations of the receptors have some more uncertainty however, we expect that due to unbiased random motions, the discrepancies between the actual and signalled positions will cancel each other out, thus not affecting the estimate. Amongst other things, this implies that immobilization is unlikely to serve the purpose of preserving the signal, and might rather have a different effect such as facilitating the interactions between the bound receptors and the cytosolic molecules or other membrane-bound proteins.

Chapter 4

The influence of receptor positioning on chemotactic information

Apart from formatting, this chapter is identical to H. Nguyen, P. Dayan, G.J. Goodhill, "The Influence of Receptor Positioning on Chemotactic Information," *Journal of Theoretical Biology*, vol 360, pp. 95-101, 2014.

Abstract

Chemotaxis, or gradient following, is important in many biological systems, but suffers from noise. How receptors are positioned on the cell or sensing device influences the quality of the inferences they can support about the gradient, suggesting that their configuration might be optimised. We show that for an elliptical sensing device, inhomogeneous receptor placement could be a potential approach for cells to eliminate bias in the posterior distribution of the gradient direction. We use information theory to calculate the mutual information between the gradient and the binding pattern, thus finding the optimal receptor arrangement for gradient sensing.

4.1 Introduction

Many biological systems rely on chemotaxis. These include neutrophils migrating to sites of inflammation [14], the slime mold *Dictyostelium discoideum* hunting for food [6], and neuronal growth cones navigating to find their targets in the developing nervous system [5, 30]. The ability of such sensing devices to detect chemical gradients depends sensitively on unavoidable stochastic fluctuations due to the limited numbers of receptors, intracellular signalling molecules, and ligand molecules available in the gradient itself [206, 207]. Detecting a gradient can thus be seen as a paradigmatic problem of reasoning in the face of uncertainty [95]. Here we focus on noise due to receptor binding fluctuations.

A powerful approach for analysing such problems is to consider the *optimal* statistical inference that an ideal observer would perform [95–97, 217, 229, 230]. This involves combining available information with prior assumptions. However a critical unanswered question is the extent to which some spatial distributions of receptors admit better gradient detection than others. Starting from the familiar model of the sensing device (hereafter 'cell') as a two-dimensional ellipse with receptors distributed on the surface, we derive the mutual information between the gradient and binding pattern as a target quantity to maximise in order to achieve optimal inference.

A recent theoretical analysis shows that with a uniformly distributed set of receptors, an elliptical cell can make incorrect inferences about the gradient when the concentration and the gradient steepness are low [99]. Surprisingly, the cell has a strong bias to infer that the gradient is parallel to the minor axis, regardless of the actual gradient direction. This is because equal spacing of receptors on a non-circular surface leads to highly unequal variances in the estimates of the x and y components of the gradient. Here we show that this can be overcome by a nonuniform placement of receptors so that the inference is free of biases due to the shape of the cell.

4.2 Model

We consider the cell as estimating the gradient $\vec{\mu}$ of a spatial function $C(\vec{r}) = C_0 \exp(\vec{\mu}\vec{r})$. Receptor positions $\vec{r}$ are relative to the 'standard' length scale $10\mu m$ and the gradient $\vec{\mu}$ is

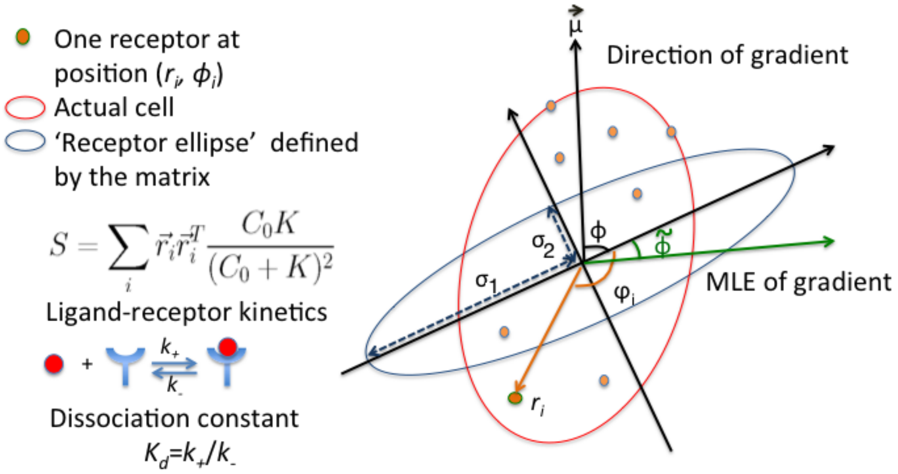

FIGURE 4.1: Schematic problem representation. The orange dots represent receptors. The axes of the coordinate system are the two eigenvectors of the 'receptor ellipse' matrix $S = \sum_i \vec{r}_i \vec{r}_i^T \frac{C_0 K}{(C_0+K)^2}$ (blue) which might or might not coincide with the axes of the actual cell (red). The two axes of the 'receptor ellipse' determines the properties of gradient estimation.

dimensionless. We assume that the information available about C consists of independent binary random variables b_i representing the bound and unbound states of a set of n receptors located at positions $\vec{r}_i \in \mathcal{R}^2, i = 1...n$. Standard Michaelis-Menten kinetics implies the binding probability of each receptor is

$$P(b_i = 1) = \frac{C(\vec{r}_i)}{(K_d + C(\vec{r}_i))}$$

with K_d being the dissociation constant. The likelihood function of the complete binding state is:

$$\mathcal{L}_{\mathbf{b}}(\vec{\mu}, C_0) = \prod_{i=1}^{n} \left(\frac{C(\vec{r}_i)}{K_d + C(\vec{r}_i)} \right)^{b_i} \left(\frac{K_d}{K_d + C(\vec{r}_i)} \right)^{1-b_i}$$

whose logarithm is

$$\ln \mathcal{L}_{\mathbf{b}}(\vec{\mu}, C_0) = \sum_{i=1}^{n} b_i \ln \left(\frac{C(\vec{r}_i)}{K_d} \right) - \sum_{i=1}^{n} \ln \left(\frac{K_d + C(\vec{r}_i)}{K_d} \right)$$

The cell should combine likelihood information with its *a priori* estimate of the gradient. The prior has two components: the first is the direction $\phi = \angle \vec{\mu}$, which is conventionally represented as a von Mises distribution as in [97]:

$$P(\phi) = \frac{\exp(\kappa \cos(\phi - \delta))}{I_0(\kappa)},$$

where δ is the prior bias of the cell regarding the gradient direction, κ is the strength of bias, and $I_0(\kappa)$ is the modified Bessel function of the first kind. This prior could be determined by previous measurements, as in a filtering scheme, or by an intrinsic bias. The second component is the strength $s = |\vec{\mu}|$ of the gradient. For convenience, we considered a simple, half-Gaussian form for this $P(s) = 2\sqrt{\beta/\pi}H(s)\exp(-\beta s^2)$, where β parameterizes the uncertainty. This favors small gradients, a conclusion invited by the exquisite sensitivity of many sensing systems [95, 231]. However, its precise form is not expected to influence the results very strongly, provided it is smooth and covers the range of relevant values. We consider these two components to be independent, making the overall prior $P(s,\phi) = P(s) \times P(\phi)$.

Expanding the likelihood function to second order around 0 in $\vec{\mu}$:

$$\ln \mathcal{L}_{\mathbf{b}} \simeq \sum_i b_i \ln \frac{C_0}{K} + n \ln \frac{K}{C_0 + K} + \vec{\mu}\Delta_{\mathbf{b}}\vec{r} - \frac{1}{2}\vec{\mu}^T S \vec{\mu} \tag{4.1}$$

where

$$\Delta_{\mathbf{b}}\vec{r} = \sum_{i=1}^{n}(\vec{r}_i b_i - \frac{C_0}{C_0 + K}), S = \sum_i \vec{r}_i\vec{r}_i^T \frac{C_0 K}{(C_0 + K)^2} \tag{4.2}$$

leads to the maximum likelihood estimate (MLE)

$$\vec{\mu}^{\mathrm{ML}} = S^{-1}\Delta_{\mathbf{b}}\vec{r}$$

This formula is more general than that derived in [96] since it does not assume a circular cell or a uniform distribution of receptors on the cell's surface. The average binding probability $\mathbb{E}[b_i]$ at each receptor is:

$$\mathbb{E}[b_i] = \frac{C_0 exp(\vec{\mu}\vec{r})}{K + C_0 exp(\vec{\mu}\vec{r})} \approx \frac{C_0}{C_0 + K} + \frac{C_0 K}{(C_0 + K)^2}\vec{\mu}\vec{r},$$

and therefore

$$\mathbb{E}[\vec{\mu}_{\mathbf{b}}^{ML}] = \frac{C_0 K}{(C_0 + K)^2}(\vec{r}^T\vec{r})S^{-1}\vec{\mu} = \vec{\mu},$$

confirming that the expectation of $\vec{\mu}^{ML}$ over all possible binding patterns is the actual gradient.

In the large n limit, the properties of the MLE ensures that $\vec{\mu}^{ML} \to \mathcal{N}(\vec{\mu}, S^{-1})$. S^{-1} is the covariance matrix of the maximum likelihood estimate and only depends on the positions of the receptors, not the shape of the cell. We call S the 'receptor matrix' as it ultimately encodes information about the receptor arrangement. As S is a symmetric matrix it can be diagonalised, implying that there exists a coordinate system defined by the two eigenvectors of S (shown in Fig. 4.1) such that the two orthogonal components of $\vec{\mu}^{ML}$ are uncorrelated, and their variances are the eigenvalues of the matrix S^{-1}. Henceforth, we will define all angles relative to this coordinate system, with x, y axes identified with the first and second eigenvectors of S^{-1}. Note that these axes will in general be different from the axes of the elliptical cell.

We define $1/\sigma_1^2$ and $1/\sigma_2^2$ to be the corresponding eigenvalues of the matrix S^{-1} and

$$\begin{bmatrix} Z_1 \\ Z_2 \end{bmatrix} = \begin{bmatrix} \mu_x^{ML}\sigma_1^2 \\ \mu_y^{ML}\sigma_2^2 \end{bmatrix} = \begin{bmatrix} \sum \sigma_1^2 b_i (r_i \cos\varphi_i - \frac{C_0}{K+C_0}) \\ \sum \sigma_2^2 b_i (r_i \sin\varphi_i - \frac{C_0}{K+C_0}) \end{bmatrix}$$

where r_i, φ_i are the positions of the receptors in polar coordinates, and thus recover the familiar Gaussian approximation for the likelihood function [96]:

$$P(\vec{Z}|s,\phi) = \frac{1}{2\pi\sigma_1\sigma_2} \exp\left[-\frac{(Z_1 - s\sigma_1^2\cos\phi)^2}{2\sigma_1^2} - \frac{(Z_2 - s\sigma_2^2\sin\phi)^2}{2\sigma_2^2}\right]$$

4.3 Eliminating bias

For certain receptor distributions for which $\sigma_1 \neq \sigma_2$, the variances in μ_x^{ML} and μ_y^{ML} can differ, causing the cell consistently to estimate the gradient direction

$$\tilde{\phi} = \tan^{-1}\left(\frac{\mu_x^{ML}}{\mu_y^{ML}}\right)$$

parallel to its minor axis at low concentration or gradient steepness, as seen in [99]. At first glance, this result might be counter-intuitive. However, if $\sigma_1 \gg \sigma_2$, equivalent to a 'receptor ellipse' elongated in the x direction, the cell can much more easily detect the asymmetry in the concentration in the x direction (low variance) than in the y direction (high variance). The inequality in variances leads to bias in the MLE due to the highly nonlinear nature of the function $\tan^{-1}$. Therefore, at shallow gradients the estimated direction of the gradient has a tendency to favor the minor axis (the y direction). The estimated direction also has higher

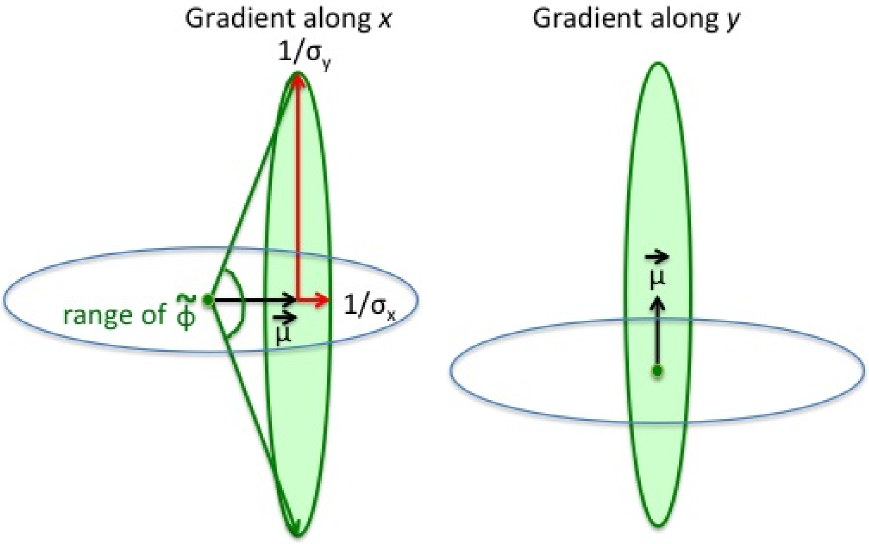

FIGURE 4.2: The blue ellipse is the receptor ellipse as defined in Fig. 4.1, the green ellipse represents the confidence ellipsoid of the maximum likelihood estimates $\vec{\mu}^{ML}$ of the gradient and the black line is the true gradient. The actual cell is not shown. The bias of the cell to estimate the gradient direction $\tilde{\phi}$ along the minor axis of the receptor ellipse can be explained by the unequal variances $1/\sigma_x^2$ and $1/\sigma_y^2$. If the true direction points in the x axis, the variance of the ML estimates $\tilde{\phi}$ can be large. If the true direction is parallel to the y axis, the variance is much lower. In both cases, $\tilde{\phi}$ strongly favors values close to $\pm\pi/2$.

variance if the true gradient is in the x direction than if it is in the y direction as illustrated in Fig. 4.2.

For simplicity we assume that the cell is only interested in the gradient direction rather than its magnitude. In order to find the maximum *a posteriori* (MAP) estimate for the actual gradient direction ϕ_{true}, we seek to solve $\hat{\phi}_{MAP} = \arg\max_\phi P(\phi|\vec{Z})$ where

$$\begin{aligned} P(\phi|\vec{Z}) &\propto \int P(\vec{Z}|s,\phi)P(s)P(\phi)ds \\ &\propto \frac{1}{\sqrt{A}}\exp(\frac{B^2}{4A} - C)(1 - \mathrm{erf}(-\frac{B}{2\sqrt{A}})) \end{aligned} \tag{4.3}$$

where

$$\begin{aligned} A &= 1/2(\sigma_1^2\cos^2\phi + \sigma_2^2\sin^2\phi) + \beta \\ B &= Z_1\cos\phi + Z_2\sin\phi \\ C &= \frac{Z_1^2}{2\sigma_1^2} + \frac{Z_2^2}{2\sigma_2^2} - \kappa\cos(\phi - \delta) \end{aligned}$$

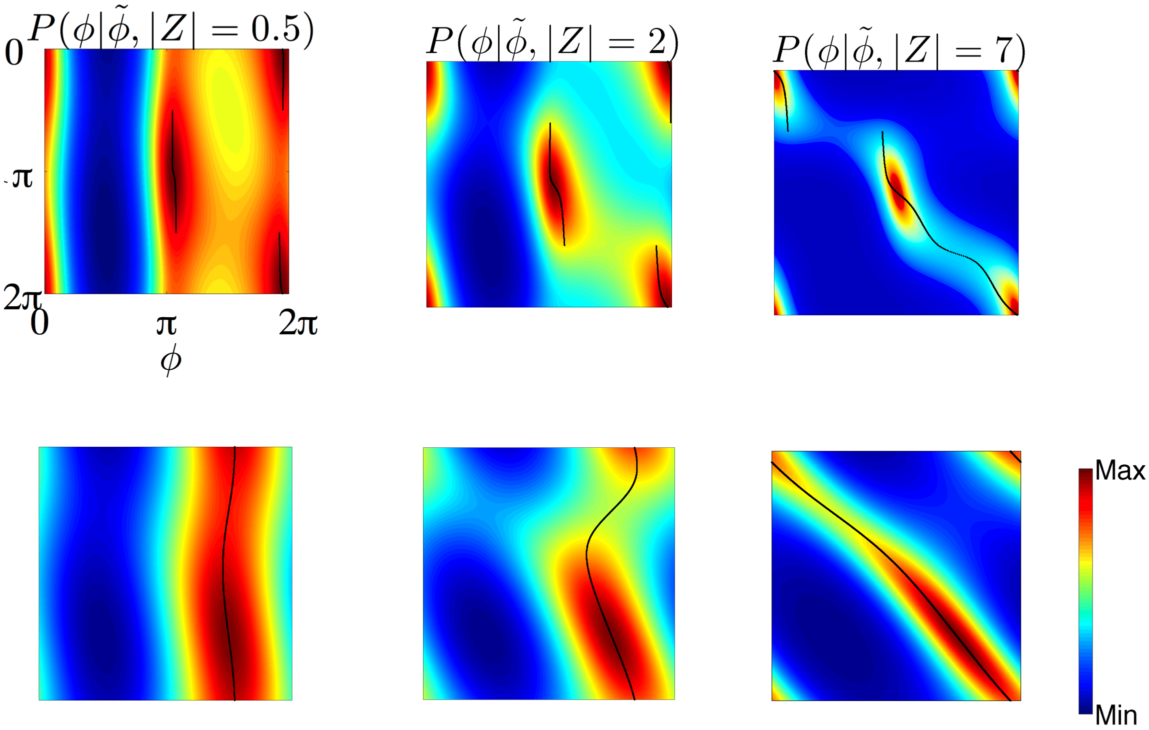

FIGURE 4.3: Numerical comparison of the posterior distribution of the gradient direction ϕ given the maximum likelihood estimate $\tilde{\phi}$ for $\sigma_1 = 3, \sigma_2 = 7$ (row 1) and $\sigma_1 = \sigma_2 = 5$ (row 2), using the same prior $P(s, \phi) \propto \exp(0.5\cos(\phi+\pi/2))\exp(-2s^2)$. The maximum and minimum in each plot from left to right are (0.06, 0.25), (0.05, 0.34), (0.19, 0.99), (0.08, 0.26), (0.06, 0.30), (0.02,0.50). The black lines represent the maximum *a posteriori* estimates. The first row shows a clear nonuniform quality in the posterior distributions given different $\tilde{\phi}$. The posterior distribution is sharper when $\tilde{\phi}$ aligns with σ_1 ($\tilde{\phi} = 0$ or π) than when $\tilde{\phi}$ aligns with σ_2 ($\tilde{\phi} = \pi/2$ or $3/2\pi$).

Denoting

$$\tilde{\phi} = \tan^{-1}\left(\frac{Z_1/\sigma_1^2}{Z_2/\sigma_2^2}\right)$$

as the maximum likelihood estimate of the gradient direction and $|Z| = \sqrt{Z_1^2 + Z_2^2}$ representing the asymmetry in the receptor occupancy, we numerically calculate $P(\phi|\tilde{\phi}, |Z|)$ for different values of $|Z|$. Figure 4.3 shows the relationship between $\tilde{\phi}$ and the posterior estimate of the gradient direction at three values of $|Z| = 0.5, 2$ and 7, for $\sigma_1 = 3, \sigma_2 = 7$ (row 1), which we loosely call the 'elliptical' case and $\sigma_1 = 5, \sigma_2 = 5$ (row 2), the 'circular' case. The black lines represent the maximum *a posteriori* estimates for each case. The prior distribution for all cases is

$$P(s, \phi) \propto \exp(0.5(\phi + \pi/2))\exp(-2s^2).$$

For the elliptical case, the posterior is influenced by three factors: the bias due to the inequality between σ_1 and σ_2 represented by the term A in Eq. 3, the prior represented by the last term of C, and the data captured by the term B. Since A is minimized when $\phi = 0$ or π, there is a strong bias for the posterior distribution to peak at 0 or π (aligned with the direction of σ_1), which can overwhelm the prior when $|Z|$ is weak (column 1). As $|Z|$ becomes stronger, this tendency remains, and although ϕ_{MAP} follows $\tilde{\phi}$ more closely (column 3), the cell is more precise at estimating gradient directions pointing along the minor axis of the receptor ellipse than along the major axis, consistent with the results in [99]. The posterior is more sharply peaked when $\tilde{\phi} = 0$ or π because when B is maximum, A is minimum, and vice versa. If $\tilde{\phi} = \pi/2$ or $3\pi/2$, the maxima and minima of B and A are 'in phase', therefore reducing the variance. At lower values of $|Z|$ (column 1 and 2), there are discontinuities in ϕ_{MAP} around $\phi = \pi/2$ and $3\pi/2$. The graph in column 2 shows the intermediate case between the two extremes of the estimates being dominated by the shape bias (column 1) and dominated by the binding observation.

In contrast, the circular case does not have the bias due to the shape (row 2). If $|Z|$ is weak, the gradient estimates are dominated by the prior. When $|Z|$ is large, the maximum a posteriori estimates become almost equal to the maximum likelihood estimates $\tilde{\phi}$ (row 2, column 3). The posterior distribution is more sharply peaked when $\tilde{\phi}$ is near the prior mean $3\pi/2$, meaning that the data agree with the prior knowledge.

The estimation problem can be visualized using numerical simulations. Recalling that Z_1, Z_2 are Gaussian random variables with means $s\sigma_1^2 \cos\phi_{true}, s\sigma_2^2 \sin\phi_{true}$ and variances σ_1^2 and σ_2^2 respectively, and arbitrarily setting the prior mean $\delta = -\pi/2$, we can visualize the distribution of all MAP estimates for various combinations of parameters (Fig. 4.4). The red plots are the posterior distribution $P(\phi|\vec{Z})$ weighted by the empirical probability density $P(\vec{Z}|s_{true}, \phi_{true})$. For $\sigma_1 \neq \sigma_2$ (columns 1-4, row 1), when the prior κ is weak and the gradient s is shallow, the estimates are strongly biased toward the minor axis of the 'receptor ellipse' S (cf [99]). The discontinuities of ϕ_{MAP} at angles parallel to the major axis of the 'receptor ellipse' are also observed, consistent with row 1 of Fig. 4.2. When the gradient is stronger (row 2), the estimates follow the true gradient more faithfully, and the performance is better when the true gradient is aligned with the minor axis than when it is aligned with the major axis (row 2, column 1 vs 3). Even when the prior is strong and the true gradient is shallow (row 3), the estimates can still be strongly influenced by the cell's bias towards the minor axis. When the

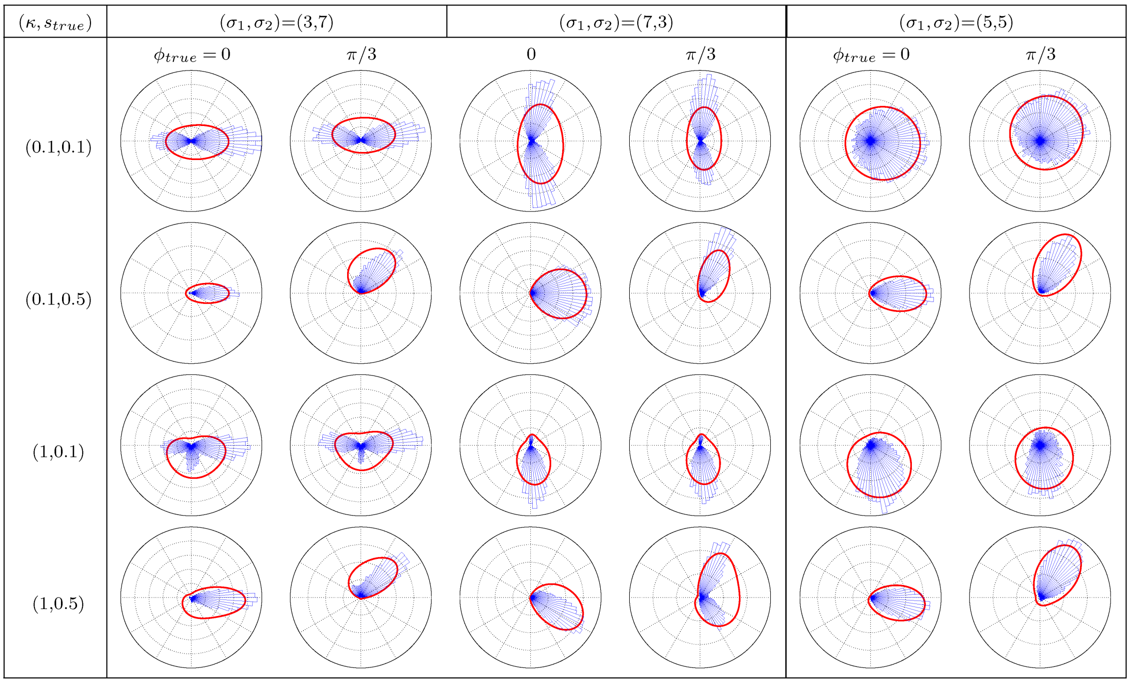

FIGURE 4.4: The distribution of MAP estimates for different gradient magnitudes and gradient direction priors. The x and y axes are defined by the matrix S as in Fig. 4.1. As the prior over s plays little role, we assume the same prior $P(s) = 2\sqrt{2/\pi}\exp(-2s^2)$ and $\delta = -\pi/2$ for all cases. Columns 1-4: $\sigma_1 \neq \sigma_2$. Columns 5-6: $\sigma_1 = \sigma_2$. The red plot is the distribution $P(\phi_{posterior}|s_{true}, \phi_{true})$, arbitrarily scaled for easy visualization.

prior and the gradient are both strong (row 4), the estimates represent a compromise between the true gradient, the prior and the minor axis.

Meanwhile, when $\sigma_1 = \sigma_2$ (columns 5-6), this bias towards the minor axis is eliminated. Note that it is not the case that there is a certain strength of receptor heterogeneity that is required to overcome the bias imposed by cell shape, rather any receptor arrangement that satisfies $\sigma_1 = \sigma_2$ is a solution. The distribution of the estimates then becomes a compromise between the prior directional bias and the measurements. If the actual gradient is shallow and the prior over the direction is weak (row 1), the estimates can fluctuate greatly however, the estimates stay centred around the true gradient direction. If the prior is strong (row 3), the measurements contribute little to the estimates. The estimates become more accurate when the prior is weak and the gradient is steep (row 2).

We now focus on the special case $\sigma_1 = \sigma_2 = \sigma$, since it avoids the bias coming from the spatial arrangement of the receptors. In the next section, we will show that by arranging receptors in such a way that σ is maximized, the cell maximizes the information about the gradient from its binding patterns. This optimization is subject to the constraint that the receptors have to

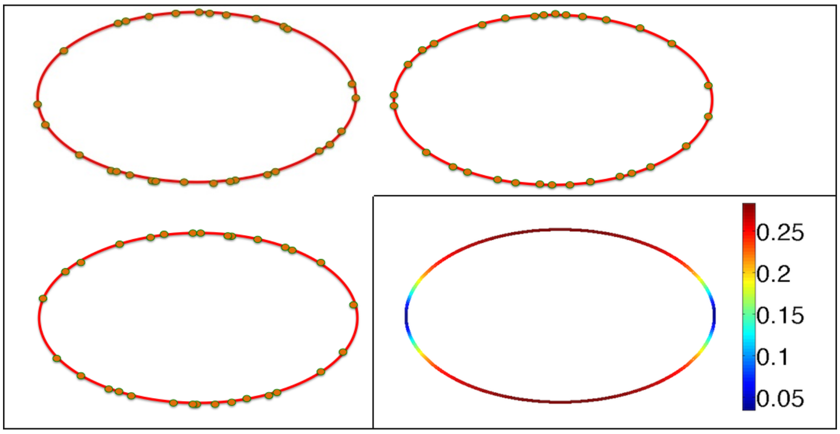

FIGURE 4.5: Some numerical examples of receptor distributions of 30 receptors on the surface of an elliptical cell that approximately satisfies the conditions $\sigma_1 = \sigma_2$ and $\sum r_i^2 \cos(\varphi_i)\sin(\varphi_i) = 0$. This was found by minimizing the determinant of the matrix S subject to the condition $\sigma_1 = \sigma_2$, using the command fmincon in MATLAB. The bottom right is the receptor probability density on the edge of the cell with major axis 0.83 in the x direction and minor axis 0.3. More receptors cluster around the minor axis of the cell because the receptors near the major axis contribute a large amount to σ_1 but little to σ_2. This distribution is independent of the prior bias or the actual gradient direction.

be on the cell surface. We know that the covariance of $\vec{\mu}^{ML}$ is the matrix S^{-1} with eigenvalues $1/\sigma_1^2$ and $1/\sigma_2^2$ from Eq. 2. Imposing $\sigma_1 = \sigma_2$ implies that the diagonal terms of S must be equal:

$$\sum \frac{C_0 K_d r_i^2 \cos^2\varphi_i}{(C_0+K_d)^2} = \sum \frac{C_0 K_d r_i^2 \sin^2\varphi_i}{(C_0+K_d)^2}$$

and maximizing σ requires maximizing the eigenvalue of S or maximizing $S_{11}S_{22} - S_{12}^2$. Thus the cross correlation term vanishes: $\Sigma r_i^2 \cos\varphi_i \sin\varphi_i = 0$. Recalling the ellipse equation $x^2/a^2 + y^2/b^2 = 1$, we can easily see that

$$\frac{\sigma_1^2}{a^2} + \frac{\sigma_2^2}{b^2} = \frac{nC_0K_d}{(C_0+K_d)^2} \tag{4.4}$$

which leads to

$$\sigma_1 = \sigma_2 = \frac{nC_0K_d}{(C_0+K_d)^2}\frac{a^2b^2}{a^2+b^2}.$$

Three example receptor arrangements that satisfy the above conditions are shown in Fig. 4.5. We found these numerically; however, extra insight into appropriate arrangements comes from finding the maximum entropy (i.e., least specified) distribution $P(\varphi)$ satisfying the constraints:

$$\int_0^{2\pi} r(\varphi)^2(\cos^2\varphi - \sin^2\varphi)P(\varphi)d\varphi = 0 \tag{4.5}$$

or

$$\int_0^{2\pi} \frac{ab(\cos^2\varphi - \sin^2\varphi)}{(a\sin\varphi)^2 + (b\cos\varphi)^2} P(\varphi) d\varphi = 0 \tag{4.6}$$

The resulting distribution is

$$P(\varphi) = C \exp\left[\frac{\nu(\cos^2\varphi - \sin^2\varphi)}{(a\sin\varphi)^2 + (b\cos\varphi)^2}\right] \tag{4.7}$$

where C and ν are constants such that $\int P(\varphi) = 1$. $\nu < 0$ if $a > b$ and $\nu > 0$ if $a < b$. This probability density is illustrated in the bottom right of Fig. 4.5. More receptors are distributed near the minor than the major axis.

4.4 Optimizing the Mutual Information

A canonical way to quantify the quality with which the receptors constrain the estimate of the gradient is via the mutual information between the gradient direction estimate and the binding pattern, defined as:

$$\mathcal{I}(\phi, \vec{Z}) = \int \log P(\phi|\vec{Z}) P(\phi, \vec{Z}) d\phi d\vec{Z} - \int \log P(\phi) P(\phi) d\phi$$

The second term is fixed, so we wish to maximize the first term, which can be written:

$$\int \log P(\phi, \vec{Z}) P(\phi, \vec{Z}) d\phi d\vec{Z} - \int \log P(\vec{Z}) p(\vec{Z}) d\vec{Z} \tag{4.8}$$

We consider the general case of both gradient direction and magnitude, and also compare with the mutual information for just direction. By defining

$$\tilde{s} = \sqrt{\left(\frac{Z_1}{\sigma_1^2}\right)^2 + \left(\frac{Z_2}{\sigma_2^2}\right)^2}$$

and simplifying Eq. 3, the joint probability of the binding pattern and the gradient is:

$$
\begin{aligned}
P(\phi,\vec{Z}) = &\int P(\vec{Z}|s,\phi)P(s)P(\phi)ds \\
=&\frac{\sqrt{\beta}}{2\pi^2\sigma^2 I_0(\kappa)\sqrt{2\sigma^2+4\beta}}\text{erfc}\left(-\frac{\tilde{s}\sigma\cos(\phi-\tilde{\phi})}{\sqrt{2\sigma^2+4\beta}}\right) \\
&\times\exp\left(\frac{(\tilde{s}\sigma\cos(\phi-\tilde{\phi}))^2}{2\sigma^2+4\beta}-\frac{\tilde{s}^2}{2}+\kappa\cos(\phi-\delta)\right)
\end{aligned}
\tag{4.9}
$$

The joint entropy between the gradient direction and binding pattern can be approximated as follows:

$$
\int \log P(\phi,\vec{Z})P(\phi,\vec{Z})d\phi d\vec{Z} \approx \log\left(\frac{\sqrt{2\beta}}{2\pi^2 e\sqrt{2\sigma^2+4\beta}\sigma^2 I_0(\kappa)}\right)+\frac{\kappa I_1(\kappa)}{I_0(\kappa)}
\tag{4.10}
$$

The quality of this approximation falls when β increases or when σ decreases (data not shown). However, when σ is greater than 5 and β less than 8, the error between the approximation and the exact integral is less than 7% and quickly approaches 0 as σ increases or β decreases.

We then obtain an approximation for $P(\vec{Z})$

$$
\begin{aligned}
P(\vec{Z}) = &\int_0^{2\pi}\int_0^{\infty} P(\vec{Z}|s,\phi)P(s)P(\phi)dsd\phi \\
=&\frac{\sqrt{\beta}}{2\pi^{5/2}\sigma^2 I_o(k)}\int\int \exp(\kappa cos(\phi-\delta)-\beta s^2) \\
&\times\exp\left[-\frac{(Z_1-s\sigma^2\cos\phi)^2+(Z_2-s\sigma^2\sin\phi)^2}{2\sigma^2}\right]dsd\phi \\
=&\frac{\sqrt{\beta}}{2\pi^{5/2}\sigma^2 I_o(k)}\exp\left(-\frac{Z_1^2}{2\sigma_1^2}-\frac{Z_2^2}{2\sigma_2^2}\right)\int\exp(\kappa\cos(\phi-\delta)) \\
&\times\exp(Z_1 s\cos\phi+Z_2 s\sin\phi-s^2(\frac{\sigma^2}{2}-\beta))dsd\phi
\end{aligned}
\tag{4.11}
$$

With $\tilde{s}=\sqrt{Z_1^2+Z_2^2}/\sigma, Z_1=\sigma\tilde{s}\cos\tilde{\phi}, Z_2=\sigma\tilde{s}\sin\tilde{\phi}$ and I_ν being the modified Bessel function of the first kind of order ν

$$
\begin{aligned}
P(\vec{Z}) =&\frac{\sqrt{\beta}}{2\pi^{5/2}\sigma^2 I_o(k)}\exp(-\frac{\tilde{s}^2}{2}) \\
&\times\int\exp(\sigma s\tilde{s}\cos(\phi-\tilde{\phi})+\kappa\cos(\phi-\delta)-s^2(\frac{\sigma^2}{2}-\beta))dsd\phi
\end{aligned}
\tag{4.12}
$$

Defining

$$\alpha = \arctan \frac{\kappa sin(\psi - \delta)}{s\eta + \kappa \cos(\psi - \delta)}, \qquad \gamma = \kappa \cos(\tilde{\phi} - \delta),$$

the integral can be written as:

$$\begin{aligned}
&\int\int \exp(\sqrt{\sigma^2 \tilde{s}^2 s^2 + \kappa^2 + 2\sigma\tilde{s}s\gamma} \cos(\phi - \tilde{\phi} + \alpha)) \times \exp(-s^2\sigma^2/2 - \beta s^2) ds d\phi \\
&= \int_0^\infty 2\pi I_o(\sqrt{\sigma^2 \tilde{s}^2 s^2 + \kappa^2 + 2\sigma\tilde{s}s\gamma}) \exp(-s^2(\frac{\sigma^2}{2} + \beta)) ds \\
&\approx 2\pi \int_0^\infty I_o(\sigma\tilde{s}s + \gamma) \exp(-s^2(\frac{\sigma^2}{2} + \beta)) ds \\
&\approx 2\pi \int (I_0(\gamma) I_0(\sigma\tilde{s}s) + 2I_1(\gamma) I_1(\sigma\tilde{s}s)) \exp(-(\frac{\sigma_1^2}{2} + \beta) s^2) ds \\
&= \sqrt{\frac{4\pi^3}{2\sigma^2 + 4\beta}} \exp(\frac{\sigma^2\tilde{s}^2}{4\sigma^2 + 8\beta}) \times [I_0(\gamma) I_0(\frac{\sigma^2\tilde{s}^2}{4\sigma^2 + 8\beta}) + 2I_1(\gamma) I_{1/2}(\frac{\sigma^2\tilde{s}^2}{4\sigma^2 + 8\beta})] \qquad (4.13)
\end{aligned}$$

using the following integral:

$$\int_0^\infty e^{-\alpha x^2} I_\nu(\beta x) dx = \frac{\sqrt{\pi}}{2\sqrt{\alpha}} exp(\frac{\beta^2}{8\alpha}) I_{\nu/2}(\frac{\beta^2}{8\alpha})$$

and the identity:

$$I_0(x + a) = \sum_{k=-\infty}^{\infty} I_k(x) I_{-k}(a) \approx I_0(x) I_0(a) + 2I_1(x) I_1(a)$$

for small a. Putting all the terms back together, we have:

$$\begin{aligned}
P(\vec{Z}) &= \int\int P(\vec{Z}|s, \phi) P(s) P(\phi) ds d\phi \\
&\approx \frac{\sqrt{\beta}}{\pi\sqrt{(2\sigma^2 + 4\beta)}\sigma^2 I_o(\kappa)} \exp(-\frac{\tilde{s}^2}{2} + \frac{\tilde{s}^2\sigma^2}{4\sigma^2 + 8\beta}) \\
&\quad \times [I_0(\gamma) I_0(\frac{\tilde{s}^2\sigma^2}{4\sigma^2 + 8\beta}) + 2I_1(\gamma) I_{1/2}(\frac{\tilde{s}^2\sigma^2}{4\sigma^2 + 8\beta})] \qquad (4.14)
\end{aligned}$$

When $\kappa < 0.4$, this approximation is accurate within 2% of the true value of $P(Z)$ for a wide range of parameters.

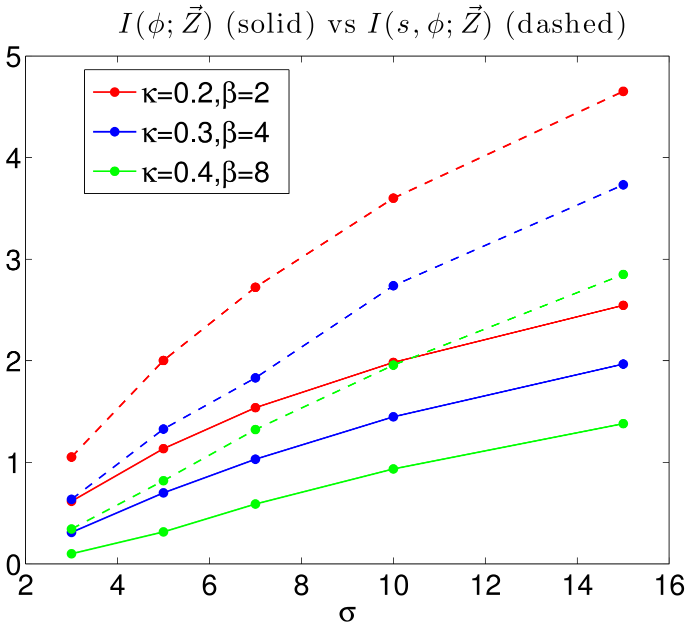

FIGURE 4.6: The mutual information between the binding pattern and the gradient (dashed line) or only the gradient direction (solid line). The former yields twice as much information.

Transforming to polar coordinates, i.e. $d\vec{Z} = \sigma^2 \tilde{s} d\tilde{s} d\tilde{\phi}$ and by numerical examination, we make the following approximations:

$$\int \log P(\vec{Z}) p(\vec{Z}) d\vec{Z} \approx \ln K + K(A_1 + A_2 + A_3 + A_4) \tag{4.15}$$

where

$$K = \frac{\sqrt{\beta}}{\pi\sqrt{2\sigma^2+4\beta}\,\sigma^2 I_0(\kappa)} \tag{4.16}$$

$$A_1 = \frac{-\left(\frac{1}{2\sigma^2}-\frac{1}{4\sigma^2+8\beta}\right)^2}{\left(\frac{1}{2\sigma^2}\left(\frac{1}{2\sigma^2}-\frac{1}{2\sigma^2+4\beta}\right)\right)^{3/2}}\,\frac{(\kappa^2+8)\pi}{8} \tag{4.17}$$

$$A_2 = \frac{\sigma^2\sqrt{2\sigma^2+4\beta}}{2\sqrt{\beta}}\,\frac{(3k^4+16k^2)\pi}{64} \tag{4.18}$$

$$\begin{aligned} A_3 = {} & \frac{(\kappa^2+8)\pi}{32}\,\frac{\sqrt{\frac{1}{2\sigma^2+4\beta}}}{\left(\frac{1}{2\sigma^2}-\frac{1}{2\sigma^2+4\beta}\right)^{3/2}} \\ & - \frac{(\kappa^2+8)\pi}{16}\,\frac{[\psi(1/2)-\ln(2\beta/\sigma_1^2)+\log(\pi)]}{\left(\frac{1}{2\sigma^2+4\beta}\left(\frac{1}{2\sigma^2}-\frac{1}{2\sigma^2+4\beta}\right)\right)^{1/2}} \end{aligned} \tag{4.19}$$

$$A_4 \approx \frac{1.08\kappa^2\pi\frac{1}{4\sigma^2+8\beta}}{\sqrt{\frac{\beta}{\sigma^4(2\sigma^2+4\beta)}}\left(\frac{1}{\sigma^2}-\frac{1}{2\sigma^2+4\beta}+\frac{2\sqrt{\beta}}{\sigma^2\sqrt{2\sigma^2+4\beta}}\right)} \tag{4.20}$$

with the constant 1.08 in A_4 derived from numerical approximation. For the range of parameters we tested ($\kappa < 0.4$, $\sigma \in (3, 15)$, $\beta \in (1, 8)$), the difference between the LHS and RHS of Eq. 16 is less than 3%.

Having obtained all component probabilities $P(\phi, s, \vec{Z})$, $P(\vec{Z})$, $P(\phi, s)$, we can contrast the mutual information calculated above with that in the case when the cell must estimate both the gradient steepness and gradient direction:

$$I(s, \phi; \vec{Z}) = \int P(\phi, s, \vec{Z}) \log \left(\frac{P(\phi, s, \vec{Z})}{P(\phi, s) P(\vec{Z})} \right) ds d\phi d\vec{Z} \tag{4.21}$$

As σ increases, the cell obtains more information about the gradient from each measurement (Fig. 4.6). This result makes sense intuitively because σ represents the 'strength' of the data, therefore the greater σ, the more information the measurement contains. σ is a function of the cell dimension and number of receptors, implying that the larger the cell or the more receptors the better. The joint estimation of both the gradient steepness and direction yields twice as much information as the direction estimate alone. The mutual information is also greater when the prior distribution is broader. This is consistent with previous results in [97], where the mutual information for a fixed gradient steepness was calculated and was found to decrease as κ is higher and approaches 0 in the limit $\kappa \to \infty$. Our calculation however is more general as it treats the gradient steepness also as an unknown. The general case $\sigma_1 \neq \sigma_2$ is beyond the scope of this paper. However, by discretizing Z_1, Z_2 to calculate the entropies, numerical calculations show that there exists an optimal combination of (σ_1, σ_2) such that the mutual information $\mathcal{I}(\phi, \vec{Z})$ is maximized. In Fig. 4.7, we illustrate this with one example of a cell with minor axis $a = 0.3$ and major axis $b = 0.83$ (to ensure the same area as a cell of diameter 1) with 4000 receptors at ligand concentration of K_d. Different arrangements of receptors result in different combinations of (σ_1, σ_2) that can satisfy Eq. 4, and the pair that gives the greatest amount of information about the gradient is (7, 17.8). This result implies that the quality of gradient sensing can be dependent on cell shape, though the lack of a formula for the general case $\sigma_1 \neq \sigma_2$ means that it is hard to address this analytically. However, in the case that the goal of the cell is to avoid bias at all cost by imposing $\sigma_1 = \sigma_2$, a highly elongated cell will be at a disadvantage compared to a circular cell of the same area because σ is constrained by the minor axis.

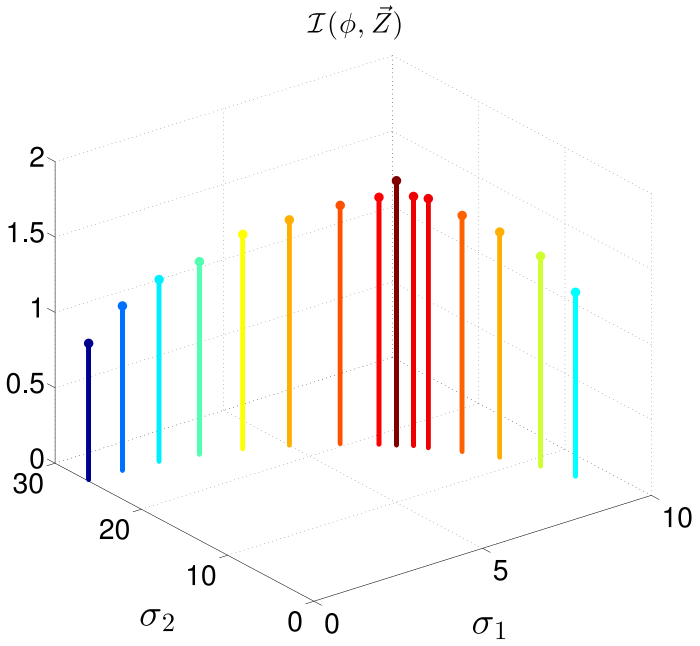

FIGURE 4.7: The numerically calculated mutual information between the binding pattern and the gradient directions for different combinations of (σ_1, σ_2) for the same cell shape $(a = 0.3, b = 0.83)$ and 4000 receptors at ligand concentration K_d. There exists an optimal pair $(\sigma_1 = 7, \sigma_2 = 17.8)$ which results in the greatest mutual information.

4.5 Discussion

We have formulated gradient detection as an optimization problem, addressing in particular the question of how receptors should be arranged in order to maximize the amount of information that the sensing device can gain about the gradient. The previous works we built on [95, 97–99, 230] derived the posterior distribution of the gradient by assuming a uniform distribution of receptors on the sensing device, and a large enough number of receptors such that the Gaussian approximation holds for the magnitude and the direction of the gradient. In contrast, we use the mutual information instead of Fisher information, which makes our approach more suitable to analyse the case of a finite or small number of receptors (thousands or fewer). We have derived a formula for the mutual information given a weak prior for the gradient. We also found good approximations for calculating the entropies with errors of less than 10% over a broad range of parameters. Our formulation is more general than [98], where the authors derived the mutual information for a fixed gradient magnitude.

The analysis presented here should apply to all cell types with independent receptors regardless of their distribution. This distribution of receptors depends on the particular cell type. In *Dictyostelium* and neutrophils, receptors are known to be uniformly distributed during chemotaxis [232, 233]. Meanwhile, in spatial gradients of epidermal growth factor, endocytosed receptors accumulate on the upgradient end of the mammary carcinoma cell [234]. There is some evidence that growth cone receptors redistribute in response to chemotactic gradients. When exposed to a GABA gradient (a neurotransmitter acting as a chemoattractant), receptors on neuronal growth cones cluster on the up-gradient side [226]. In growth cones that are undergoing attraction towards brain derived neurotrophic factor (BDNF), trkB receptors for BDNF are associated with lipid rafts that become localised to the side of the growth cone that is closest to the source of BDNF [235]. These results however do not affect the general findings in this chapter.

Although several theoretical and experimental works show that receptor cooperativity can play a significant role in chemotaxis [96, 236–238], the assumption of independent receptors is a still a useful simplification that has been widely used in many theoretical works [98, 99, 216, 239]. Cooperativity is difficult to analyze in the general framework in this paper. Without the assumption of symmetric distribution of receptors over the cell surface, it is intractable to apply the Ising chain framework used to study cooperativity in [98].

We postulate that by imposing the ‘receptor ellipse’ to be circular, the cell can overcome the bias caused by its elliptical shape, which is particularly useful when the gradient is shallow. It can also maximize the information from each measurement by maximizing σ, or the radius of the ‘receptor circle’. This is a general result that is independent of our choice of the prior distribution. The case $\sigma_1 \neq \sigma_2$ is beyond the scope of this paper, but it offers the enticing prospect that the cell might adjust its shape (whilst leaving the receptor distribution uniform) to adapt itself to exploit prevailing gradient conditions optimally.

Chapter 5

Axon Guidance Studies Using a Microfluidics-Based Chemotropic Gradient Generator

Apart from formatting, this chapter is identical to Z. Pujic, H. Nguyen, N. Glass, J. Cooper-White, G.J. Goodhill, ”Axon guidance studies using a microfluidics-based chemotropic gradient generator,” in *Chemotaxis: Methods and Protocols (Methods in Molecular Biology)* (T. Jin and D. Hereld, ed.), Springer.

Abstract

Microfluidics can be used to generate flow-driven gradients of chemotropic guidance cues with precisely controlled steepnesses for indefinite lengths of time. Neuronal cells grown in the presence of these gradients can be studied for their response to the effects exerted by the cues. Here we describe a polydimethylsiloxane (PDMS) microfluidics chamber capable of producing linear gradients of soluble factors, stable for at least 18 hours, suitable for axon guidance studies. Using this device we demonstrate turning of superior cervical ganglion axons by gradients of nerve growth factor (NGF). The chamber produces robust gradients, is inexpensive to mass produce, can be mounted on a tissue culture dish or glass coverslip for long term timelapse microscopy imaging, and is suitable for immunostaining.

5.1 Introduction

For the brain to develop correctly it must be wired up correctly. To achieve this, growing axons must navigate reliably to their targets and make synaptic connections. Understanding how this navigation occurs is important since axon miswiring may underlie many mental disorders [8], and it is also critical for axons to be able to reform appropriate connections after injury. Due to the enormous complexity of the developing brain, it is often desirable to study these mechanisms *in vitro* since it is possible to exclude confounding factors. An important cellular process often required to accomplish correct guidance is the detection, by the growth cones at the tips of developing axons, of gradients of diffusible chemotropic cues within the developing tissues. The *in vitro* study of axon guidance by diffusible gradient cues ideally requires the generation of temporally and spatially stable gradients with precisely controllable characteristics, that can be applied to a large number of individual axons, and allow timelapse imaging. However few assays used for axon guidance studies currently achieve these goals. Collagen gel explant coculture assays [28] produce gradients which are poorly characterized and decay with time, while more sophisticated efforts to produce gradients with known steepnesses in collagen gels [166] are expensive to set up and limited to shallow gradients. The widely used "growth cone turning" or "pipette" assay [78, 240] has a low throughput, limited gradient stability, and little control over gradient steepness. The Dunn chamber can be effective for axon guidance studies, but as a passive device suffers from transients and gradient decay [241] . Many of these limitations can be overcome by using microfluidic technologies [141, 187]. Gradients of diffusible factors can be generated dynamically and therefore sustained at a particular steepness and concentration regime almost indefinitely. The number of isolated cells exposed to the gradient is generally greater than that for other assays, and the gradient can be defined with greater precision. Recent advances in microfluidics chamber design have employed innovative approaches which demonstrate that the approach is both powerful and versatile. For instance, microfluidically generated gradients of diffusible Slit-1 or Netrin-1 were able to elicit turning in hippocampal or dorsal root ganglion neurons [242]. Flow-based approaches can cause shear stresses which are damaging for growth cones, which are less robust than cell bodies. Various methods have been used to minimise this problem, such as culturing cells in a 3D hydrogel [242], using micro-well structures [203], or using a permeable membrane separated the fluid-flow driven gradient from the cells [243]. Here we describe a simple and easy to produce flow-based microfluidics chamber which can generate stable linear gradients despite using a flow rate low enough to be suitable for axon guidance studies.

5.2 Materials

To minimize the blockage of PDMS chambers by dust and other particulates, prepare all materials and solutions in a clean, dust-free environment. Where possible, work in laminar flow hoods to ensure that a minimal amount of dust and particulates are present. Use ultrapure water (deionized to attain 18 MΩ cm at 25 C) and filter all aqueous solutions with 0.2 μm filters.

5.2.1 Microfluidics

1. AutoCad software (Autodesk, Australia).

2. Photoplate (Konica, Minolta, New South Wales, Australia)

3. Silicon wafers (M.M.R.C. Pty Ltd, Malvern, Vic, Australia).

4. Photolithography: A clean room with a spin coater, level hotplates, mask writer or photoplotter, mask aligner (EVG, St. Florian, Austria) or UV flood source and a fume hood.

5. Photolithography chemicals: Ti Prime (MicroChemicals, Ulm, Germany), SU-8 2050 and SU-8 2100 (MicroChem, Westbrough, MA), Propylene glycol monomethyl ether acetate (PGMEA; Sigma-Aldrich, Australia) and Trichloro(1H,1H,2H,2H-perfluorooctyl)silane (Sigma-Aldrich) (see Note 1).

6. Chamber testing: Epifluorescence microscope or confocal microscope and 10 – 63X objectives (see Note 2). 7. Optical profiler (Wyko NT1100,Veeco, Plainview, NY).

8. PDMS mixture: Combine polydimethylsiloxane (PDMS) base elastomer (Sylgard 184, Dow Corning, Midland, MI) and silicon elastomer curing agent in a 10:1 (m/m) ratio in a 50 mL plastic tube. Mix for one hour either with a wooden tongue depressor or a rotary mixer.

9. Fluorescent dextran: Aqueous 10 mg/mL of 40 kDa dextran conjugated to tetramethylrhodamine (Life Technologies, Australia). Store 10 μL aliquots at -80 C (see Note 2).

10. Tubing: Polyethylene tubing I.D. 0.58 mm, O.D. 0.965 mm (Intramedic Clay Adams Brand, Becton Dickinson Co.). Cut to length as required. Store in 70% ethanol. Air dry in laminar flow hood and rinse with filtered PBS prior to use.

11. Metal connectors: These can be made by cutting the metal needle from a 23 gauge syringe and smoothing down any rough metal burrs on a wetstone.

12. Syringe connectors: 23 Gauge syringes (Terumo Medical Corp., NSW Australia) with the bevelled-tip cut off with a pair of metal snips. The rough edges are smoothened on a wetstone.

13. Syringes: 100, 250 or 500 μL glass syringes (SGE Analytical Science, NSW Australia) or 1 mL plastic syringes (Terumo Medical Corp.).

14. Microfluidics pump (e.g., Harvard Apparatus Ultra, SGE Analytical Science).

15. 0.75 mm corer (Harris Uni-Core, Ted Pella, CA, USA).

16. Plasma cleaner (e.g., PDC-002, Harrick Plasma, NY, USA).

17. (3-Aminopropyl)triethoxysilane (APTES; Sigma-Aldrich).

5.2.2 Tissue Culture

1. Laminar flow hood and tissue culture incubator with 5% CO2 at 37 C.

2. Leibovitz's L-15 medium: Add 5 mL of 45% glucose to 500 mL L-15 (Life Technologies). Store at 4 C.

3. Petri dishes: 35 mm wide, tissue-culture treated Petri dishes (Sigma-Aldrich).

4. Trypsin solution: Add 0.5 mL 2.5% trypsin to 2.5 mL calcium- and magnesium-free Hanks balanced salt solution. Prepare immediately before use.

5. Superior cervical ganglion (SCG) Growth Medium (SGM): 1X OptiMem-1 (Life Technologies) containing 1X penicillin/streptomycin, 10 μg/mL mouse laminin, 4% (v/v) fetal calf serum, 2% B-27 supplement (Life Technologies) (see Note 3).

6. Fixative: 4% paraformaldehyde in 1X phosphate buffered saline (PBS) (see Note 4).

7. H Solution: 6 nM NGF in SGM, equivalent to 20 × Kd (see Note 5).

8. Blocking solution: 4% normal goat serum in PBS.

9. Primary antibody: 1:1000 mouse anti-neuron specific β-tubulin class III antibody (BD Biosciences, Australia) in blocking solution. Add Triton X-100 to 0.05%.

10. Secondary antibody: 1:1000 goat anti-mouse Alexa 488 conjugated IgG (BD Biosciences, Australia) in blocking solution.

5.3 Methods

5.3.1 Shear Stress Determination

An important consideration when designing any microfluidics chamber with liquid flow is the potential for significant shear stress on the cells in the growing chamber. Various methods have been used to minimise this problem, such as culturing cells in a 3D hydrogel [242], using micro-well structures [203], or using a permeable membrane separating the fluid-flow driven gradient from the cells [243]. Using the chamber design in Fig 5.1A, we found no correlation between the final direction of axons and the fluid flow direction (i.e., no bias in neurite growth) due to liquid flow rates up to 200 μL/hr (data not shown). Assuming the Poiseuille model [244], the shear stress τ is calculated as follows:

$$\tau = -12\frac{\mu Q}{wh^2} \quad w \gg h$$

where Q is the flow rate (m3 s-1), μ is the fluid viscosity (Pa.s) and h (m) and w (m) are the channel height and width, respectively. According to this equation, a flow rate of 200 μL/hr caused shear of 1.7 N/m^{-2}. Since shear is not dependent on position within the growth chamber, and since the cells are all in contact with the growth chamber floor, the shear is uniform across all cells. Little is currently known about how much shear stress can be tolerated by neurons of different type or on different substrates. Morel *et al.* [243] found that at 5×10^{-2} N/m^2, the growth cones of rat DRG neurons displayed damage, but that at 5×10^{-4} Nm^{-2}, damage due to the shear stress was undetectable. Wang *et al.* [203] found that at 0.72 × 10^{-2} N^{-2}, Xenopus spinal neurons undergo collapse, but that at 4.5 × 10-4 N^{-2}, they did not. Consequently, the shear stress in our device at 200 μL/hr falls well below that of the detrimental value of 5 × 10^{-2} N/m2 used by Morel *et al.*, and is only about 2-fold above that found to be damaging for Xenopus spinal neurons by Wang *et al.* This suggests that the shear stress in our device is in a domain which, at least for rat SCG cells grown on plastic, is still conducive to growth. However, we note that the no-slip boundary condition for viscous fluid flow states that the velocity profile in a rectangular channel is parabolic [245], implying that the shear stress in the thin layer in which axons are growing may be significantly less than the value calculated above.

5.3.2 Microfluidics Chambers

5.3.2.1 Microfluidics Chamber Design

Draft the chamber design using AutoCad software and plot it onto the photoplate. Fig 5.1A illustrates the design used for the photomask for the first layer of lithography. In order to reduce the shear stress on neurons growing in the growth chamber, the design shown in Fig 5.1A is two-layered. The first layer consists of the entire pattern shown in Fig 5.1A with a height of 50 μm. The second layer is 100 μm thick and deposited over only the growing region. This means that although the fluid mixing occurs in channel heights of 50 μm, the cells are growing in a region with a 150 μm height. Since shear goes as 1/h2, the reduction in shear stress to the cells is considerable. Therefore, a relatively fast flow rate in the mixing channels using only a small expenditure of fluid can be used to establish the gradient quickly.

5.3.2.2 Microfluidics Chamber Fabrication

Fabricate chamber molds using standard SU-8 multilayer photolithography techniques as follows:

1. Clean silicon wafers using a plasma cleaner with a power of 200 W at a pressure of 200 mTorr for 5 minutes.

2. Immediately after cleaning the wafers, coat them with Ti Prime by spin-coating at 3000 rpm for 30 s, followed by a two minute bake at 110oC. Then allow the wafers to cool to room temperature.

3. Next, deposit a layer of SU-8 2050 on the wafers by spin-coating, according to the manufacturer's recommendations. To achieve an approximately 50 μm thickness, spin the SU-8 at 500 rpm followed by 1500 rpm for 10 and 30 seconds, respectively.

4. The wafers are then soft baked at 65oC and 95oC for 3 minutes and 9 minutes, respectively.

5. After allowing the wafers to cool to room temperature, expose them in the mask aligner to a dose of 175 mJ/cm2. Fig 5.1A shows the pattern that was used.

6. Perform a post-exposure bake at 65oC and 95oC for 2 minutes and 7 minutes, respectively, and then allow the wafers to cool to room temperature.

7. Apply a second layer of photoresist, this time SU-8 2100, by spin-coating at 500 rpm followed by 3000 rpm for 10 and 30 seconds, respectively. This allows for an approximate additional height of 100 μm.

8. The wafers are then soft baked at 65oC and 95oC for 5 minutes and 30 minutes, respectively.

9. Next align and expose a second mask using the mask aligner at a dose of 250 mJ/cm2. The second mask is designed to increase the height of the growth chamber and exit hole regions of the devices.

10. When the wafers return to room temperature, develop them in PEGMA for approximately 15 minutes.

11. Verify the height of the mold using the optical profiler. The lowest and highest features should measure around 50 μm and 150 μm, respectively.

12. Next silanize the molds to prevent PDMS adhesion. Clean the freshly processed masters using an oxygen plasma cleaner and then place them in a vacuum desiccator with several drops of Trichloro(1H,1H,2H,2H-perfluorooctyl)silane for approximately 20 minutes.

13. Pour enough PDMS mixture onto the silicon master to cover it to a depth of about 4 mm.

14. Place the mold with PDMS into a vacuum chamber and apply vacuum for 2 hours to degas the PDMS (see Note 6). During degassing, minute bubbles will form in the low air pressure and rise to the top of the liquid PDMS. After 2-3 hours, the PDMS will appear completely transparent.

15. Bake (cure) the mold for at least 2 hours at 80 C. Baking at higher temperatures for slightly shorter times will also lead to curing.

16. Using a scalpel, carefully cut around the chamber, taking care to avoid damaging the lithographed pattern on the silicon wafer. Gently pull the chamber out of the mold.

17. Cover the channel side of the chamber with Scotch magic tape to protect the channels from airborne dust which can lead to clogging during later stages.

18. Using a 0.75 mm corer, core holes into the PDMS where fluid or cells can be introduced. The corer should have an external diameter slightly smaller than that of the metal connecting tubes. Make sure the PDMS “noodle” is pushed out of the holes and the corer goes all the way through the PDMS.

19. To bond the PDMS chamber to a plastic tissue-culture petri dish, plasma treat the petri dish (using 100 W at a pressure of 380 mTorr for 30 seconds) and then pour enough APTES solution (5% APTES in 70% ethanol) into the dish to cover the bottom surface and leave for 5 minutes. Meanwhile, plasma treat the PDMS chamber with high power for 40 seconds. Make sure the PDMS chamber is placed into the plasma cleaner so the channels side is face-up, otherwise the plasma will not properly treat the surface. Discard the APTES solution from the petri dish, wash thoroughly with water, and allow it to air dry or blow dry. Press the PDMS chamber onto the APTES-treated petri dish. Make sure to press the channel-side surface of the PDMS onto the dish. If bonding of PDMS chambers onto glass is required, plasma treat the glass and the chamber at the same time and gently press the chamber on glass (see Note 7).

20. Bake the dish for 30 minutes at 65 C. Although the bond forms within a few seconds, baking will increase bond strength. After baking, the chamber is ready to be used for tissue culture, otherwise chambers can be prepared ahead of time and stored at room temperature (see Note 8).

21. Fill the plate with filtered PBS and penicillin/streptomycin and degas in the vacuum chamber for 5 minutes. Take out the chambers at least 15 minutes before injecting cells into them to allow the solution to fill up all the channels to avoid air bubbles.

5.3.3 Tissue Dissociation

1. Cut out the superior cervical ganglia (SCG) from P0-P3 rat pups into about 2 mL Leibovitz medium in a Petri dish kept on ice. Leave in trypsin for 30 minutes at 37 C in a 15 mL tube. Use a sterilised flame polished glass Pasteur pipette to gently triturate the cells by aspirating up and down slowly (see Note 9).

2. Stop the trypsin by filling the tube with Leibovitz medium to 15 mL. Centrifuge at 190 rcf for 5 min at 4 C. Discard the supernatant carefully and then repeat with 15 mL Leibovitz, then 15 mL OptiMem and then with 0.5 mL filtered SGM containing 0.3 nM NGF. Suck out most of the solution to leave 50 μL of solution per SCG. Very gently resuspend the cells. Using the microfluidics pump or pumping by hand with a short length of polyethylene tubing connected to a metal connector, aspirate the solution at 1 μL/s and then inject into a test chamber through the outlet with the chambers fully immersed in PBS/PS. Make sure there is no air bubble in the injected solution or in the chambers. Adjust the cell density so that $20 - 100$ cells enter the growth chamber. Very low density often leads to poor growth and very high density makes imaging difficult.

5.3.4 Growth in the Gradient

1. Leave the cells in the incubator for at least 1 hour to allow cells to adhere to the substrate before setting up the flow.

2. Cut two lengths of polyethylene tubing approximately 60 cm (see Note 10). Connect a metal connector to one end of each tube (Fig 5.1B). Connect the other end of each tube to a syringe connector and connect, via a Luer lock, to a 250, 500 or 1000 μL glass syringe or a plastic 1 mL syringe (the size of the syringe limits the duration of the experiment). Insert the syringes into the microfluidics pump. The syringes contain H solution (SGM with a high concentration of guidance cue (in our case NGF), equivalent to 20 × Kd) and L solution (SGM

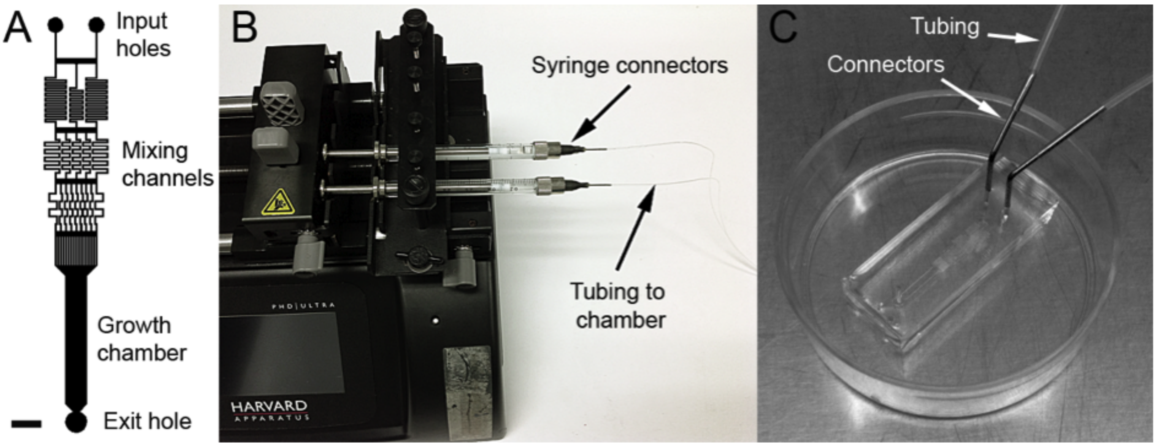

FIGURE 5.1: A schematic of the microfluidics chamber channels. A. The two input holes separately receive SGM containing NGF (H solution) or SGM only (L solution). The media are combined in the mixing channels and enter the growth chamber and eventually leave through the exit hole. The heights of the growth chamber and exit hole are 150 μm, while all other regions of the device are 50 μm. Scale bar = 1 mm. B. Two syringes mounted on a Harvard Apparatus infusion pump via syringe connectors. The polyethylene tubing enters the PDMS chamber (see panel C). C. A completed PDMS chamber bonded to a 35 mm tissue culture grade Petri dish. Metal connector tubes are used to connect the polyethylene tubing to the chamber.

with no guidance cue). Make sure there are no air bubbles in the tubing and that there is no air in the syringes. To generate a linear gradient, the flow rates of both syringes have to be the same (5 μL/hr each). To increase the throughput, four chambers can be run in parallel, with 8 syringes on 2 PhD Harvard pumps.

3. Pump out a small amount of solution then quickly put the metal pins of the H and L tubes into the appropriate inlets (Fig 5.1C; see Note 11). Turn on the flow to 5 μL/hr. Gradients should establish within 5 minutes.

4. Place the chambers into a tissue culture incubator (with the pump outside). After 2-4 hours, neurites will start to grow from the cell bodies. At this point, the cells may be used for live imaging by moving the chambers and pump(s) to an incubated inverted microscope. The tubing can be attached to the incubator door higher than the plate so that air bubbles will rise and not enter the chambers. Otherwise incubate the chambers overnight. Make sure there is enough solution in the syringes for the desired duration of the experiment.

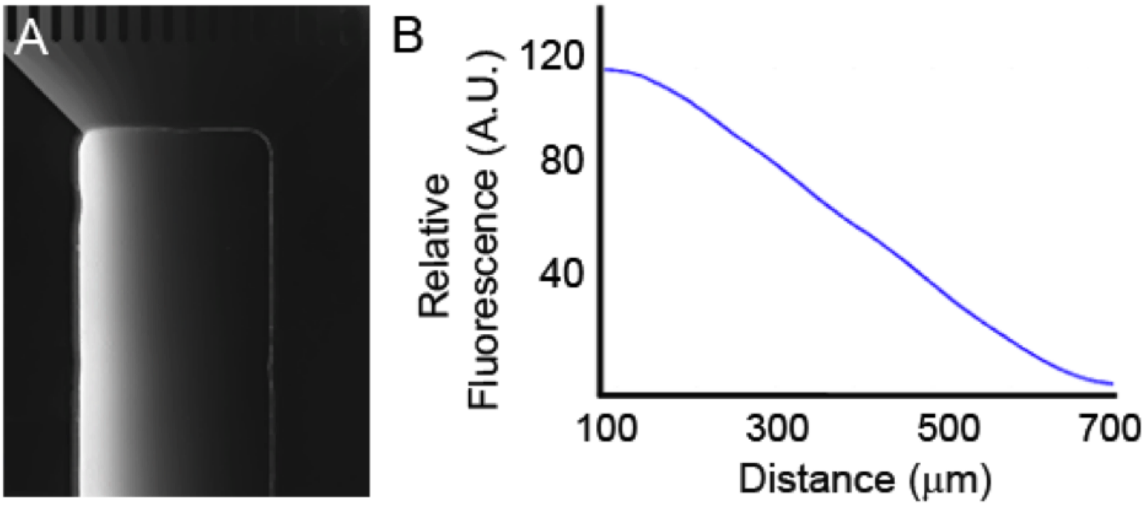

FIGURE 5.2: A. A gradient of 40 kDa dextran-tetramethylrhodamine in the growth chamber of the PDMS chamber shown in Fig. 5.2B. B. The relative fluorescence of 40 kDa dextran-tetramethylrhodamine in a transverse section through the gradient in Fig. 5.2A. (A.U. = arbitrary units).

5.3.5 Quantification of Guidance

1. The chambers can be used for *in vitro* imaging of growth cone guidance using time-lapse microscopy. The chambers should be housed in an inverted microscope with environmental control including temperature (37 C) and a 5% CO2 atmosphere. Images can be obtained using phase contrast microscopy at 1 minute intervals for up to 4 hours. The degree of guidance can be estimated for each growth cone from the time-lapse data using the definition of the turning angle shown in Fig 5.3B [241]; however, other definitions of turning can also be used [203, 246]. 2. If, following growth of neurites in the growing chamber, the axons need to be immunostained, then gently remove the tubing from the microfluidics chamber and examine the growing chamber. Neurites should be visible under phase contrast microscopy (see Note 12 and 5.3A). Fill a 1 mL plastic syringe with fixative and, with a short length of polyethylene tubing (and using the appropriate connectors) pump through the fixative into the exit hole at 1 μL/s for 60 seconds. Replace the fixative in the syringe with PBS and pump through at the same flow rate for 5 min to remove all fixative. Pump through blocking solution and then primary antibody at the same flow rate for 60 seconds. Leave the primary antibody solution in for 15 min without flow. Pump through the appropriate fluorophore labelled secondary antibody at the same flow rate for 60 seconds and leave without flow for 15 min. Finally, wash with PBS for 5 min (see Notes 13 and 14).

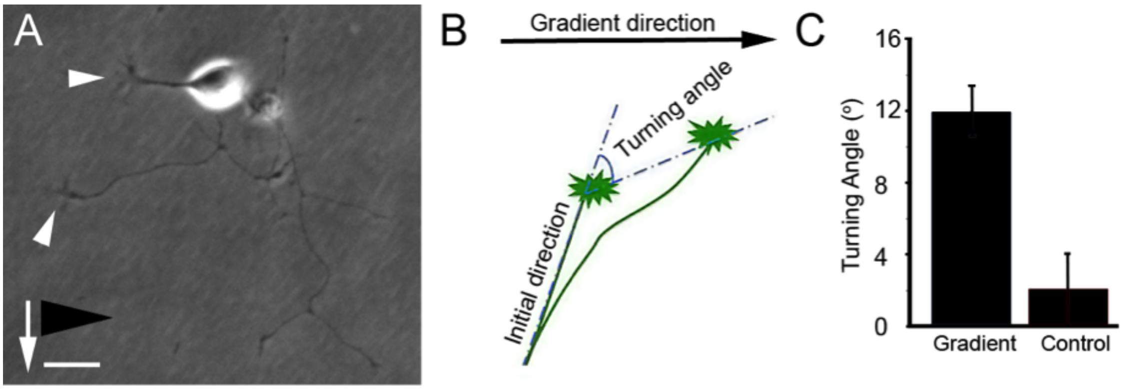

FIGURE 5.3: A. Phase contrast image, obtained with a 20X objective, of an SCG neuron grown in a microfluidics chamber with an NGF gradient (gradient direction is shown by the black triangle). The white arrow indicates direction of fluid flow. White arrowheads indicate growth cones with filopodia. Scale bar = 10 μm. B. Definition of initial angle and turning angle in short-term turning assay. The reference axis is perpendicular to the direction of flow, which is the gradient direction. The initial direction is defined as the tangential direction of the 15 μm neurite segment. The initial angle is defined as the angle between initial direction and the reference axis. The turning angle is defined as the angle between the line connecting the growth cone before and after the assay and the initial direction. C. Turning angles of axons grown either in a gradient of NGF (n = 190 axons) compared to those grown in an NGF plateau control (n = 110 axons) using a flow rate of 10 μL/hr. Axons grown in the gradient display a positive turning response of 12 ± 1.4 compared to 2.1 ± 2.0 (mean ± S.E.M.) for those grown in a plateau of NGF ($p = 0.033$, t-test).

3. Photograph neurites at 20X using fluorescence microscopy for the appropriate fluorophore.

5.4 Notes

1. Chamber design: A comprehensive description of the concepts used in the design of our chamber can be found in Campbell *et al.* [247]. The dimensions of the design were modified to suit the diffusion constant of nerve growth factor.

2. To test whether the chamber is capable of generating a gradient, a fluorescently labeled dextran, of a molecular weight roughly equivalent to the guidance cue being studied, can be used to visualize the gradient. 40 kDa-dextran fluorescently labelled with tetramethylrhodamine has a molecular weight similiar to that of nerve growth factor. To visualize the gradient, set up a gradient as in section 3.4.2, however exclude the guidance cue and instead, include the fluorophore in the H solution. L solution should contain no fluorophore. The exact concentration of the fluorophore in the H solution is not important as long as it is high enough to provide an

image of the gradient using a relatively short exposure (e.g., 1 second) (5.2A and 5.2B). Time lapse-imaging of the chamber can be used to assess the stability of the gradient.

3. This is also suitable for the growth of dorsal root ganglion neurons from newborn rat pups up to about postnatal day 7 of age.

4. 4% paraformaldehyde in PBS can be stored at -20 C for several months and should be thawed to room temperature before use. It produces sufficient fixation for the visualization of axons, however we find it unsuitable for the fixation of finer cellular detail such as filopodia.

5. The dissociation constant (Kd) of NGF for its high affinity receptor, TrkA, is about 0.3 nM [95].

6. When PDMS is mixed or poured, tiny bubbles will be generated which, if not removed, will become incorporated into the microfluidics chamber during curing.

7. If PDMS chambers do not adhere to glass or plastic substrates, the plasma oxidation conditions should be optimized. Determine optimal oxidation time, ionization strength and O2 pressure within the plasma cleaner. For our Harrick Expanded Plasma Cleaner, typical values are 380-410 mTorr O2 pressure, 30 W power and 30 – 50 s ionization time.

8. Contamination by bacterial and fungal cells may be reduced by spraying the chambers with 70% ethanol following by irradiation with short-wavelength UV for several hours. Once dried, the chambers may be used for tissue culture.

9. Poor cell growth can also be due to poor trituration. Optimise the trypsin concentration and incubation time. Optimise the size of the flame-polished pipette bore. Holes which are too large will result in poor dissociation. Holes which are too small will result in high cell death. Ganglia should dissociate into cells within 2 minutes of trituration.

10. The length of both tubes has to be enough so that the microfluidics chamber can be placed in a tissue culture incubator with the microfluidics pump outside the incubator.

11. A major problem which will be encountered when using microfluidics is the accidental introduction of air bubbles into the chamber. This can occur mostly as a result of poor connections where the metal connector tubes are inserted into the chambers. The metal connectors can be sealed by making a small amount of PDMS with curing agent and spreading about 10

μL around the insertion site followed by curing at 65C. Then fill the plate with filtered PBS to immerse both the chambers and connector pins in solution and degas. Use the tubing to suck solution through the connector pin to fill up all the channels and pins with PBS. However we find that the best solution is to ensure that coring achieves clean defect-free holes which are less likely to leak and inject into the chambers while they are immersed in solution.

12. If neuronal cell growth is poor, it may be necessary to perform PDMS extraction prior to bonding to the substrate. This is done in order to remove unpolymerized PDMS monomers from the PDMS chamber which may cause cell toxicity. Numerous PDMS extraction techniques exist. We have found the following to improve neuronal cell growth: Following removal of the PDMS from the mold, immerse chambers for 200 mL for 1 hour into each of the following; 100% pentane, 100% acetone and then 100% ethanol. PDMS will swell significantly while in the pentane and acetone, and care should be taken to ensure the liquid volume is significantly larger than the PDMS volume. Do not delay in transferring chambers from one solution to the next otherwise cracking of the PDMS will occur. After PDMS have soaked in the ethanol, bake at 65 C for 2 hours and proceed with bonding to the substrate. Discard the used solutions according to institutional guidelines.

13. Image quality of the immunostained cells will be better with a glass substrate.

14. We find that a high solution (H) of 20 - 40 Kd and a low solution (L) of 0 Kd elicited the strongest turning responses in SCG axons whereas a very high solution of H = 200 Kd abolishes the turning (5.3C shows turning of growth cones in a gradient using nerve growth factor with L = 0 nM, H = 20 Kd nM). If no turning is observed, these parameters should be optimized.

Chapter 6

A mathematical model explains saturating axon guidance responses to molecular gradients

Apart from formatting and the abridged Methods section, this chapter is identical to H. Nguyen, P. Dayan, Z. Pujic, J. Cooper-White, G.J. Goodhill, “A mathematical model explains saturating axon guidance responses to molecular gradients” resubmitted to eLife.

Abstract

Correct wiring is crucial for the proper functioning of the nervous system. Molecular gradients provide critical signals to guide growth cones, which are the motile tips of developing axons, to their targets. However *in vitro* growth cones trace highly stochastic trajectories, and exactly how molecular gradients bias their movement is unclear. Here we introduce a mathematical model based on persistence, bias and noise to describe this behaviour, constrained directly by measurements of the detailed statistics of growth cone movements in both attractive and repulsive gradients in a microfluidic device. This model provides a mathematical explanation for why average axon turning angles in gradients *in vitro* saturate very rapidly with time at relatively small values. This work introduces the most accurate predictive model of growth

cone trajectories to date, and deepens our understanding of axon guidance events both *in vitro* and *in vivo*.

6.1 Introduction

For the brain to function correctly, it must be wired correctly. Indeed, many neurodevelopmental disorders are likely the result of wiring defects [10, 248–250]. Axon guidance, where axons grow and navigate to their targets, occurs primarily via the sensing of molecular cues in the environment. A critical mechanism by which such cues act is believed to be concentration gradients, causing axons to be attracted or repelled in particular directions [5, 30]. However, despite major advances in understanding which molecules are involved in this process [1–3, 251], an accurate quantitative model describing how axon trajectories are influenced by such guidance cues is still lacking.

In vivo, axon trajectories may potentially be influenced by many cues. *In vitro* assays allow individual influences, such as that from the concentration gradient of a single guidance factor, to be isolated and quantified. A substantial mystery posed by *in vitro* axonal chemotaxis assays is the relatively weak turning produced, even over long periods of time. The naive prediction that axons would promptly turn until they become fully aligned with the gradient turns out not to be true. In an early study of chemotactic responses of chick sensory neurons to a gradient of nerve growth factor in a diffusion chamber, only 60% of nerve tips were preferentially directed towards the gradient direction after 46 hours of growth [46]. The growth cone turning assay over 1-2 h produces average turning angles typically ranging from 10-25°, with high variability [80, 156, 157, 252, 253]. A similarly weak response is observed in the Dunn chamber [241, 254–257]. More recent studies using microfluidic technologies over timescales ranging from hours to days have also elicited average axon turning angles only up to 10-15° [203, 243, 258, 259]. Why average turning angles are so small, and what this means for axon guidance *in vivo*, are unclear.

One of the key properties of *in vitro* axon growth that might explain this mystery is that it is often very straight [121, 122]. Axons are under mechanical tension from the pull of the growth cone [260, 261], and this tension stimulates the elongation of the axon by stretching [262, 263]. Traction forces generated in the growth cone arise from the coupling of the continuous retrograde flow of actin to the substrate through adhesion receptors [264–266]. For reasons which are not clear, axons tend not to bend and follow the highly random movements of their growth cones. Rather, they usually form a straight line between their tip and a location where they are firmly attached to the substrate (i.e. a focal adhesion [267]). We call such locations anchor points; they can be at the soma, at a branch point, or at some other seemingly sporadic location along the axon. Although it is not clear how this tension leads to elongation, the growth cone advances largely in the stretch direction along the axon, resulting in relatively straight paths.

To determine quantitatively what effect this might have on axonal trajectories requires mathematical modelling. Growth cone movements were first analyzed in detail in [121, 122]. Subsequently, various phenomenological models have been built that differ as to how they treat stochasticity, and mechanisms for directional preference, namely turning or growth rate modulation. One set attempted to fit the dynamics of growth cone movement to a random walk with drift [123–125, 129]. Li *et al.* simulated trajectories by assuming the turning angle of the growth cone is in proportion to the angle between the neurite and the resultant filopodial tension [131]. In [126], the axon growth angle depends on the tendency to turn towards the gradient angle and noise. The noise term is small (2-5°), leading to straight paths that resemble axon growth in the tadpole spinal cord. Another set of models has concentrated on how asymmetric receptor binding across the growth cone might be used as the basis of a turning signal [133, 134, 139], but without considering the consequence for whole trajectories. A third group of models considers the possibility that the velocity of the growth cone is influenced by an attractive gradient from the target cells, and chemoattractants and chemorepellants released from other growth cones and itself [136, 137]. However none of these models has been closely compared with the details of experimentally measured trajectories in gradients, and parameters such as variability in step sizes, the distribution of instantaneous turning angles, and straightness of real paths, have not been addressed. Thus the question of whether there is a model that can adequately capture all these characteristics of real trajectories remains open. Without such a model, it is difficult to determine if trajectories observed *in vivo* are in fact consistent with gradient guidance.

Here we present a new computational model for axonal trajectories based on the combined influence of anchor points, a tendency to turn towards the gradient direction, and random noise. We found that the gradient had no effect on the step sizes, thus we only model the turning angles. Critically, the model predicts rapid near saturation of average turning angles with time. To test this model quantitatively we then introduce a new microfluidics assay for studying axonal response to gradients, and using timelapse imaging characterize the behavior of axons over several hours of growth in both attractive and repulsive gradients. We find that our model fits the behavior observed very closely. We then investigate by simulation the effect of increasing the number of anchor points, and find that this increases the average fidelity of turning but at the cost of higher variability. Together, this work both explains why turning response to gradient saturates so rapidly and reveals the quantitative principles that are required to reproduce accurately *in vitro* axonal trajectories in response to chemotactic gradients. The model identifies straightness as a limiting factor on how much axons can turn and suggests that the frequency of anchor points plays a key role in the axonal turning response to a gradient.

6.2 Materials and Methods

Microfluidics chamber fabrication, primary superior cervical ganglion (SCG) cell culture and gradient measurement

See Chapter 5.

We added another condition: To generate a repulsive gradient, KT5720 (Alexis Biochemicals), a specific inhibitor of protein kinase A (PKA), was added into both the high and low solutions at a concentration of 70 nM.

Tracking growth cone trajectories

After the onset of the gradient, the axons were imaged every 5 min for 6 hours using Zeiss Zen software. After data acquisition, axons of 30 μm length, growing in all directions, that did not branch or retract in at least 80 minutes, were chosen for measurements. All axons were tracked manually using customized MATLAB software (The MathWorks) for as long as possible until they branched or retracted. A 5 min time interval was chosen because, for smaller intervals, variability in identifying the centre of the growth cone was larger than the net movement between frames. The point where the axon attaches to the cell body or the main branch was considered the anchor point.

The straightness index

The straightness index S is the inverse of tortuosity, and compares the overall net displacement G of a path with the total path length T [268]. Consider a walk that starts at location (x_0, y_0), and after n steps of lengths l_j $(j = 1...n)$ finishes at (x_n, y_n). The straightness index is given by:

$$S = \frac{G}{T} = \frac{\sqrt{(x_n - x_0)^2 + (y_n - y_0)^2}}{\sum_{j=1}^{n} l_j}$$

This index is between 0 and 1, where 1 corresponds to movement in a straight line and 0 corresponds to a walk that returns to the origin. The closer this index is to 1, the straighter the trajectory is. Obviously S depends on the time interval used for tracing, but can be used to compare conditions which all have the same time interval.

Modelling growth cone trajectories

All parameters of the model are summarized in Table 6.1. We consider a model which is a discretized random walk in which we separate the length and directions of the steps (Fig 6.1A). We discretized the axons at a timestep of 5 minutes, and, based on hypotheses we test later, only explicitly modelled the turning angles of the steps or 'bearing changes'. $\Delta\theta(t)$, the 'bearing change' at time t depends on the current bearing of the growth cone $\theta(t)$, the angle $\phi(t)$ of the vector connecting the growth cone to its anchor point, the gradient direction Ψ and the noise ξ according to Equation (6.1):

$$\Delta\theta(t) = a\angle(\phi(t), \theta(t)) + b\angle(\Psi, \theta(t)) + \xi,$$

where two parameters a and b scale the contributions of the first term representing persistence and the second term representing the bias due to the gradient. The symbol $\angle(x, y)$ denotes the

Symbol	Meaning
θ	GC's current bearing
ϕ	GC's overall angle
Ψ	Gradient direction
$\Delta\theta$	Bearing change
ψ_{turn}	Turning angle after 80 minutes
a	Persistence strength
b	Bias strength
ξ	Noise in bearing change
σ	Standard deviation of ξ
s	Step size every 5 minutes
L	Distance from origin to GC
S	Straightness index
r	Anchoring rate

Table 6.1: Summary of model parameters (GC: growth cone).

angle difference $x-y$ constrained to take values from $-\pi$ to π. It is positive for an anticlockwise turn to get from y to x. As the bearing is biased by the gradient direction, the overall growth cone angle $\phi(t)$ will also be biased by the gradient, coupled through the above equation.

We first assume there is only one fixed anchor point where the axon initially grew out of the cell body or the main branch. We will later relax this assumption and allow the growth cone to put down new anchor points along its path. We denote the rate of anchor point deposition as r, which is the inverse of the average number of steps per new anchor point.

We first assume an initial direction of $\phi(0) = \theta(0) = \pi/2$, a gradient direction of $\Psi = 0$ and a fixed step size s every 5 minutes. In the idealized noiseless case ($\xi = 0$) as $t \to \infty$, the equation reaches a steady state when $\Delta\theta = 0$, i.e.:

$$\Delta\theta(t) = a(\phi(t) - \theta(t)) + b(0 - \theta(t)) = 0.$$

This gives:

$$\theta(t) = \frac{a}{a+b}\phi(t) = \alpha\phi(t)$$

with $\alpha = \frac{a}{a+b}$. Defining L to be the distance of the growth cone from its original position, and using the geometry in Fig 6.1.A, we have:

$$\begin{aligned}\tan(\phi(t+1)) &= \frac{L\sin\phi(t) + s\sin(\alpha\phi(t))}{L\cos\phi(t) + s\cos(\alpha\phi(t))}\\ &\approx \tan(\phi(t)) + \frac{s\sin(\alpha\phi(t))}{L\cos\phi(t)} - \frac{L\sin\phi(t)s\cos(\alpha\phi(t))}{L^2\cos^2\phi(t)}\end{aligned}$$

The approximation above is due to $s \ll L$ and $\phi(t) \to \Psi = 0$ as $t \to \infty$. Using the Taylor expansion $f(x_0 + \delta x) \approx f(x_0) + \delta x f'(x_0)$ and $d\tan^{-1}(x)/dx = 1/(x^2+1)$, we invert both sides of the above equation to obtain:

$$\begin{aligned}\phi(t+1) &\approx \tan^{-1}(\tan\phi(t) + \frac{s\sin(\alpha\phi(t))}{L\cos\phi(t)} - \frac{L\sin\phi(t)s\cos(\alpha\phi(t))}{L^2\cos^2\phi(t)})\\ &\approx \phi(t) + (\frac{s\sin(\alpha\phi(t))}{L\cos\phi(t)} - \frac{L\sin\phi(t)s\cos(\alpha\phi(t))}{L^2\cos^2\phi(t)})\cos^2\phi(t)\\ &\approx \phi(t) + s/L\,(\sin(\alpha\phi(t))\cos\phi(t) - \cos(\alpha\phi(t))\sin\phi(t))\\ &\approx \phi(t) + s\sin((\alpha-1)\phi(t))/L\end{aligned}$$

At $t \to \infty$, $\Delta\theta(t) \to 0$, meaning the growth direction stops changing, thus $\phi(t) \approx 0$ and $L \approx st$ due to geometry (even for the $a = 0$ case), so the above equation can be simplified as

$$\frac{d\phi(t)}{dt} \approx \frac{(\alpha-1)\phi(t)}{t}$$

$$\frac{d\phi(t)}{\phi(t)} \approx \frac{(\alpha-1)dt}{t}$$

$$\ln\phi(t) = (\alpha-1)\ln t + \text{const}$$

Therefore, the long-term turning behaviour of axons in the model is given by the power law $\phi(t) \propto t^{(\alpha-1)}$.

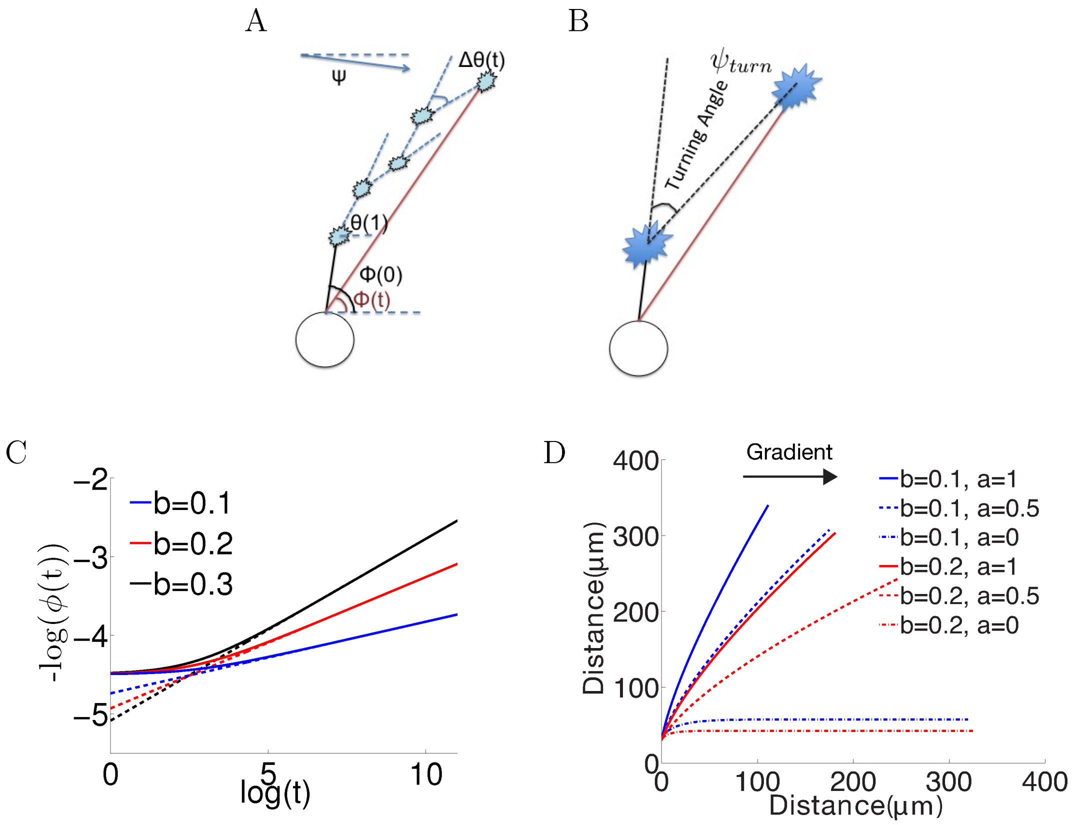

FIGURE 6.1: **Model set-up and the noiseless case.** A, The axon starts growing from the soma (black segment) at initiation angle $\phi(0)$. At each time point the bearing is $\theta(t)$, and the bearing change between t and $t+1$ is $\Delta\theta(t)$. $\phi(t)$ is the angle of the vector connecting the current position of the growth cone with the anchor point. Ψ is the fixed gradient direction. B. The turning angle ψ_{turn} at time t is the angle between the initial direction of growth, and the line joining the initial and current positions of the growth cone. C. Simulation of the growth cone angle using equation (6.1) in the noiseless case ($\xi = 0$) with the same $a = 1$ and different values of b. The dashed line is the power law $\phi(t) \propto t^{\frac{-b}{a+b}}$. In the long time limit, this law accurately describes the angle of the growth cone. D. Simulations of the trajectories for different combinations of a and b in the absence of noise. Larger b leads to stronger turning. When $a = 0$, the growth cone very rapidly aligns with the gradient. The persistence term ($a > 0$) leads to incomplete turning.

6.3 Results

A correlated walk model of growth cone trajectories

We modelled 3 basic influences on the direction of axon growth: a tendency to grow straight, the effect of a chemotactic gradient, if present, and random movement noise. In a fixed coordinate system with arbitrary zero angle direction, we define $\theta(t)$ as the bearing of the growth cone at time step t, $\phi(t)$ as the angle of the vector connecting the growth cone to its anchor point, and Ψ as the gradient direction (terminology is summarized in Table 6.1). We define 'bearing change' as $\Delta\theta(t)$, the change in $\theta(t)$ at time step t, distinct from 'turning angle' ψ_{turn}, the total change in θ from the initial direction of growth over long periods of time. For simulations we identify each timestep as 5 minutes of real time. The model (Fig 6.1) is then

$$\Delta\theta(t) = a\angle(\phi(t), \theta(t)) + b\angle(\Psi, \theta(t)) + \xi, \tag{6.1}$$

where a scales persistence to move in the same direction as the overall direction of the axon, b scales the bias due to the gradient, and ξ is random noise in the bearing changes. The symbol $\angle(x, y)$ denotes the signed angle between the unit vectors with angles x and y, and constrains the resultant angle to be between $-\pi$ and π. The step size is the distance moved after one time step, and will later be estimated empirically.

We consider first the noiseless case ($\xi = 0$) in long- and finite-time regimes, and then consider the effects of noise. Figure 6.1C shows the results of setting $\xi = 0$, with a fixed step size of $s = 3\mu$m, and simulating the model for long times with the same $a = 1$ and different values of b (0.1, 0.2 and 0.3). Turning angles rapidly saturate, which can be understood analytically (see Methods): in the $t \to \infty$ limit, the growth cone angle follows a power law with respect to time $\phi(t) \propto t^{(\alpha-1)}$ or $\log(\phi(t)) = \text{const} + (\alpha - 1)\log(t)$ (Fig 6.1C). This relationship generally holds for $t > \exp(4) \approx 4$ h, meaning that for long times, the rate of change of angle decreases and this rate is determined by the power law exponent $b/(a + b)$. Since comparison with empirical data (see later) shows that the biologically relevant regime is $b \ll a$, the exponent is generally small. Thus, while ultimately axons in the model do eventually align with the gradient, this process takes an exceedingly long time. This explains the slow and decreasing change in the turning angle over time in the noiseless case.

The finite t regime of this equation is difficult to solve analytically, since $\phi(t)$ depends on the entire history of growth cone movements. Simulations using different combinations of a and b are shown in Fig 6.1D. For the cases of $a \neq 0$, after 150 time steps (12.5 h of real time), the resultant turning angle was far from completely aligned with the gradient. Although the bias term bent the trajectory in the direction of the gradient, there was a straightening effect due to the persistence term, constantly pulling the growth cone towards the overall growth direction of the axon. As expected, the pull due to the gradient increased with larger b (Fig 6.1D). Thus, the persistence term prevented the axon from completely aligning with the gradient. Also

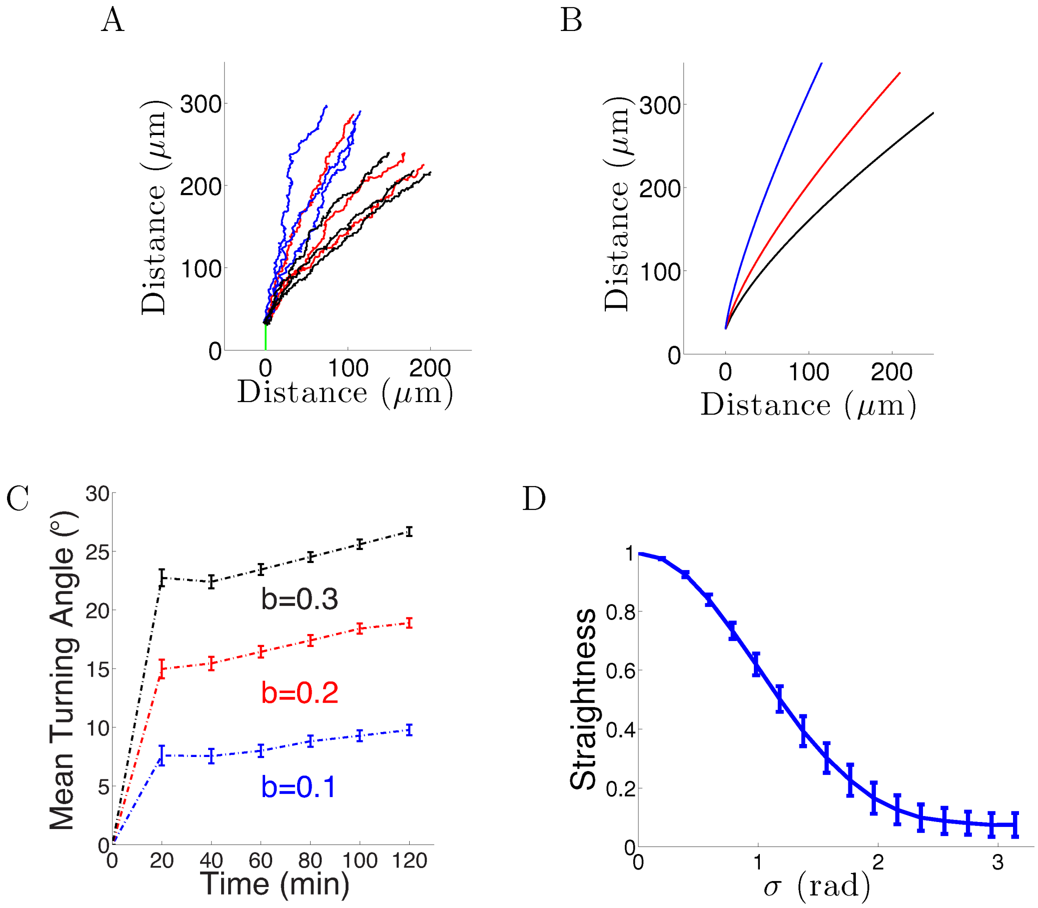

FIGURE 6.2: **Model results with noise.** A. Long term behaviour of growth cones: Simulation of 9 axons with fixed growth rate and noise in bearing changes ($\xi \propto \mathcal{N}(0, \pi/4)$ radians) starting at $\phi(0) = 90$ subject to the gradient direction $\Psi = 0$ with persistence $a = 1$ and bias $b = 0.1$ (blue), $b = 0.2$ (red), $b = 0.3$ (black) after 150 steps (12.5 hours of real time). B. The trajectories with the same parameters without noise. C. The turning angles over time (mean ± SEM) of 1000 axons for different values of b (0.1, 0.2, 0.3) and $a = 1$. D. Straightness (mean ± STD) decreases as the noise variance increases.

apparent is that without noise, the trajectories were all very straight (with straightness index (see Methods) greater than 0.98). Thus, the microscopic constraint imposed by the persistence term leads to the macroscopic phenomenon of incomplete turning.

When we introduced Gaussian noise into the bearing changes (in radians) ($\xi \sim \mathcal{N}(0, \sigma)$, $\sigma = \pi/4$) with the same parameters and initial conditions as above for 1000 axons, the behavior was qualitatively similar: after an initial period of relatively rapid turning, turning angles tended to an almost steady state which was not aligned with the gradient even after a long time. However the average final turning angle was even less than that of the noiseless case. This is because the noise created more random wandering of the growth cone, further reducing the directional effect of the gradient (Fig 6.2A-B). After 20-40 minutes, for $b = 0.1$, the turning angle distribution of the population was $7 \pm 25°$ (mean ± std). Assuming a normal distribution of turning angles, this means that many of the axons were no longer roughly perpendicular to the gradient, and thus only continued to turn extremely slowly. Therefore over time the influence of the gradient on the whole population of axons weakened. The persistence term also created a resistance against large turns due to the gradient. Increasing b/a increased the turning angle, but did not alter its rapid saturation with time (Fig 6.2C). Lastly, we examined the effect on the straightness by varying the standand deviation of the noise σ from 0 to π radians. As the steps became more noisy, the paths became less straight (Fig 6.2D).

In summary, the noiseless case generated very straight axons and growth cone angles that followed power laws with respect to time in the long time limit. Similarly, in the noisy case, the rate of change of the average turning angle was initially rapid and then slowed down even more rapidly with time. In both cases, the persistence term was a limiting factor on how much and how fast the axons could turn. Thus, this model captures, at least qualitatively, the behavior that axons turn only slightly in gradients, and even for long times do not generally become completely aligned with the gradient.

Stable gradient generation for guidance assays

Having established the basic behaviour of the model, we then asked whether it could reproduce in detail real axon trajectory statistics. We therefore analyzed the trajectories of superior cervical ganglion neurons in a new microfluidics device (Fig. 6.3A-C). This device generated linear gradients, by the mixing of high and low solutions of a chemotropic factor. The gradient was visualized using 40 kDa dextran-tetramethylrhodamine (Fig 6.3D), and gradients were stable for at least 20 hours (Fig 6.3E,F).

SCG neurons were guided in the microfluidic assay

We measured the response to nerve growth factor (NGF) gradients of axons from dissociated P1-P3 SCG neurons. We chose this model system because almost 100% of these neurons express the NGF receptor TrkA ([269, 270]).

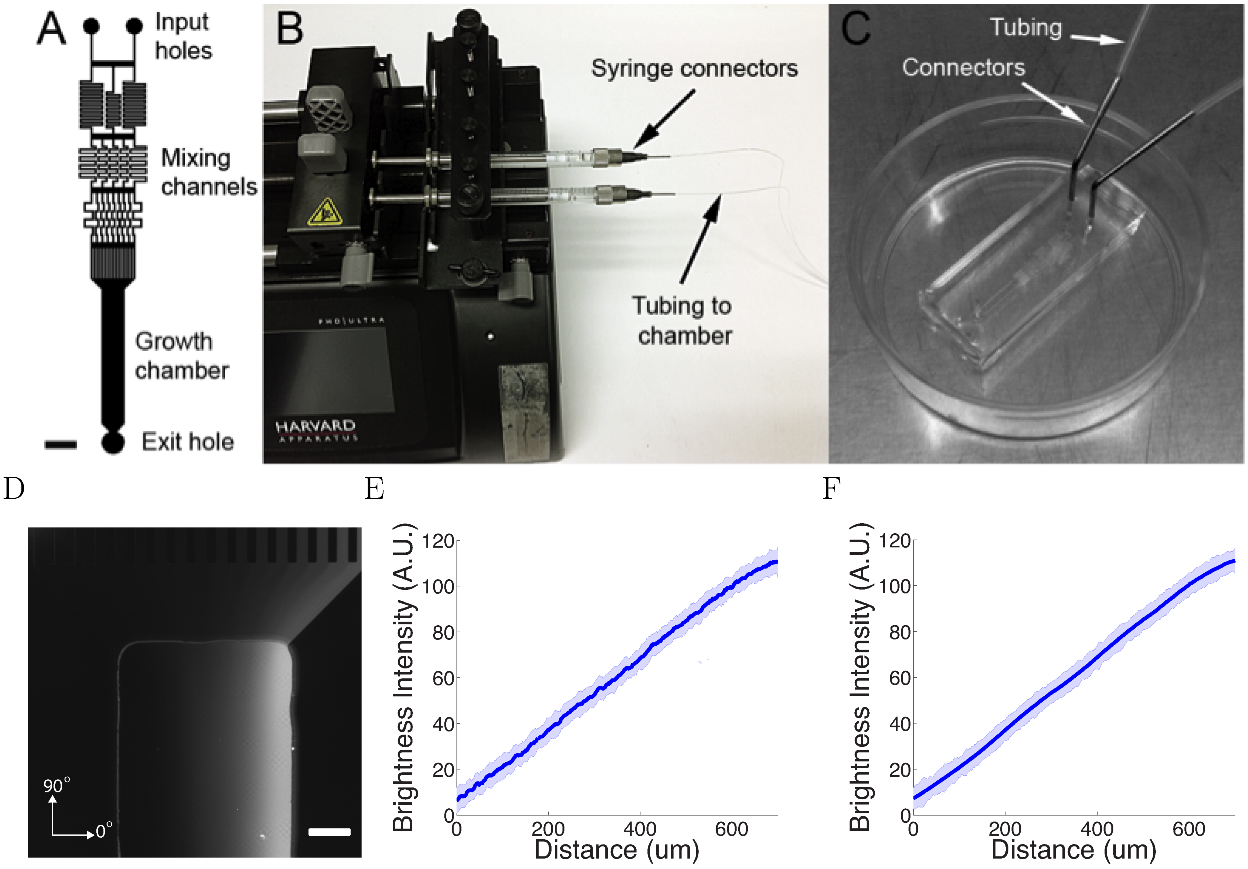

FIGURE 6.3: **The microfluidic assay.** A, The design of the chamber: the two solutions were pumped into the inlets and mix in the mixing channels before flowing into the growth chamber where the cells are plated. The mixing channels were of height 50 μm and width 50 μm. Scale bar 1 mm. B,C, Photo of the experimental setup: two glass syringes attached to a Harvard pump injected the solutions into the chamber bonded on a 35mm plastic plate. D, Two solutions, one of which contained 0.1% (v/v) dextran fluorescently labelled with tetramethylrhodamine, were used to visualize the gradient. Brighter regions indicate higher concentrations. Scale bar 200 μm. E, F. Line-scan measurements of fluorescence intensity across the device show a linear gradient which persists for at least 20 hours ($t = 0$h (E) and $t = 20$h (F)). The shaded errorbars show standard deviations across 10 chambers.

Three conditions were investigated: a control without flow or gradient, an attractive gradient of nerve growth factor (NGF) and a gradient of NGF with added KT5720, which converts attraction to repulsion by lowering levels of cAMP in the growth cone ([80]). Cells were injected into the growing chambers and grown for 2 hours before gradient onset. In the control condition, cells were grown over several hours with 0.3 nM NGF. In the NGF gradient condition, two solutions of concentrations 0 nM and 10 nM NGF were pumped into the growing chamber through the two inlets. Previous work using Scatchard analysis estimated that $K_d = 0.9 \pm 0.3$ nM [271] and showed that SCG neuronal outgrowth is severely inhibited at the saturating NGF concentration of 40 nM [272]. Given the healthy growth in our assay, it is clear the

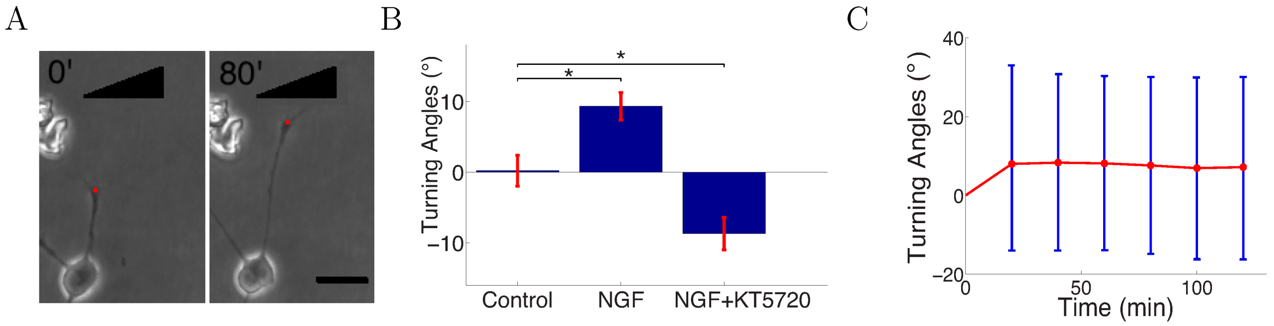

FIGURE 6.4: **Turning in microfluidic gradients.** A. Images of a representative axon initially almost perpendicular to the gradient at the beginning and end of the measurement after 80 min. Scale bar 20 μm. The red dots are the positions of the growth cone. B, Summary of turning angles in the 3 conditions (mean ± SEM): control $0.2 \pm 2.1°$ (n=120), NGF gradient (0-10 nM) $9.3 \pm 1.9°$ (n=143), NGF gradient (0-10 nM) + KT5720 $-8.8 \pm 2.2°$ (n=112). *: $p < 0.01$ t-test in both cases. C. The means (red) and standard deviations (blue) of turning angles of 143 axons over time for the attractive case.

concentration in the gradient condition was below saturation point. We analyzed trajectories for 300 axons per condition. These were obtained from 23 individual chambers in the control case, 27 chambers in the NGF gradient case, and 24 chambers in the NGF gradient plus KT5720 case. In most experiments, 2 chambers were run in parallel, so the total numbers of experiments in each case were 12, 15 and 13 respectively. For the measurement of turning angles we selected only axons that started growing between 70° and 110° relative to the gradient (when present). An asymmetric concentration field of guidance cue across the growth cone leads to turning [80, 156, 157, 252] and axons growing in this range experienced between 94% (i.e. $\sin 70°$) to 100% (i.e. $\sin 90°$) of the maximum possible concentration difference across the growth cone. Thus we expected the impact of the gradient would be strongest on these axons (Fig 6.4A). We tracked the growth cones every 5 minutes for as long as possible until they collapsed or branched or collided with other cells, axons or the edges of the chamber. The SCG axons were clearly attracted in the NGF gradient (Fig 6.4B). When the protein kinase A inhibitor KT5720 was added to the high and low solutions at concentration 70 nM, attraction was converted into repulsion as previously described [61, 80] (Fig 6.4B). These results confirm that the gradient in the microfluidic assay elicited a guidance response in SCG axons. From the timelapse imaging data, we then selected the subset of axons that did not branch or retract following growth for several hours in the attractive NGF gradient, and measured the turning angles of the population over time. The average turning angle reached the steady state quickly and did not increase significantly with time, matching the prediction of the model (Fig 6.4C).

The gradient did not affect axon branching

One possible way that the gradient could affect the axons is by causing biased branching (c.f. [273]), or changes in branching rates. To test whether the NGF gradient changed the branch extension and retraction rates, we compared the number of branches per cell after 5 hours of growth and did not detect any difference ($p = 0.9$ Kolmogorov–Smirnov test, Fig 6.5A). We measured the intervals between successive branching events in the same cell in each condition and did not find any difference in the branching rate ($p = 0.7$ Kolmogorov–Smirnov test, Fig 6.5B). Similarly, the lifetimes of the branches were unaffected by the gradient ($p = 0.2$

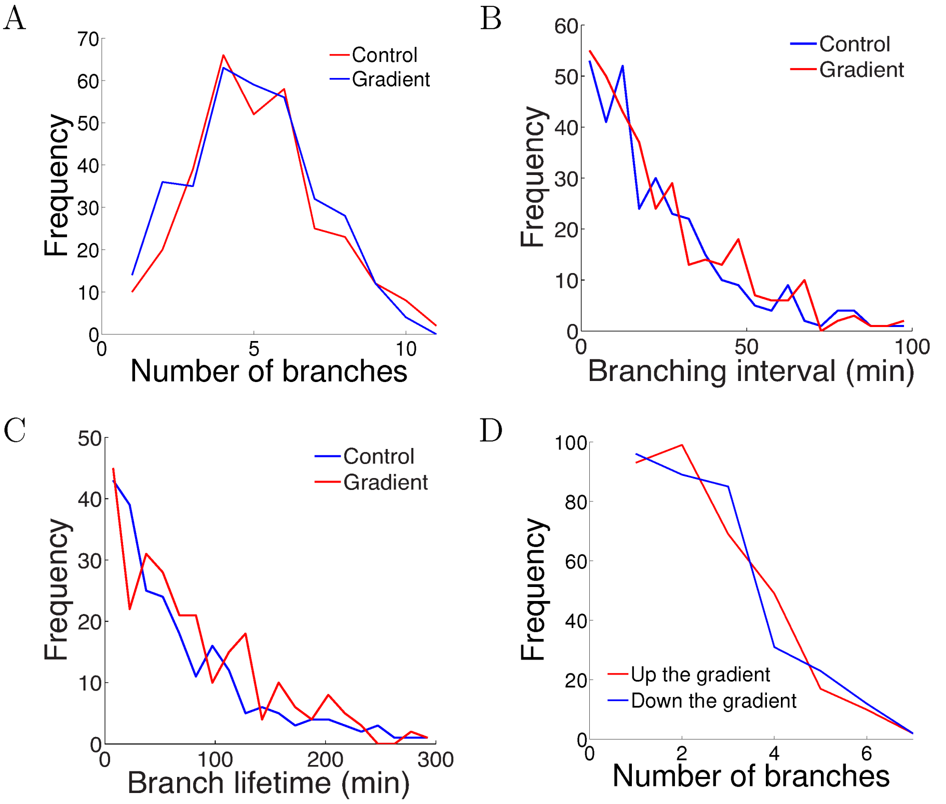

FIGURE 6.5: **The gradient did not affect branch extension and retraction rates.** A. Histogram of the number of cells with different numbers of branches after 5 hours of growth. The number (mean ± std) of branches per neuron in the control condition was 4.2 ± 1.8 (n=324 cells) and in the gradient condition was 4.4 ± 1.9 (n=297 cells), $p = 0.9$ Kolmogorov–Smirnov test. B, The distribution of interval times between two successive branching events of the same cell. The interval (mean ± std) in the control condition was 23.1 ± 22.8 min (n=315 intervals) and in the gradient condition was 24.1 ± 23.5 min (n=287 intervals), $p = 0.7$ KS test. C. Branch lifetime (mean ± std) in the control condition was 87 ± 79 min (n=245 branches) and in the gradient condition was 92 ± 81 min (n=213 branches), $p = 0.2$ KS test. D. Histogram of the number of branches pointing up the gradient vs down the gradient ($p = 0.8$, KS test).

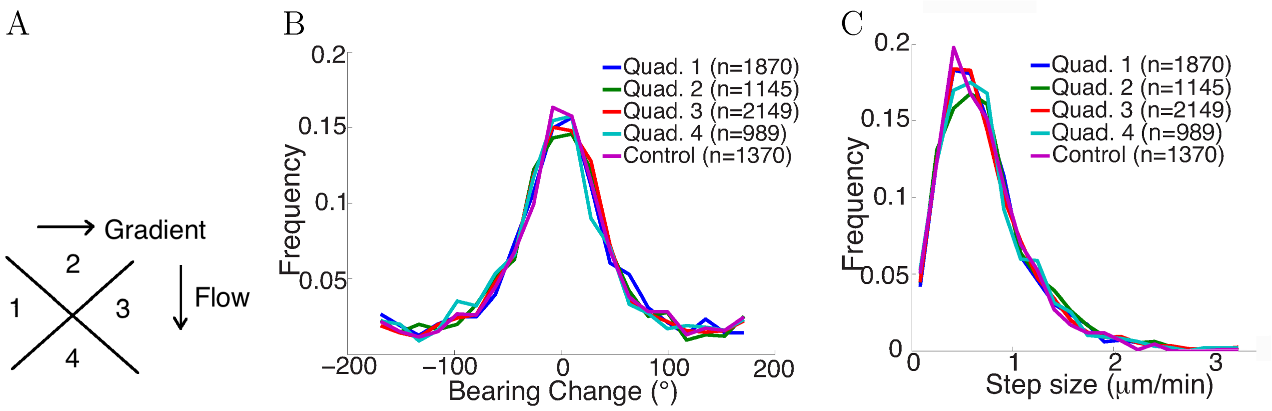

FIGURE 6.6: **Flow did not affect step statistics.** A. Axons growing in different directions were grouped into four quadrants. B. Growth cones' step sizes in different quadrants. n values refer to the number of steps in each quadrant. There was no significant difference between the quadrants ($p = 0.7$ Kruskal-Wallis test). C. Grow cones' bearing changes in different quadrants ($p = 0.4$ Kruskal-Wallis test).

Kolmogorov–Smirnov test, Fig 6.5C). We counted the number of branches pointing up and down the gradient per cell and did not find any difference ($p = 0.8$ Kolmogorov–Smirnov test, Fig 6.5.D). Thus the gradient had no effect on axon branching and retraction.

Flow did not affect the statistics of steps

To test whether fluid flow in the chamber biased the statistics of the steps, axons growing in the gradient condition with fluid flow were divided into 4 quadrants with different relative angles to the fluid flow: 2 quadrants growing perpendicular to the flow, one quadrant growing with the flow, and the other growing against the flow (Fig 6.6A). Comparing the distribution of bearing changes between the 4 quadrants, and with axons from the control condition without any flow, showed no influence of the flow ($p = 0.7$ in Fig 6.6B and $p = 0.4$ in Fig 6.6C, Kruskal-Wallis test). The means of the bearing changes in quadrants 2 and 4 were non-zero, and the bearing changes accumulated over time to result in a non-zero average turning angle of the population. However, these differences in means were very small (approximately 1°), and there were no significant statistical difference among the distributions. Therefore, the positive turning angles in the NGF gradient (and negative turning angles in the NGF gradient + KT5720) were due to the effect of the gradient, not bias from the flow.

Growth cone trajectories were generally straight

Axon growth is shown in Videos 1-3 and Fig 6.7A-C. The growth cone often wandered quite randomly, but nevertheless usually the axon segment remained very straight from the growth cone to the cell body or last axon branch point (Fig 6.7A-C). This implies that often the entire axon segment was pulled sideways across the substrate (as can be seen directly in the movies). Thus despite the irregular trajectory of the centre of the growth cone, the tension force on the growth cone from the axon was usually pointing directly back to the last anchor point, consistent with the assumptions of the model. To quantify this further, we measured the angle of this 20 μm segment and the angle to the anchor point ϕ and found them to be almost the same (Fig6.7E). Thus we can understand the term ϕ as the tension due to the most distal segment.

The trajectories (i.e. the locus of the centre of the growth cone) in three conditions are plotted in Figs 6.8, 6.9, 6.10. Note that these paths are not the same as the final image of the axon, which generally pointed straight back from the final position of the growth cone to the anchor point. Visually, the paths appear mostly straight with occasional large turns, consistent with a long tail for the bearing change distribution. The mean straightness index for the trajectories was $S = 0.72$. (Fig 6.11A).

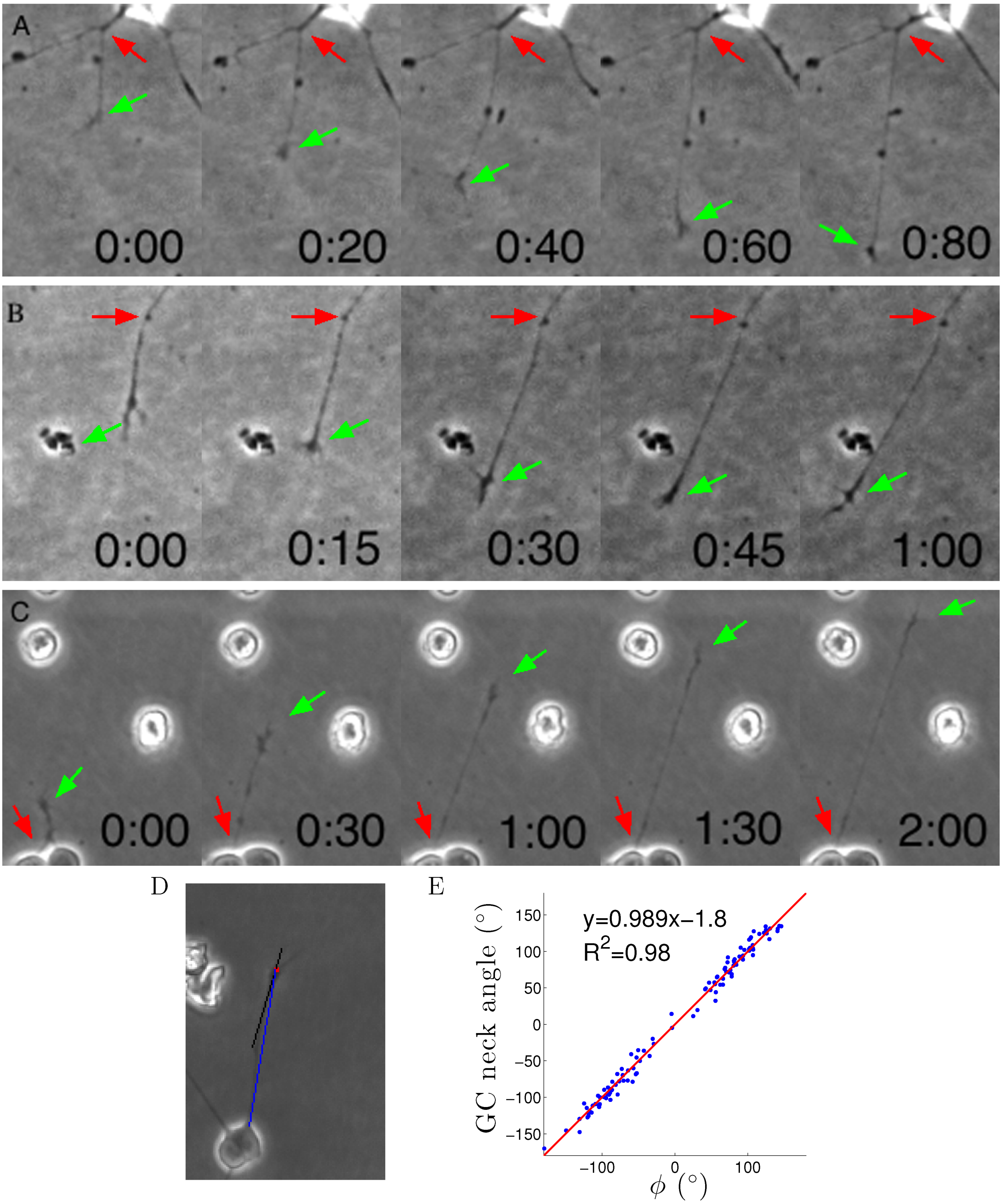

Figure 6.7: **Axons were dragged by growth cones.** A-C. Timelapse images of 3 example growth cones. Red arrows point to the putative anchor points and green arrows point to the growth cones. Time is shown in hours and minutes. D. We measured the angle of the neck of the growth cone (the last 20 μm, black line) and the overall growth cone angle (blue line) after one hour from the start of the experiment. E. The two angles were highly correlated, due to the straightness of the axon.

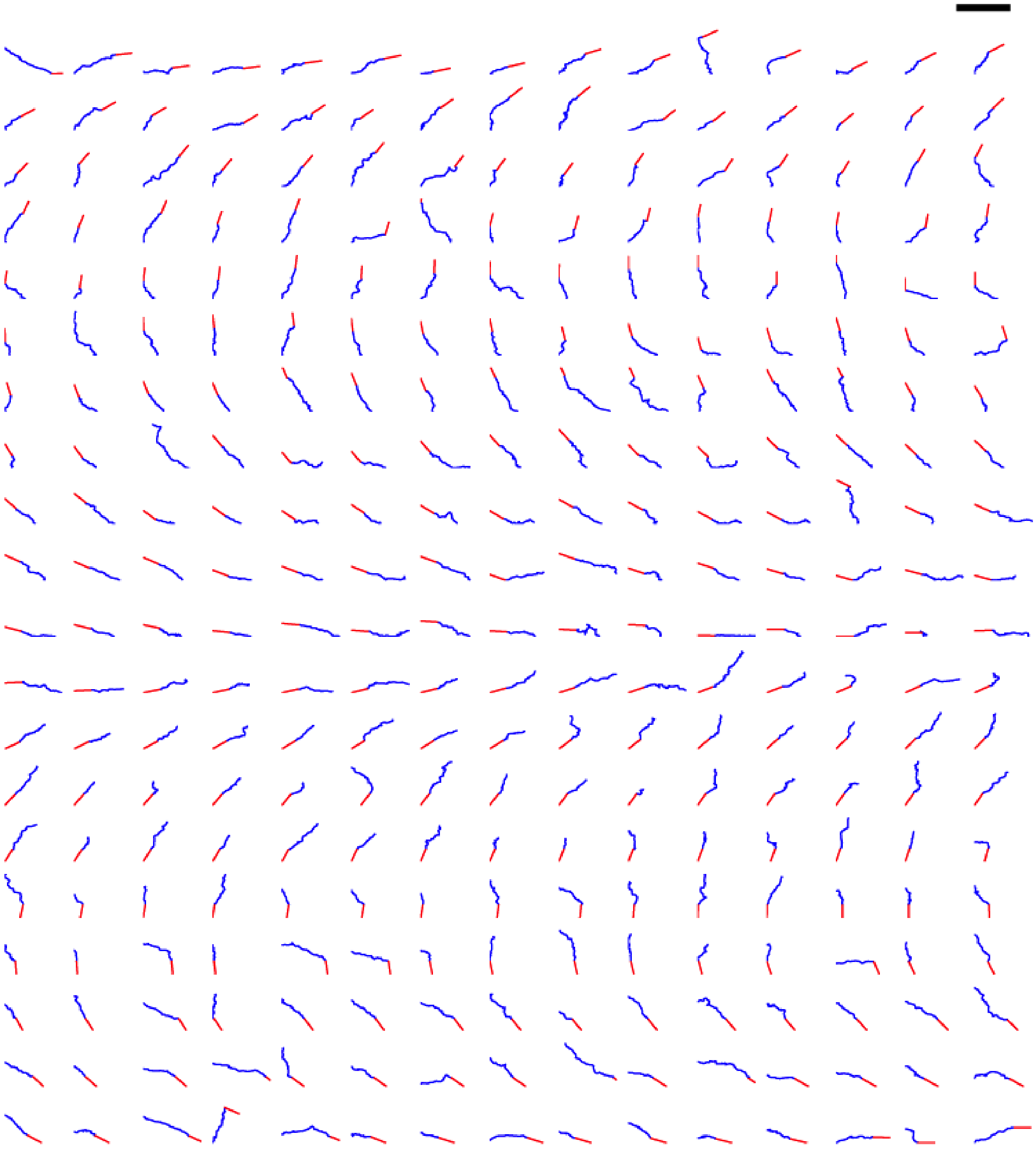

FIGURE 6.8: **Trajectories of 300 axons growing over 80 minutes in the control condition, ordered by the initial angle.** The red segments indicate the initial direction of the axon and the blue segments show the traces of the growth cones' trajectories. Scale bar = 100 μm.

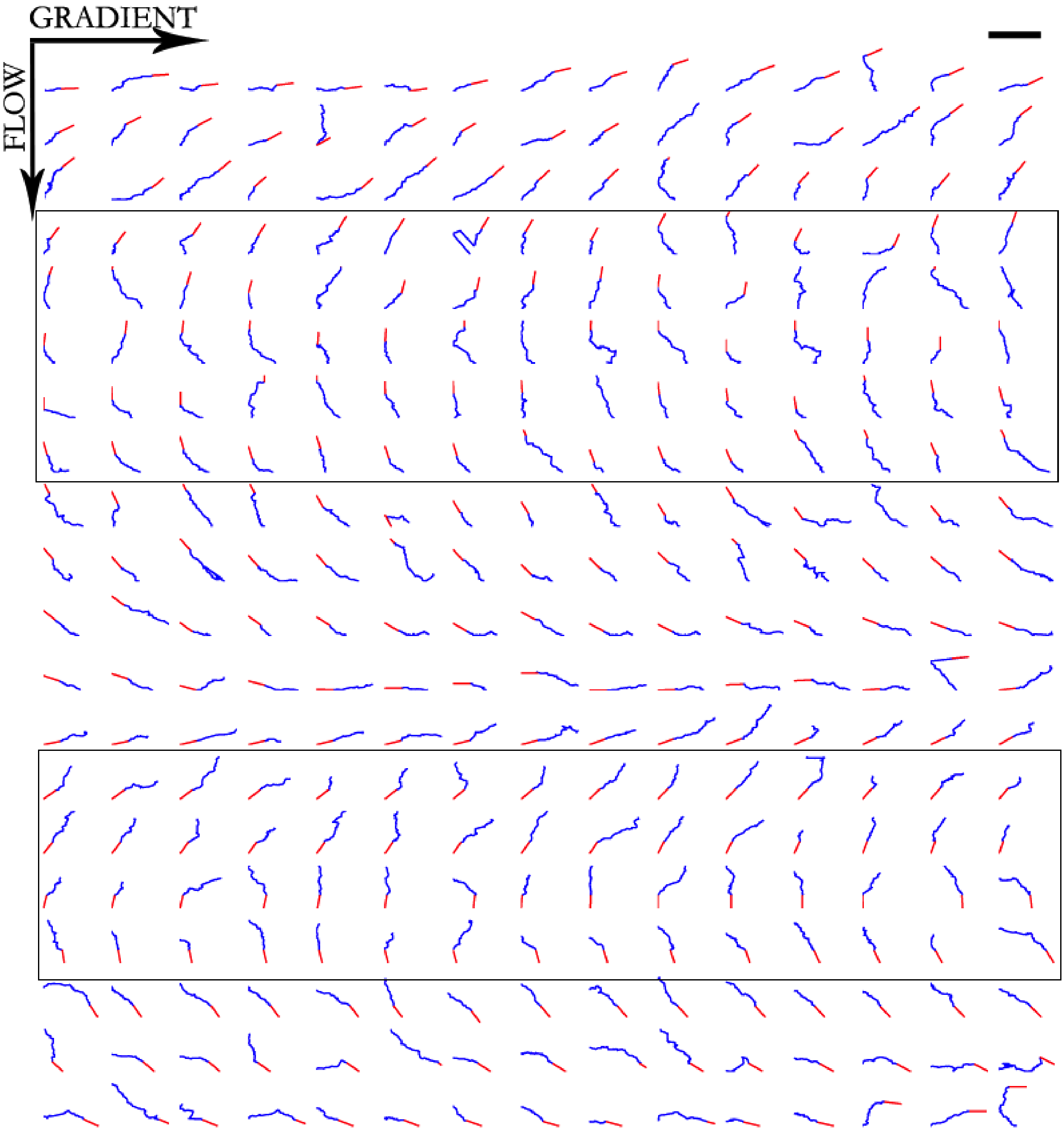

FIGURE 6.9: **Trajectories of 300 axons growing over 80 minutes in the NGF gradient, ordered by the initial angle.** Only axons in the box were selected for turning angle measurements as they were almost perpendicular to the gradient, hence most affected by it. Scale bar = 100 μm.

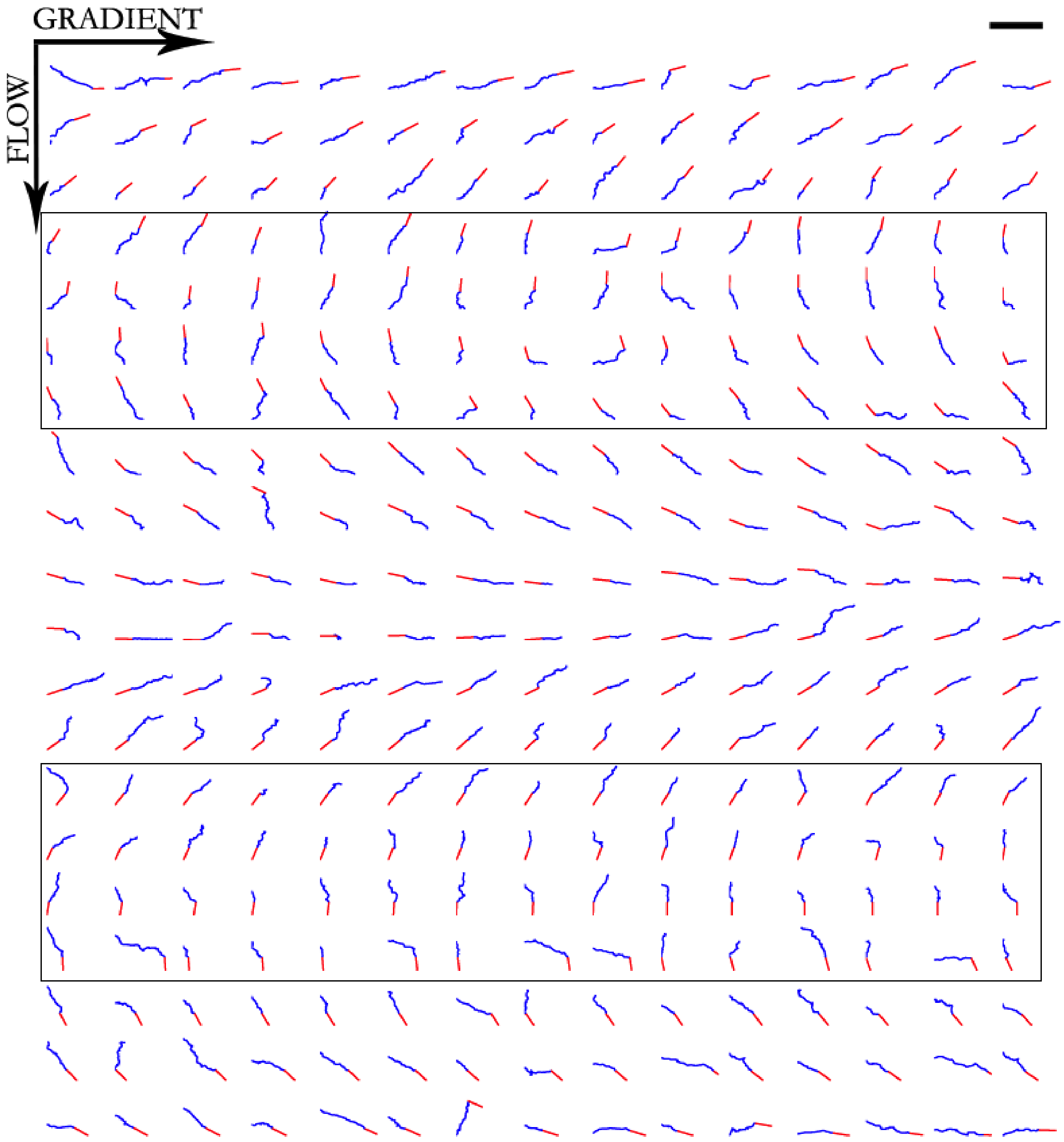

Figure 6.10: **Trajectories of 300 axons growing over 80 minutes in the NGF gradient with 70 nM KT5720 added, ordered by the initial angle.** Only axons in the box were selected for turning angle measurements. Scale bar = 100 μm.

Step size and bearing change distributions were similar across conditions

There was little correlation between the bearing change magnitude and step size (Fig 6.11B). The distribution of bearing changes in radians was well fitted by a mixture of a von Mises and a

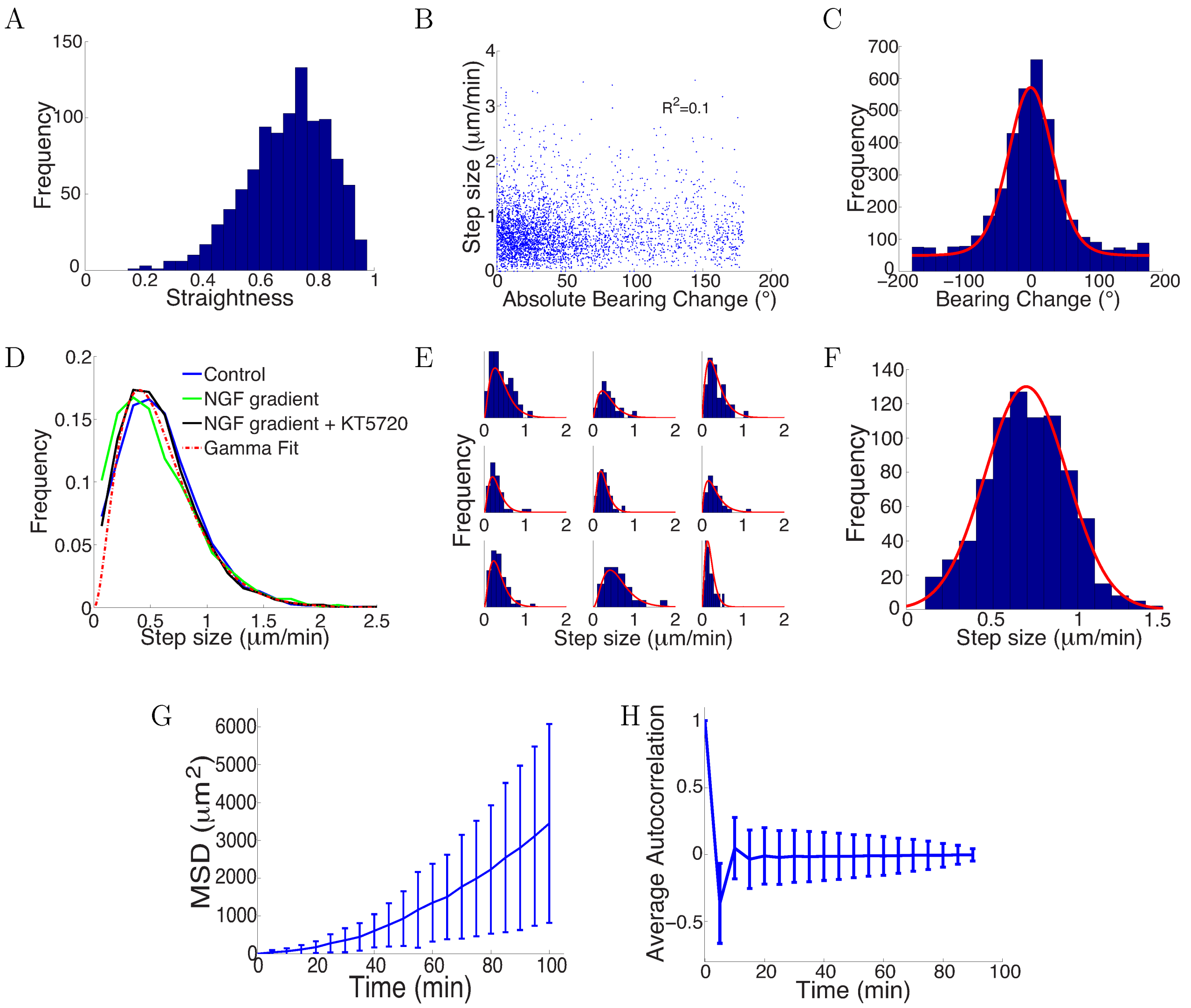

Figure 6.11: **Trajectories were straight with step sizes and bearing changes independent of each other** A. Distribution of straightness indices of all paths with mean straightness of 0.72. B. There was no correlation between bearing change and step size ($R^2 = 0.1, p = 0.7$). C. The distribution of bearing changes (blue) in radians in the control condition can be fitted to a mixture of two von Mises distributions (red) $P(x) = 0.5\frac{\exp(3\cos(x))}{2\pi I_0(3)} + 0.03$. D. Step sizes in the control, attractive and repulsive gradients conditions were similar and well-fitted by the gamma distribution $P(x) \propto x^2 \exp(-x/24)$ (red). E. Step sizes of individual growth cones (blue) can be described by gamma distributions (red) (9 examples shown). F. This distribution of the average step sizes (blue) of individual growth cones was well-fitted by a Gaussian distribution $\mathcal{N}(0.7, 0.24)$ (red). G. Mean square displacement and standard deviation of 300 growth cones growing over 100 mins in the control condition was super-linear, indicating that growth cone trajectories were straighter than predicted by a simple random walk. H. Autocorrelation of bearing changes (mean ± STD) showed that successive bearing changes were anti-correlated.

uniform distribution ($-\pi < x < \pi$) (Fig 6.11C). That is there was a great deal of randomness in bearing changes, but with a peak in probability near the forward direction. Thus growth cones tended to move in a straight line instead of turning uniformly randomly. This is inconsistent with the assumptions of several previous models [124, 125, 129].

Accumulating across all the growth cones, the distributions of step sizes over 5 min were statistically indistinguishable across the three conditions (Kruskal-Wallis test $p = 0.35$), and were well fitted by a gamma distribution (Fig 6.11D). That is, the most likely step size was around 0.5 μm/min, but the distribution had a long tail, so that longer step sizes were also seen. The distribution of step sizes for each individual growth cone were also well fit by gamma distributions (Fig 6.11E). However, individual growth cones had idiosyncratic mean values. The distribution of these mean values could be well fitted by a Gaussian distribution (Fig 6.11F).

Nevertheless, the mean square displacement was clearly not linear, implying that a simple random walk is not suitable to describe the movement (Fig 6.11G). Successive steps were anti-correlated (Fig 6.11H), which was not accounted for in a previous model [123]. This helps the paths remain relatively straight: if successive steps were positively correlated, the paths would become more bent over time. Due to large noise in the bearing changes, bearing changes more than one step apart were uncorrelated.

Turning angles over time were well predicted by the model

Having established the key statistics of steps from the data, we now asked if the simple model in equation (6.1) could replicate the observed trajectories and explain the phenomenon of saturated turning. We sampled the mean speed v_{mean} of each growth cone from a truncated Gaussian distribution of mean 0.7 μm/min and standard deviation 0.24 μm/min. At each time point (5 minute interval), the growth cone sampled a step size from the gamma distribution $\Gamma(4/u, v_{mean} * u/4)$ where u was a uniform random number. The bearing changes evolved according to equation (6.1). We found that the random noise ξ in bearing changes (in radians) could be well fit by the mixture von Mises distribution

$$P(\xi) = c\frac{\exp(d\cos(\xi))}{2\pi I_0(d)} + (1-c)$$

where c and d are parameters to be fit. This distribution is not necessarily the same as that of the bearing changes in Fig 6.11F. As the bearing change is the sum of three random terms,

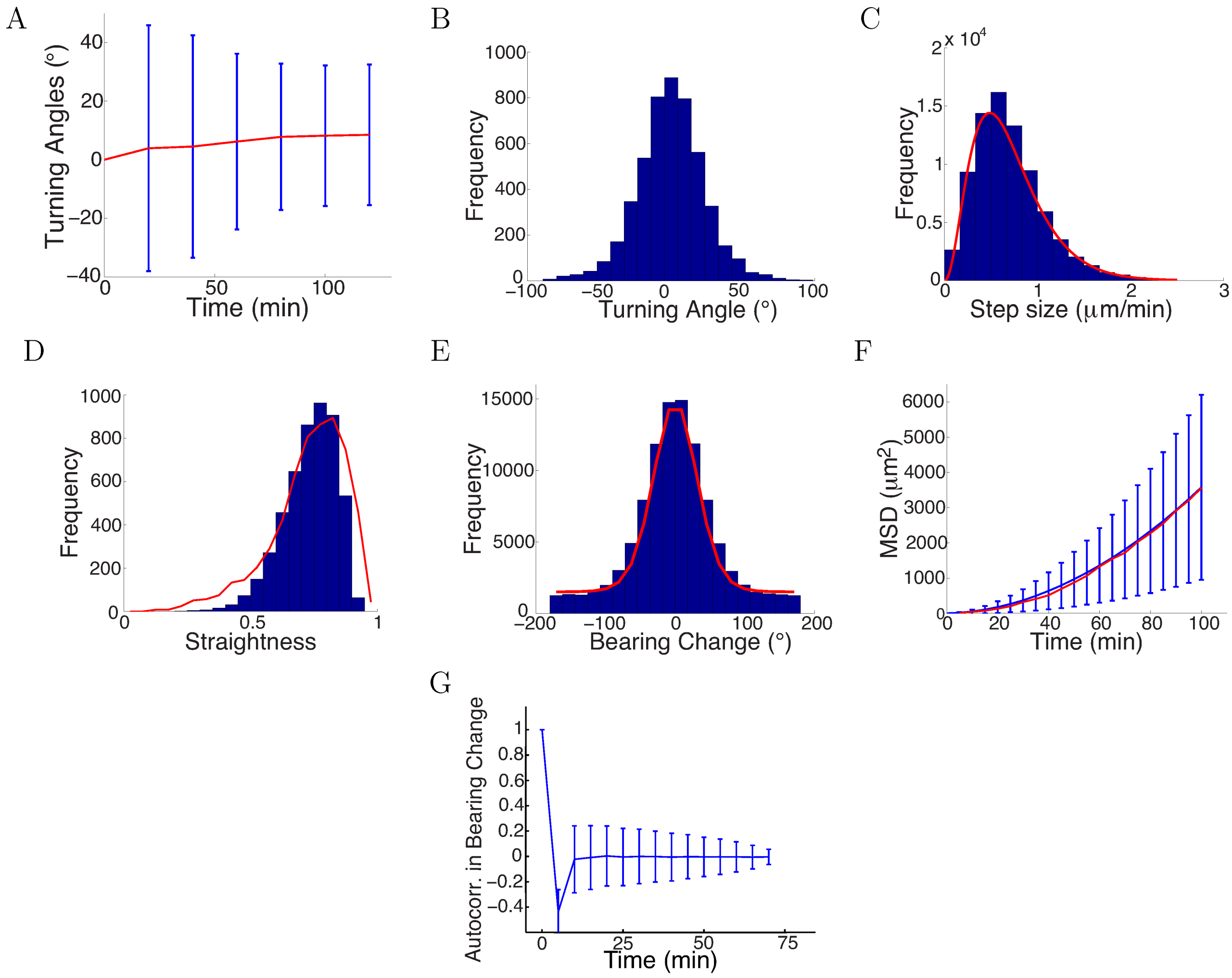

FIGURE 6.12: **Model captured key statistics of trajectories.** A. The evolution of simulated turning angles (mean ± STD) of n=5000 growth cones over time in the attractive gradient condition. B. Simulated turning angles after 16 steps (80 min) had mean 9.8° and standard deviation of 24.2°, similar to the empirical data in red in Fig 6.4B. C. Distribution of simulated step lengths (blue), fitted with the empirical distribution (red). D. Straightness of simulated trajectories (mean 0.75, blue), compared with empirical distribution (red) ($p = 0.2$, t-test). E. Simulated bearing changes (blue) fitted with the mixture of von Mises distributions given in Fig. 6.11D (red). F. Mean square displacement of simulations (blue) and data (red). G. Autocorrelation of simulated bearing changes.

its distribution is broader than the distribution of the noise term. To estimate the four free parameters a, b, c, d, we input the initiation angles $\phi(0)$ and used the model to generate the distribution of turning angles ψ_{turn}. We then estimated the likelihood function that the turning angle data was generated from the model with the given parameters $\mathcal{L}(\psi_{turn}|a, b, c, d, \phi(0))$.

We found the values of a, b, c, d that maximized the likelihood (the parameters mostly likely to have generated our empirical turning angle data) were $a = 0.7$, $b = 0.09$, $c = 0.75$, $d = 6$. The statistics over 5000 simulated trajectories using these parameters are shown in Fig 6.12,

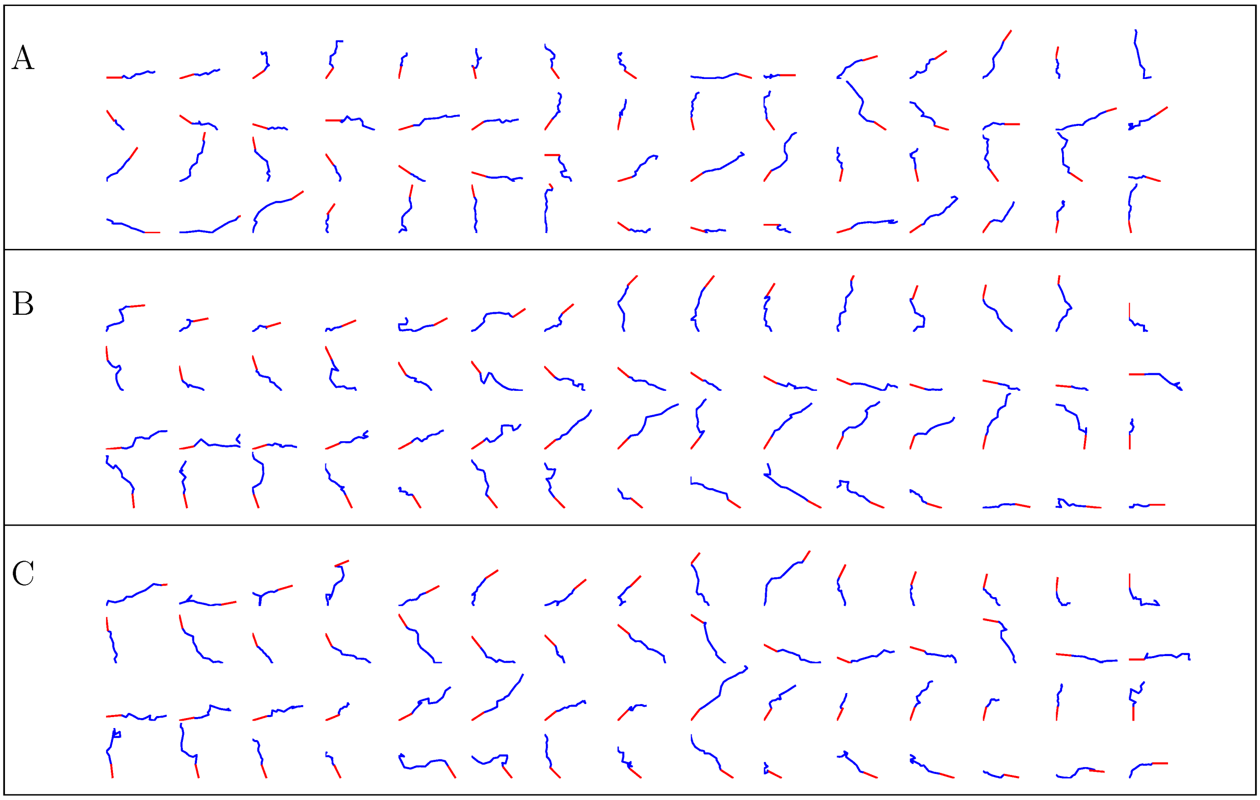

Figure 6.13: **Simulated trajectories from 3 conditions**. A. control, B. NGF gradient, C. NGF gradient + KT5720.

and some example trajectories are shown in Fig. 6.13. Similarly, we fitted the model to the control data and repulsive gradient and found b = 0.002 and b=-0.08 respectively, with other parameters remaining at very similar values as before. Notably, the simulated turning angles changed little over time (Fig 6.12A), consistent with our preliminary prediction and the data (Fig 6.1E, 6.4C). Thus, with realistic step sizes and bearing change noise distributions, the model was able to capture the phenomenon of saturated turning with quantitatively accurate means and variances over time. The distribution of turning angles and step sizes also closely matched the real data (Fig 6.12B, C). The simulated straightness distribution was also very similar to the real distribution ($p = 0.2$, t-test) (Fig 6.12D). The model also captured the distribution of bearing changes, the mean square displacement and the anticorrelation between successive bearing change, which was a consequence of the persistence term straightening the paths (Fig 6.12D-F). If successive steps were positively correlated, the paths would become more bent over time. This correlation was rapidly lost beyond one time lag because of the large noise.

Unlike previous models, we did not assume constant steps or a uniform distribution of bearing changes but rather derived these from empirical data. The model was then able to predict the evolution of the average turning angle over time, the straightness profile and the anticorrelation in bearing changes. Most importantly, it could explain the phenomenon of slow and saturated turning, due to a weak bias term relative to the persistence term. A microscope factor in each step led to a macroscope phenomenon of limited, variable turning and straight paths. This often overlooked feature of axon growth turned out to be critical in our model in limiting the overall turning. We also found little difference between the attractive and repulsive case, indicating that attractive and repulsive gradients employed similar mechanisms and could not reduce the variability of axon trajectories.

Multiple anchor points achieved sharp turns but also increased variability

The *in vitro* data we have presented here was well-fitted by assuming the only anchor point is where the axon emerges from the soma or the branch point. However the *in vivo* environment is much more complex, and axons may establish anchor points with the substrate at multiple positions as they extend. We therefore investigated in the model what effect this would have on turning angles. We assumed that at each timestep, the probability of that point becoming a new anchor point was fixed, while leaving the evolution at each step as before. The average number of anchor points per timestep (i.e. 5 min) is denoted by r.

We analyzed two cases: anchoring probabilistically at each time step (Fig 6.14A-C), and anchoring at regular intervals (Fig 6.14D-F). We simulated the trajectories for $T = 150$ timesteps with the same parameters as Fig 6.2A ($a = 1, b = 0.1, \xi = 0$ or $\xi \sim \mathcal{N}(0, \pi/4)$ radians). In both cases, more anchor points led to sharp turns in the trajectories and larger mean turning angle (Fig 6.14G), since the growth cone now was more free from its initial position. However, it increased the variability in the turning (Fig 6.14G). Given the same rate of anchoring, whether the growth cone put down new anchor points probabilistically or regularly made little difference to the mean turning. We compared the mean square final angle $\langle \phi(T)^2 \rangle$ which is the sum of the bias $\langle \phi(T) \rangle^2$ and the variance $(\phi(T))$. Ideally the growth cone should completely align with the gradient, i.e. $\phi(T) = 0$. Fig 6.14H shows the bias/variance trade off. Although more

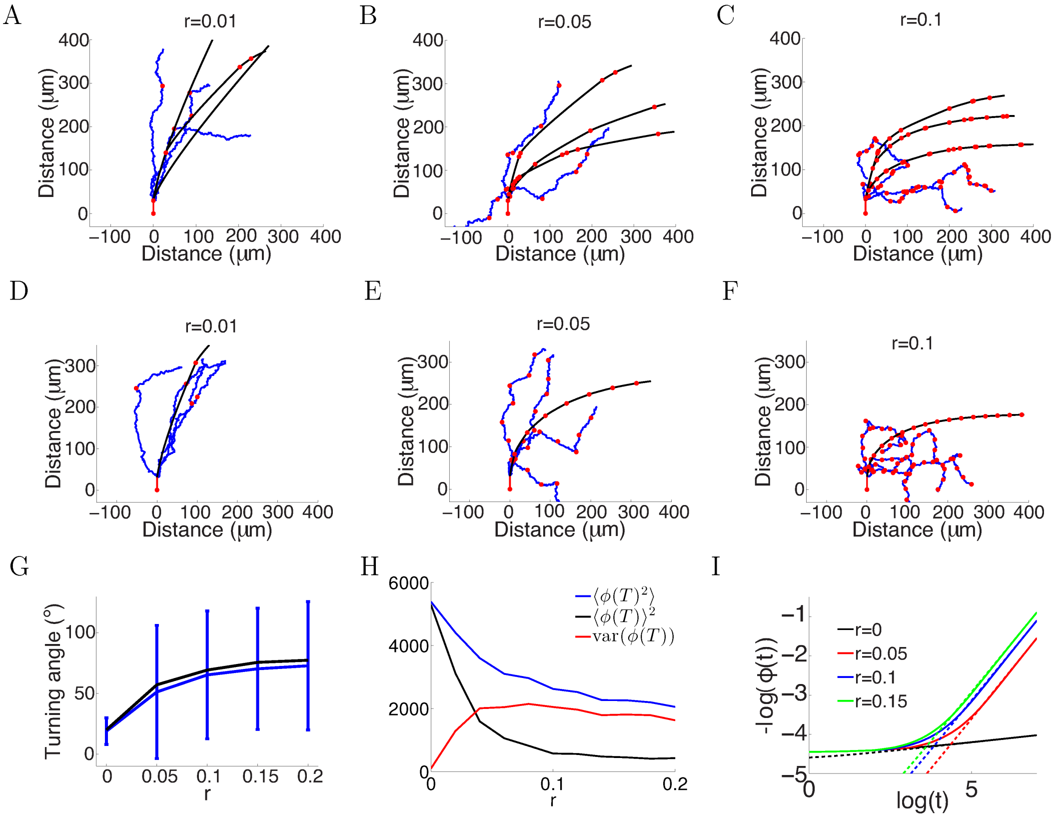

FIGURE 6.14: **More variability with more anchor points.** A-C. Trajectories of growth cones with probability of putting down a new anchor r= 0.01, 0.05, 0.1 at each timestep and the same parameters as Figure 6.2A ($a = 1, b = 0.1, T = 150$ timesteps). The black plots are without noise in the bearing changes, the blue plots are with noise $\xi \sim \mathcal{N}(0, \pi/4)$ radians in the bearing changes and the red dots are the anchor points. More anchor points lead to higher variability but also stronger turning. The means and standard deviations of turning angles and the values for the noiseless versus the noisy case in brackets for r= 0.01, 0.05, 0.1 are 32±9° (30 ± 36°), 55±8° (49 ± 57°) and 67±5° (60 ± 56°) respectively. D-F. Trajectories of growth cones with the same rate of putting down new anchor points as A-C but at regular intervals. The means and standard deviations of turning angles and the values for the noiseless versus the noisy case in brackets are 27° (24 ± 17°), 57° (54 ± 51°), 69° (66 ± 51°). G. The means and standard deviations of turning angles after 150 timesteps as a function of the anchoring rate at regular intervals in the noiseless and the noisy case. H. The mean square of the final growth cone angle (in degrees) $\langle\phi(T)^2\rangle$ for different anchoring rates r after 150 steps. $\langle\phi(T)^2\rangle$ is the sum of the bias term $\langle\phi(T)\rangle^2$ and the variance term $\mathrm{var}(\phi(T))$. Although more anchor points add more variance to the final angle (red curve), they achieve stronger turning $\phi(T) \approx 0$ (black curve). I. The evolution of $\phi(t)$ over time, for the case of anchoring at regular intervals and no noise in the movement ($\xi = 0$). With more anchor points, $\phi(t)$ also follows the power law but with steeper slope, meaning that $\phi(t) \to 0$ at a faster rate than the case without anchor points.

anchor points introduced larger variance in the final angle, they achieved greater turning, i.e. smaller $\phi(T)$.

Fig 6.14I shows that in the case without movement noise ($\xi = 0$) and regular anchoring, the growth cone angle $\phi(t)$ also followed a power law in the large t limit, similarly to the case without anchoring (Fig 6.1C). However, the exponent of this power law was larger, demonstrated by a steeper slope between $\log(t)$ and $\log(\phi(t))$, meaning that the growth cone aligned with the gradient faster with more anchor points. Thus, increasing the rate of anchoring leads to stronger turning, but increases the variance of the responses.

6.4 Discussion

Here we presented a model of axon trajectories in gradients and helped resolve the mystery of why axon turning angles in gradients saturate over time *in vitro*, revealing an important factor limiting axon turning. We found that the movement of the growth cone was strongly influenced by the axon's tendency to maintain a straight trajectory forward, limiting the directional effect of the gradient and preventing the axon from aligning with the gradient even after a long time. Our model predicted that, averaged over a large population of axons, the initial rate of turning drops rapidly over a short period of time (20- 40 minutes). The model shows that adding more anchor points can give the growth cone more flexibility and produce larger average turning, but also increases the variability. Thus we predict that different substrates, producing different densities of anchor points, could result in different trajectories for the same gradient conditions.

The application of forces to axons can induce rapid elongation without axonal thinning, and thus stretch can stimulate growth [274]. Furthermore, stretch can also regulate the mode of growth. When axons are tightly bound to a sticky substrate, stretching only happens at the tip and axons elongate by tip growth. In contrast if axons grow relatively unattached to the substrate, they will lengthen by stretching due to the pull of the growth cone [37, 275], which appears to be the case in our experimental condition. The tension along the axon will cause stimulation of growth in the existing direction producing straighter trajectories. The stiffness of axons is also important [276], and stiffer axons will likely have higher persistence due to their more limited ability to bend.

This tension results from cytoskeletal coupling with adhesive interactions to the substrate and is critical to growth cone migration [277, 278]. Although anchor points are an abstraction in our model, their biological implementation may be focal adhesions. Only at these points is the axon firmly attached to the substrate. There a number of ways in which anchor points could be investigated experimentally in future work. Axons could be stained for proteins such as integrins ([267]) to test whether their distribution is strongly localized to particular points along the axon. We also predict that applying force orthogonal to the direction of axon growth, for instance by using a pipette to puff liquid at different locations along the axon, would cause a deflection of the axon of a size related to the distance from the nearest anchor point. A similar experiment was performed using a glass needle to tow axons [37]. It was observed that the distal region of the axon was free of the substrate while the proximal region was firmly attached. In addition, it could be possible to determine the internal stress field of an axon, as has been done for growth cones [265]: we would expect the stress to in general be different on the two sides of an anchor point. The density of anchor points will depend on the components of the extracellular matrix (ECM). In our experiments, on laminin, they appeared to be rare. This might be because adhesion points are expensive to produce and the axon can grow faster when it is not attached to the substrate [275]. However the biological factors governing when new anchor points are generated are unknown.

Tension is also dependent on cell type and two main properties of the substrate: stiffness and ECM components. Our data comes from peripheral nervous system (PNS) neurons growing on a laminin substrate that is hard rather than gel-like, and other cell types of different substrates might have different behaviours. Central nervous system (CNS) and PNS neurons have different sensitivities to substrate stiffness due to adaptation to their natural environments [34], and traction force *in vitro* increased on stiffer substrates [34]. Substrates with different ECM components differentially promote growth cone motility and point contact formation. For example, growth cones are more highly motile and neurites extend more rapidly on laminin than fibronectin because point contacts have higher turnover rate [279].

Overall our work suggests that without many anchor points, cues additional to gradients may be necessary for axons to reliably find their targets *in vivo* (unless the motility noise is for some reason much lower *in vivo* than *in vitro*). These could include mechanical cues and axon-axon interactions. To understand such interactions, it is important to generate assays with realistic substrates suitable for different cell types. Recent 3D culture models, in which cells are grown with a protein scaffold, can capture some aspects of the tissue environments instead of hard surfaces [280]. It will be interesting to see how different ECM properties lead to changes in trajectories and whether they can facilitate more reliable turning.

In conclusion, we have presented a simple mathematical model which gives accurate quantitative predictions of the properties of axonal trajectories in a microfluidics-based *in vitro* gradient assay. The model identifies the key importance of anchor points in controlling turning, and provides an explanation for why axonal turning in gradients *in vitro* tend to saturate rapidly at small turning angles. This model provides a predictive framework which can be used to test whether axonal trajectories observed *in vivo* can be explained purely in terms of gradient guidance, or whether additional guidance mechanisms are also required.

Chapter 7

Discussion and Conclusions

The aim of this thesis was to develop mathematical models that would lead to a better understanding of axon guidance in chemical gradients. I first presented a theoretical analysis of gradient sensing by receptors using a statistical framework, and then built a model of growth cone trajectories based on experimental data from microfluidic devices. Here we review the main findings of the models developed and suggest directions for future work.

7.1 Summary of findings

In chapters 3 and 4, we treated gradient sensing as a statistical inference computation that combines some prior knowledge about the gradient with sensory information coming from the receptor binding patterns. We assumed the growth cone acts as an 'ideal observer' that can optimally combine these two sources of information to derive the maximum *a posteriori* estimate of the gradient direction.

The first model developed in chapter 3 investigated the role of receptor diffusion in gradient sensing by a one-dimensional 'growth cone'. We assumed the prior distribution of the gradient is flat. Decisions about the gradient direction are made on the basis of noisy information from stochastic binding interactions between receptors and ligand molecules integrated over some measurement time. We assessed the potential quality of gradient sensing by calculating the Fisher Information between the gradient direction and the measurement. We assumed that the receptors only signal when bound and can diffuse freely on the cell membrane. The main results were:

- The potential quality of gradient sensing declines with increasing diffusion constant of the receptors. This result is intuitive because faster diffusion smears out positional information from receptors to a larger extent.
- The amount of information receptors can carry about the gradient increases with concentration of the ligand molecules. As found in [216], a higher concentration means more unbound and bound periods, i.e. more sampling within the measurement period, thus results in more information.
- The faster the kinetics of the binding, the better the receptors can sense the gradient, for the same reason as above.
- Although the receptors only signal when bound, only unbound times carry information about the ligand concentration. This is because only the binding rate, not the unbinding rate, depends on ligand concentration.
- Even if the receptors take time to change their conformation after binding and only start signalling after some delay, whether the receptors become immobilised and can still move freely when bound makes little difference to the potential quality of sensing. This is because the unbound times remain unchanged and uncertainties about receptor positions cancel each other out due to random, unbiased motion.

In chapter 4, we extended the model to a two-dimensional growth cone with fixed receptors. We used the Bayesian framework developed in [95] to incorporate priors that represent prior bias in the gradient estimation. We assumed an elliptical sensing device with randomly distributed receptors. The main results were:

- The quality of the sensing depends on the positions of the receptors, not the shape of the cell because the receptors sense and estimate the gradient.
- On an elliptical cell with uniformly randomly distributed receptors, the gradient sensing will be biased in the minor axis direction because of the unequal variances in the estimate

of the x and y components of the gradient. This leads to a biased distribution of the estimated angle.

- Eliminating this bias requires a non-uniform distribution of receptors, with more receptors near the minor axis and fewer near the major axis. The quality of the sensing is maximised when the receptors are farther away from the cell centre as the concentration change over the spatial extent of the receptors becomes larger.

In chapters 5 and 6, we described a novel microfluidic device that can generate stable linear gradients. Based on the data of superior cervical ganglion neuronal growth cones growing in a linear gradient of nerve growth factor, we found that:

- Growth cone movement was extremely variable and noisy. The presence of the gradient did not reduce this variability or change the statistics of the steps.
- The axons had a strong tendency to grow straight, thus growth cone trajectories were fairly straight. This tendency limited the amount of turning of growth cones due to the gradient. We speculated that this persistence to grow straight is due to the tension from the pull of the growth cone. The tension depends the nature of cell adhesion on the substrate and the cell type. Changing any of these factors will likely change the properties of the trajectories.
- We built a mathematical model in which the growth cone's random movement has the persistence to grow straight forward and is biased by the gradient. We first assumed there was only one anchor point where the axon is fixed on the substrate and then relaxed this assumption to allow the growth cone to put down more anchor points along its path.
- In our model, if the growth cone puts down more anchor points, it can achieve greater turning but the trajectory will be much more noisy. This is because the trajectory is 'reset' more frequently and becomes less constrained by the initial growth direction and history. This finding implies that stereotypical axon paths *in vivo* could only be achieved with multiple anchor points along the trajectory and small motility noise.

7.2 Discussion

Chapters 3 and 4 extended the previous framework of applying Bayesian inference in axon guidance and can apply to other chemotactic systems. Eukaryotic cells employ spatial gradient sensing meaning that the external gradient is detected by an asymmetric receptor activation pattern on the cell surface. They are all subject to the constraint imposed by stochastic ligand binding with moving receptors. The question of receptor diffusion has been underappreciated in existing models and the analysis showed that it can play an important role.

Ours is a more realistic model of receptors that only signal when they are bound. The diffusion of receptors necessitates the integration of receptor binding information over some measurement time. This is in contrast with other models that assume receptors are stationary and the cell can take a snapshot measurement of the binding pattern at one instant to infer the gradient. When receptors can diffuse, snapshot measurements no longer suffice to estimate the gradient because the receptors have been moving through different regions of the concentration field and lost their positional information. In order to estimate the gradient optimally, the sensing device sums up the total unbound times from all its receptors weighted by their average positions in the unbound period. The direction of this resultant vector is the estimate of the gradient direction. Interestingly, we found that if the gradient information comes from integrating over time instead of a snapshot, then the performance goes up with concentration. This result appears to contradict experimental results that showed a peak performance at an intermediate concentration [95]. However, it has been proposed in [216] that this is possibly due to a limit on production of downstream signalling molecules.

We also challenged the claim that bound receptors slow down or become immobilised to gain more precise spatial information beneficial for concentration sensing [105]. Our analysis points out that the random movements of the receptors cancel each other out and on average, the quality of gradient sensing does not improve whether the bound receptors become immobilised or not. The ligand concentration gradient information lies in the unbound periods.

In this work, we did not address other complex aspects of receptor behaviour such as endocytosis or clustering and such behaviours can be interesting targets for future analysis. It has been suggested in [281] that endocytosis and recycling can increase the rate at which independent concentration measurements can be made, increasing the quality of gradient estimation.

Another study [282] used Monte-Carlo simulations of ligand receptor binding and found that "apparent" affinity of the ligand for the receptor decreases with clustering. This implies a higher dissociation constant, which is beneficial when the ligand concentration is high and detrimental when it is low, inferred from the chemotactic performance curve in Fig 2.4B.

We used Michaelis-Menten model of receptor dynamics with the assumption that the ligand-receptor interactions are not limited by diffusion of ligands but the binding and unbinding rates. The seminal work by Berg and Purcell in 1977 [206] has inspired many theoretical models into the limits of gradient sensing due to ligand diffusion [207, 283, 284]. In their classic work, they considered a model in which a spherical cell infers the ligand concentration from time-averaged occupancy of a single receptor. Ligand molecules bind to the receptor then unbinds and diffuses away. The precision of this estimation depends on the diffusion constant of the ligand, the true concentration, the mean receptor occupancy, the integration time and the receptor-ligand binding cross section. Bialek and Setayeshgar extended this result by considering the association and dissociation rates between ligand molecules and receptors [207]. In our models, we ignored the diffusion of ligand molecules, assuming that the interactions are in the reaction-limited regime, meaning that the molecules diffuse much faster than binding kinetics.

We were unable to solve the optimal receptor positioning for a general elliptical cell. However, limited to a case of a circular receptor ring ($\sum r_x^2 = \sum r_y^2$), we found that the receptors are optimally placed to maximise $\sum r_i^2$ with r_i being the distance of the i^{th} receptor to the cell centre. We also found that the prior and likelihood interact in complex ways. Our results agree with a previous study in [99], showing the bias in an elliptical distribution of receptors and the dependence of gradient sensing on the number of receptors, the size of the receptor ring and the ligand concentration [95, 98].

Chapter 4 extended the previous results by incorporating the prior information, allowing a more general treatment in polarised cells. In other chemotactic systems, polarised cells tend to be significantly more sensitive to a chemoattractant gradient [285]. In polarised *Dictyostelium*, G-proteins are distributed asymmetrically with a higher concentration at the leading than trailing edge [285]. An interpretation of this is that polarised cells are already primed for a particular gradient direction. In our statistical framework, this polarisation encodes an asymmetric prior distribution. Bound receptors recruit and activate G-proteins resulting in downstream activity that might represent the posterior distribution Alternatively, the distribution of signalling molecules prior to exposure to the gradient might encode the prior information. We expect that growth cones newly introduced to the gradient will have a uniform distribution of signalling molecules that represents a flat prior, while growth cones that have been exposed to a gradient for a long time will have a localised distribution. 'Primed' growth cones will be more responsive to gradients in the same direction of their initial bias but less responsive to gradients in the opposite directions. These hypotheses will be interesting to test in the future.

The model in chapter 6 is built based on the assumption that growth cone movement depends on three factors: persistence, bias and noise. The model derives some aspects from empirical data such as step sizes being independent on the gradient and distribution of turning angles. Without any direct measurement of anchor points, the model makes the minimalist assumption that there is only one stationary anchor point and can match the data well. The noise term can come from measurement noise from stochastic ligand-receptor binding and randomness in the actin polymerisation process. However, the source of this noise term is still not clear.

This work highlights the importance of tension in growth cone trajectories. The growth cone's behaviour is slightly counter-intuitive. It is being pulled by tension from the axon but it is this tension that stimulates growth and elongation through some little understood mechanosensing mechanism. Some progress has been made in revealing the mechanisms underlying this process [286]. Through the coupling with the substrate, the retrograde flow of actin within the growth cone drives its movement forward. Thus, the growth cone's movement depends critically on the physical properties of adhesion on the substrate. Future work should investigate the role of adhesion to substrate in axon guidance in more detail and suggestions will be described in the section 3.3.

Adhesion sites provide the coupling between the extracellular matrix and the intracellular actin cytoskeleton. Two broad categories of adhesion sites are "focal complexes" associated with lamellipodia and filopodia that support protrusion and traction and "focal adhesions" that provide more stable and longer term anchorage [267]. Smaller contact points or focal complexes that provide short term attachment to the substrate are highly dynamic leading to the motile movements of the growth cone. We hypothesise that anchor points are focal adhesions, or stable adhesion contacts made up of integrin clusters and macromolecular complexes. On a laminin substrate such as the one used in our experimental set up, such focal adhesions appeared to be rare as visually, the axon was only attached to the substrate at very few points. Methods to visualise the anchor points in moving axons would be very useful to characterise this dynamics in more detail. Existing methods relying on imaging focal adhesion kinases that are present in adhesion complexes have provided important insights on the dynamics of such contact points and their role in growth cone motility [279]. However, our study indicates that imaging focal adhesions along the axon can also be critical to gain a more complete picture.

The model also predicts that with more anchor points and high motility noise, the trajectories will have less persistence to grow straight and can curve back on themselves. However, this phenomenon is rarely observed *in vivo*, suggesting that motility noise *in vivo* is small. *In vivo* growth cones often follow stereotypical well-defined paths that can sometimes include drastic turns, for example retinotectal projections in the zebrafish [287] or commissural growth cones crossing the midline [288]. It is still unclear why *in vitro* turning is so different from *in vivo*, but other factors such as physical barriers, cell cell interactions and the highly complex ECM environment might be at play. Through expression of cell surface adhesion molecules and release short and long-range signal cues, cell-cell interactions can serve as intermediate guideposts in axon guidance and scaffolds for growth [289]. Adhesion molecules in the ECM might either provide guidance directly or cooperate with diffusible guidance cues to achieve more accurate guidance. Such possibilities are discussed in the next section.

Our work gives some insight for researchers in this field because it provides a detailed analysis of guided trajectories that has been lacking. Traditionally, guidance data is provided in a binary manner (turning left/right) however, the detailed statistics were lacking. It stimulates new thinking about the critical role of adhesion points and how to manipulate them to regulate guidance.

7.3 Future directions

7.3.1 Combination of multiple cues

A striking feature of axon guidance is the vast repertoire of guidance signals due to the combinations of ligand molecules, receptors, and downstream signalling pathways. Growth cones navigating in the developing embryo are likely to be exposed to and integrate multiple guidance cues along their paths. The use of multiple signalling systems gives more flexibility in regulating guidance responses to a limited number of guidance cues, possibly increases the chemotactic accuracy and reduces noise. The rules by which growth cones respond to multiple factors are still unknown.

Dudanova and Klein [290] classify interactions between guidance cues into two types. First, different cues might act independently. For example, Ret and EphA4 receptors binding with glial-cell-derived neurotrophic factor and EphirinAs ligands act independently in motor axon projection to the vertebrate hindlimb [204]. Second, two types of receptors might interact in a non-additive manner due to crosstalk between signalling pathways, by suppressing or enhancing each other [290]. One of the best-known examples of the complex interaction between multiple guidance cues is in axonal growth cones that cross the nervous system midline and change their responsiveness to Slit and Netrin. Slit acts primarily as a chemorepellent while Netrin can act as an attractant or repellent depending on the cellular context. DCC and UNC-5 receptors bind to netrins and Robo receptors bind to Slit. Growth cones that have crossed the midline become repelled by the Slit and simultaneously lose attraction to netrin. Activation of the Slit receptor Roundabout (Robo) silences the attractive effect of netrin-1 through the formation of a Robo/DCC receptor complex [291].

As *in vivo* studies have been difficult, *in vitro* assays will prove greatly helpful by creating precisely controlled microenvironments to observe cell response to different combinations of guidance cues. Cao and Shoichet [292] found a synergistic effect between NT-3 and NGF in chick DRG neurons at E9 by observing that a significantly shallower gradient was required to guide axonal growth cones. However, they did not find any synergistic effect between NGF and BDNF. Furthermore, spinal neurons were guided by a concentration gradient of NT-3 in the presence of NGF but not by a gradient of BDNF in the presence of NGF [293]. The authors hypothesized that BDNF and NGF share common cytosolic signalling paths while NT-3 and NGF use two separate pathways for guidance. The gradients in this paper took a long time to develop (30-36h) while the DRGs extended axons within 12 hours. The assay was thus limited to observing long term effects.

The combinatorial effect has been poorly examined *in vitro*, due to the lack of appropriate experimental assays. Compared to classical cell culture methods, microfluidic devices allow much more refined spatial and temporal control over the guidance cue profiles and are ideal for studying combinations of guidance cues. Few experiments have been done to investigate this phenomenon but they have given interesting results. When the growth cone is presented with opposing gradients of BDNF and substrate-bound laminin, the polarity of guidance response of a growth can be modulated by manipulating the mean concentration of a BDNF gradient [203]. Sloan *et al.* [259] discovered that commissural axons exhibited higher sensitivity to the guidance cues when exposed to combined Shh and Netrin-1 gradients compared to each alone and can turn in response to shallower gradients that were individually unable to guide axons. This might be useful as growth cones can be guided by shallow gradients in the spinal cord where the steepness of a single cue is insufficient.

New patterning techniques such as double-cue stripe assays have contributed to a deeper understanding of the retino-tectal topographic map. Using novel double-cue (receptor/ligand) stripe substrates, Gebhardt *et al.* shows that proper topographic guidance requires both fiber-target and fiber-fiber chemospecificity in nasal-temporal axons growing in a tectum where both the axons and the target tissues express gradients of both ligands and receptors [294]. Future microfluidics assays will be useful in investigating these interactions in further detail.

7.3.2 Substrate and turning

This thesis has revealed the critical role of adhesion to the substrate on axon trajectories. It is well known that adhesion to the substrate can influence cell movements [168]. This tethering of actin filaments to the adhesive sites, hence the substrate, counteracts the retrograde flow of actin. Myosin II motors in the actin network exert tension that pulls the growth cone forward. A major player in this process is the integrin receptors. In addition to providing force transmission to the ECM, integrin-mediated adhesions are also believed to be important for mechanosensing. Integrin engagement initiates the assembly of macromolecular complexes consisting of clustered integrins, adaptor proteins and other signalling molecules that link to the cytoskeleton. The nature of these adhesion points differ on different substrate. On laminin, point contacts are highly dynamic, leading to motile and rapidly extending growth cones. On fibronectin, there are fewer contacts on the growth cone but they are more stable, leading to reduced motility [279].

Our study also only investigated one particular cell type on a laminin plastic substrate, and there are likely differences in other systems. The recent study [34] on the different response of PNS and CNS neurons on different substrates indicates that the microfluidic environment might be very different from the natural environment and a softer, more realistic substrate is to be desired. Growing neurons on glial cells might be a more realistic environment although it will require a different labelling technique such as fluorescent labelling. Similar detailed analysis should be done in other cell types (PNS versus CNS) on different substrates (soft and hard) patterned with different molecules (laminin, fibronectin, poly-lysine) to identify whether the model can predict their trajectories.

By testing different cell types on different substrate stiffness and ECM components, we can have a clearer picture of the role of ECM. Novel technologies that permit an integrative approach allowing controlling of stiffness, protein patterning and soluble gradients will be of great interest in the future. The substrate stiffness can be controlled by adjusting the crosslinker concentration in a polymer, for example polyacrylamide [295]. The rate of neurite extension was inversely correlated to the mechanical stiffness of agarose gels [295]. A recent paper investigated the complex interactions between the ECM and molecular gradients on neurite guidance [296]. In this work, neurite outgrowth is modelled by a partial different equation whose parameters are the guidance molecule concentration and diffusion constant in the collagen gel. They experimentally demonstrated that outgrowth and turning were influenced by the physical properties (composition and stiffness) of the 3D ECM scaffold in a microfluidic device. This will help achieve a more complete understanding of growth cone behaviour in response to mechanical and biochemical stimuli.

7.4 Conclusion

In conclusion, the positioning and diffusion of receptors on neuronal growth cones can have substantial effect on the quality of spatial gradient sensing. We have introduced a theoretical model of how growth cones move in attractive and repulsive gradients to match experimental data. It provides a unifying explanation for weak turning *in vitro* and suggests other conditions that must exist *in vivo* for reliable turning to occur. The interaction of diffusible gradient and substrate properties will be an exciting direction to pursue in the future.

Bibliography

[1] M. Tessier-Lavigne and C. S. Goodman, “The molecular biology of axon guidance.,” *Science*, vol. 274, pp. 1123–1133, 1996.

[2] B. J. Dickson, “Molecular mechanisms of axon guidance.,” *Science*, vol. 298, pp. 1959–1964, 2002.

[3] J. K. Chilton, “Molecular mechanisms of axon guidance,” *Developmental Biology*, vol. 292, pp. 13–24, 2006.

[4] A. Bagorda and C. A. Parent, “Eukaryotic chemotaxis at a glance.,” *Journal of Cell Science*, vol. 121, no. 16, pp. 2621–2624, 2008.

[5] D. Mortimer, T. Fothergill, Z. Pujic, L. J. Richards, and G. J. Goodhill, “Growth cone chemotaxis,” *Trends in Neurosciences*, vol. 31, pp. 90–98, 2008.

[6] K. F. Swaney, C.-H. Huang, and P. N. Devreotes, “Eukaryotic chemotaxis: a network of signaling pathways controls motility, directional sensing, and polarity,” *Annual Review of Biophysics*, vol. 39, pp. 265–289, 2010.

[7] R. H. Insall, “Understanding eukaryotic chemotaxis: a pseudopod-centred view.,” *Nature Reviews. Molecular Cell Biology*, vol. 11, no. 6, pp. 453–458, 2010.

[8] E. C. Engle, “Human genetic disorders of axon guidance.,” *Cold Spring Harbor Perspectives in Biology*, vol. 2, no. 3, pp. 1–18, 2010.

[9] A. A. Nugent, A. L. Kolpak, and E. C. Engle, “Human disorders of axon guidance.,” *Current Opinion in Neurobiology*, vol. 22, no. 5, pp. 837–43, 2012.

[10] A. Yaron and B. Zheng, “Navigating their way to the clinic: Emerging roles for axon guidance molecules in neurological disorders and injury,” *Developmental Neurobiology*, vol. 67, pp. 1216–1231, 2007.

[11] D. M. Maraganore, M. de Andrade, T. G. Lesnick, K. J. Strain, M. J. Farrer, W. A. Rocca, P. V. K. Pant, K. A. Frazer, D. R. Cox, and D. G. Ballinger, “High-resolution whole-genome association study of Parkinson disease,” *American Journal of Human Genetics*, vol. 77, no. 5, pp. 685–693, 2005.

[12] S. Suda, K. Iwata, C. Shimmura, Y. Kameno, A. Anitha, I. Thanseem, K. Nakamura, H. Matsuzaki, K. J. Tsuchiya, G. Sugihara, Y. Iwata, K. Suzuki, K. Koizumi, H. Higashida, N. Takei, and N. Mori, “Decreased expression of axon-guidance receptors in the anterior cingulate cortex in autism,” *Molecular Autism*, vol. 2, no. 1, p. 14, 2011.

[13] K. Hannula-Jouppi, N. Kaminen-Ahola, M. Taipale, R. Eklund, J. Nopola-Hemmi, H. Kääriäinen, and J. Kere, “The axon guidance receptor gene ROBO1 is a candidate gene for developmental dyslexia,” *PLoS Genetics*, vol. 1, no. 4, pp. 0467–0474, 2005.

[14] G. P. Downey, “Mechanisms of leukocyte motility and chemotaxis.,” *Current Opinion in Immunology*, vol. 6, no. 1, pp. 113–24, 1994.

[15] P. A. Iglesias and P. N. Devreotes, “Navigating through models of chemotaxis.,” *Current Opinion in Cell Biology*, vol. 20, no. 1, pp. 35–40, 2008.

[16] A. von Philipsborn and M. Bastmeyer, “Mechanisms of gradient detection: a comparison of axon pathfinding with eukaryotic cell migration.,” *International Review of Cytology*, vol. 263, no. 07, pp. 1–62, 2007.

[17] M. Ueda, Y. Sako, T. Tanaka, P. Devreotes, and T. Yanagida, “Single-molecule analysis of chemotactic signaling in Dictyostelium cells.,” *Science*, vol. 294, no. 5543, pp. 864–867, 2001.

[18] P. A. Iglesias and A. Levchenko, “Modeling the cell’s guidance system.,” *Science Signaling*, vol. 2002, no. 148, p. re12, 2002.

[19] A. Levchenko and P. A. Iglesias, “Models of eukaryotic gradient sensing: application to chemotaxis of amoebae and neutrophils.,” *Biophysical Journal*, vol. 82, no. January, pp. 50–63, 2002.

[20] A. Samadani, J. Mettetal, and A. van Oudenaarden, “Cellular asymmetry and individuality in directional sensing.,” *Proceedings of the National Academy of Sciences of the United States of America*, vol. 103, no. 31, pp. 11549–54, 2006.

[21] P. A. Iglesias, “Chemoattractant signaling in dictyostelium: adaptation and amplification,” *Science Signaling*, vol. 5, no. 213, p. pe8, 2012.

[22] G. J. Goodhill, “Contributions of theoretical modeling to the understanding of neural map development.,” *Neuron*, vol. 56, no. 2, pp. 301–311, 2007.

[23] P. Gordon-Weeks, *Neuronal Growth Cones.* Cambridge University Press, 2005.

[24] C. Speidel, “Motion Pictures Made of Growing Nerve Fibers,” *Science News-Letter*, vol. 23, no. 615, p. 43, 1933.

[25] P. Weiss, “Nerve patterns : the mechanics of nerve growth,” *Growth*, vol. 5, pp. 163–203, 1941.

[26] R. Sperry, “Chemoaffinity in the orderly growth of nerve fiber patterns and connections,” *Proceedings of the National Academy of Sciences of the United States of America*, vol. 50, no. 4, pp. 703–710, 1963.

[27] A. G. Lumsden and A. M. Davies, “Chemotropic effect of specific target epithelium in the developing mammalian nervous system,” *Nature*, vol. 323, no. 6088, pp. 538–9, 1986.

[28] M. Tessier-Lavigne, M. Placzek, A. G. Lumsden, J. Dodd, and T. M. Jessell, “Chemotropic guidance of developing axons in the mammalian central nervous system,” *Nature*, vol. 336, no. 6201, pp. 775–778, 1988.

[29] T. E. Kennedy, T. Serafini, J. R. de la Torre, and M. Tessier-Lavigne, “Netrins are diffusible chemotropic factors for commissural axons in the embryonic spinal cord,” *Cell*, vol. 78, no. 3, pp. 425–435, 1994.

[30] L. A. Lowery and D. Van Vactor, “The trip of the tip: understanding the growth cone machinery,” *Nature Reviews. Molecular Cell Biology*, vol. 10, pp. 332–343, 2009.

[31] K. Kalil, L. Li, and B. I. Hutchins, “Signaling Mechanisms in Cortical Axon Growth, Guidance, and Branching,” *Frontiers in Neuroanatomy*, vol. 5, 2011.

[32] T. M. Gomez and P. C. Letourneau, “Actin dynamics in growth cone motility and navigation,” *Journal of Neurochemistry*, vol. 129, no. 2, pp. 221–234, 2014.

[33] D. M. Suter and P. Forscher, “Substrate-cytoskeletal coupling as a mechanism for the regulation of growth cone motility and guidance,” *Journal of Neurobiology*, vol. 44, no. 2, pp. 97–113, 2000.

[34] D. Koch, W. J. Rosoff, J. Jiang, H. M. Geller, and J. S. Urbach, “Strength in the periphery: Growth cone biomechanics and substrate rigidity response in peripheral and central nervous system neurons,” *Biophysical Journal*, vol. 102, no. 3, pp. 452–460, 2012.

[35] M. Vassali, M. Basso, and F. Difato, “Measurement of tension release during laser induced axon lesion to evaluate axonal adhesion to the substrate at piconewton and millisecond resolution,” *Journal of Visualized Experiments*, vol. 75, p. 50477, 2013.

[36] T. J. Dennerll, P. Lamoureux, R. E. Buxbaum, and S. R. Heidemann, “The cytomechanics of axonal elongation and retraction,” *Journal of Cell Biology*, vol. 109, no. 6 I, pp. 3073–3083, 1989.

[37] M. O’Toole, P. Lamoureux, and K. E. Miller, “A physical model of axonal elongation: force, viscosity, and adhesions govern the mode of outgrowth,” *Biophysical Journal*, vol. 94, no. 7, pp. 2610–20, 2008.

[38] M. Aeschlimann, *Biophysical models of axonal pathfinding.* Phd thesis, University of Lausanne, 2000.

[39] A. Chédotal and L. J. Richards, “Wiring the brain: the biology of neuronal guidance.,” *Cold Spring Harbor Perspectives in Biology*, vol. 2, no. 6, pp. 1–17, 2010.

[40] D. G. Wilkinson, “Topographic mapping: Organising by repulsion and competition?,” *Current Biology*, vol. 10, no. 12, pp. 447–451, 2000.

[41] F. S. Walsh and P. Doherty, “Neural cell adhesion molecules of the immunoglobulin superfamily: role in axon growth and guidance.,” *Annual Review of Cell and Developmental Biology*, vol. 13, pp. 425–456, 1997.

[42] V. Hamburger and R. Levi-Montalcini, "Proliferation, differentiation and generation in the spinal ganglia of the chick embryo under normal and experimental conditions," *Journal of Experimental Zoology*, vol. 111, no. 3, pp. 457–501, 1949.

[43] R. Levi-Montalcini and P. Angeletti, "Growth control of the sympathetic system by a specific protein factor," *Quarterly Review of Biology*, vol. 36, no. 2, pp. 99–108, 1961.

[44] R. Levi-Montalcini and P. U. Anceletti, "Essential Survival Role of the Nerve and Maintenance Growth Factor in the of Dissociated Embryonic Sensory and Sympathetic Nerve Cells in Vitro1," *Developmental Biology*, vol. 7, pp. 653–659, 1963.

[45] S. Guthrie, "Neurotrophic factors: are they axon guidance molecules?," in *Advances in Experimental Medicine and Biology*, vol. 621, pp. 81–94, 2007.

[46] P. C. Letourneau, "Chemotactic response of nerve fiber elongation to nerve growth factor.," *Developmental Biology*, vol. 66, pp. 183–196, 1978.

[47] G. J. Bashaw and R. Klein, "Signaling from axon guidance receptors.," *Cold Spring Harbor Perspectives in Biology*, vol. 2, no. 5, p. 1941, 2010.

[48] A. Hall and G. Lalli, "Rho and Ras GTPases in axon growth, guidance, and branching.," *Cold Spring Harbor Perspectives in Biology*, vol. 2, no. 2, pp. 1–18, 2010.

[49] A. Jilkine, *Mathematical study of Rho GTPases in motile cells.* Master thesis, University of British Columbia, 2005.

[50] A. Jilkine, A. F. M. Marée, and L. Edelstein-Keshet, "Mathematical model for spatial segregation of the Rho-family GTPases based on inhibitory crosstalk.," *Bulletin of Mathematical Biology*, vol. 69, no. 6, pp. 1943–78, 2007.

[51] M. Otsuji, S. Ishihara, C. Co, K. Kaibuchi, A. Mochizuki, and S. Kuroda, "A mass conserved reaction-diffusion system captures properties of cell polarity," *PLoS Computational Biology*, vol. 3, no. 6, pp. 1040–1054, 2007.

[52] D. J. Sutherland, Z. Pujic, and G. J. Goodhill, "Calcium signaling in axon guidance," *Trends in Neurosciences*, vol. 37, no. 8, pp. 424–432, 2014.

[53] K. L. Lankford and P. C. Letourneau, “Evidence that calcium may control neurite outgrowth by regulating the stability of actin filaments,” *Journal of Cell Biology*, vol. 109, no. 3, pp. 1229–1243, 1989.

[54] R. D. Fields, E. A. Neale, and P. G. Nelson, “Effects of patterned electrical activity on neurite outgrowth from mouse sensory neurons.,” *Journal of Neuroscience*, vol. 10, no. 9, pp. 2950–2964, 1990.

[55] C. E. Bandtlow, M. F. Schmidt, T. D. Hassinger, M. E. Schwab, and S. B. Kater, “Role of intracellular calcium in NI-35-evoked collapse of neuronal growth cones.,” *Science*, vol. 259, no. 5091, pp. 80–83, 1993.

[56] M. Catsicas, S. Allcorn, and P. Mobbs, “Early activation of Ca2+-permeable AMPA receptors reduces neurite outgrowth in embryonic chick retinal neurons,” *Journal of Neurobiology*, vol. 49, no. 3, pp. 200–211, 2001.

[57] F. Tang, E. W. Dent, and K. Kalil, “Spontaneous calcium transients in developing cortical neurons regulate axon outgrowth.,” *Journal of Neuroscience*, vol. 23, no. 3, pp. 927–936, 2003.

[58] M. P. Mattson and S. B. Kater, “Calcium regulation of neurite elongation and growth cone motility.,” *Journal of Neuroscience*, vol. 7, no. 12, pp. 4034–43, 1987.

[59] T. M. Gomez and N. C. Spitzer, “In vivo regulation of axon extension and pathfinding by growth-cone calcium transients.,” *Nature*, vol. 397, no. 6717, pp. 350–355, 1999.

[60] K. Hong, M. Nishiyama, J. Henley, M. Tessier-Lavigne, and M. Poo, “Calcium signalling in the guidance of nerve growth by netrin-1,” *Nature*, vol. 403, no. 6765, pp. 93–98, 2000.

[61] E. M. Forbes, A. W. Thompson, J. Yuan, and G. J. Goodhill, “Calcium and cAMP Levels Interact to Determine Attraction versus Repulsion in Axon Guidance,” *Neuron*, vol. 74, pp. 490–503, 2012.

[62] T. M. Gomez and J. Q. Zheng, “The molecular basis for calcium-dependent axon pathfinding.,” *Nature Reviews. Neuroscience*, vol. 7, no. 2, pp. 115–25, 2006.

[63] J. Q. Zheng, M. M. Poo, and J. A. Connor, “Calcium and chemotropic turning of nerve growth cones,” *Perspectives on Developmental Neurobiology*, vol. 4, no. 2-3, pp. 205–213, 1996.

[64] T. M. Gomez, D. M. Snow, and P. C. Letourneau, “Characterization of spontaneous calcium transients in nerve growth cones and their effect on growth cone migration,” *Neuron*, vol. 14, no. 6, pp. 1233–1246, 1995.

[65] T. M. Gomez, E. Robles, M. Poo, and N. C. Spitzer, “Filopodial calcium transients promote substrate-dependent growth cone turning.,” *Science*, vol. 291, no. 5510, pp. 1983–1987, 2001.

[66] Y. Li, Y.-C. Jia, K. Cui, N. Li, Z.-Y. Zheng, Y.-Z. Wang, and X.-B. Yuan, “Essential role of TRPC channels in the guidance of nerve growth cones by brain-derived neurotrophic factor.,” *Nature*, vol. 434, no. 7035, pp. 894–898, 2005.

[67] G. X. Wang and M.-M. Poo, “Requirement of TRPC channels in netrin-1-induced chemotropic turning of nerve growth cones.,” *Nature*, vol. 434, no. 7035, pp. 898–904, 2005.

[68] M. J. Berridge, M. D. Bootman, and H. L. Roderick, “Calcium signalling: dynamics, homeostasis and remodelling.,” *Nature Reviews. Molecular Cell Biology*, vol. 4, no. 7, pp. 517–29, 2003.

[69] T. Tojima, J. H. Hines, J. R. Henley, and H. Kamiguchi, “Second messengers and membrane trafficking direct and organize growth cone steering.,” *Nature Reviews. Neuroscience*, vol. 12, no. 4, pp. 191–203, 2011.

[70] M. J. Berridge and R. F. Irvine, “Inositol trisphosphate, a novel second messenger in cellular signal transduction.,” *Nature*, vol. 312, no. 5992, pp. 315–21, 1984.

[71] M. Endo, M. Tanaka, and Y. Ogawa, “Calcium induced release of calcium from the sarcoplasmic reticulum of skinned skeletal muscle fibres,” *Nature*, vol. 228, pp. 34–36, 1970.

[72] T. Tojima, R. Itofusa, and H. Kamiguchi, “The nitric oxide-cGMP pathway controls the directional polarity of growth cone guidance via modulating cytosolic Ca2+ signals.,” *Journal of Neuroscience*, vol. 29, no. 24, pp. 7886–97, 2009.

[73] T. Tojima, R. Itofusa, and H. Kamiguchi, "Steering neuronal growth cones by shifting the imbalance between exocytosis and endocytosis.," *Journal of Neuroscience*, vol. 34, no. 21, pp. 7165–78, 2014.

[74] G. C. Faas, S. Raghavachari, J. E. Lisman, and I. Mody, "Calmodulin as a direct detector of Ca2+ signals.," *Nature Neuroscience*, vol. 14, no. 3, pp. 301–4, 2011.

[75] Z. Wen, C. Guirland, G. L. Ming, and J. Q. Zheng, "A CaMKII/calcineurin switch controls the direction of Ca(2+)-dependent growth cone guidance.," *Neuron*, vol. 43, no. 6, pp. 835–46, 2004.

[76] T. Ishikawa, J. R. Hume, and K. D. Keef, "Regulation of Ca2+ channels by cAMP and cGMP in vascular smooth muscle cells," *Circulation Research*, vol. 73, no. 6, pp. 1128–1137, 1993.

[77] K. Taguchi, M. Ueda, and T. Kubo, "Effects of cAMP and cGMP on L-type calcium channel currents in rat mesenteric artery cells.," *Japanese Journal of Pharmacology*, vol. 74, no. 2, pp. 179–86, 1997.

[78] A. M. Lohof, M. Quillan, Y. Dan, and M. M. Poo, "Asymmetric modulation of cytosolic cAMP activity induces growth cone turning.," *Journal of Neuroscience*, vol. 12, pp. 1253–1261, 1992.

[79] G. L. Ming, H. J. Song, B. Berninger, C. E. Holt, M. Tessier-Lavigne, and M. M. Poo, "cAMP-dependent growth cone guidance by netrin-1," *Neuron*, vol. 19, no. 6, pp. 1225–1235, 1997.

[80] H. J. Song, G. L. Ming, and M. M. Poo, "cAMP-induced switching in turning direction of nerve growth cones.," *Nature*, vol. 388, pp. 275–279, 1997.

[81] H. Song, G. Ming, Z. He, M. Lehmann, L. McKerracher, M. Tessier-Lavigne, and M. Poo, "Conversion of neuronal growth cone responses from repulsion to attraction by cyclic nucleotides.," *Science*, vol. 281, no. 5382, pp. 1515–1518, 1998.

[82] D. J. Sutherland and G. J. Goodhill, "The interdependent roles of Ca2+ and cAMP in axon guidance," *Developmental Neurobiology*, pp. 402–410, 2013.

[83] T. Tojima, R. Itofusa, and H. Kamiguchi, "Asymmetric clathrin-mediated endocytosis drives repulsive growth cone guidance," *Neuron*, vol. 66, no. 3, pp. 370–377, 2010.

[84] B. J. Dickson, "Rho GTPases in growth cone guidance," *Current Opinion in Neurobiology*, vol. 11, no. 1, pp. 103–110, 2001.

[85] K.-M. Leung, F. P. G. van Horck, A. C. Lin, R. Allison, N. Standart, and C. E. Holt, "Asymmetrical beta-actin mRNA translation in growth cones mediates attractive turning to netrin-1.," *Nature Neuroscience*, vol. 9, no. 10, pp. 1247–56, 2006.

[86] T. Shigeoka, B. Lu, and C. E. Holt, "Cell biology in neuroscience: RNA-based mechanisms underlying axon guidance.," *Journal of Cell Biology*, vol. 202, no. 7, pp. 991–9, 2013.

[87] D. S. Campbell and C. E. Holt, "Chemotropic responses of retinal growth cones mediated by rapid local protein synthesis and degradation," *Neuron*, vol. 32, no. 6, pp. 1013–1026, 2001.

[88] M. Piper, R. Anderson, A. Dwivedy, C. Weinl, F. Van Horck, K. M. Leung, E. Cogill, and C. Holt, "Signaling mechanisms underlying Slit2-induced collapse of Xenopus retinal growth cones," *Neuron*, vol. 49, no. 2, pp. 215–228, 2006.

[89] S. M. Kay, *Fundamentals of Statistical Signal Processing*, vol. Volume I. Prentice Hall, 1993.

[90] H. V. Poor, *An introduction to signal detection and estimation.* Springer, 1994.

[91] D. C. Knill and A. Pouget, "The Bayesian brain: The role of uncertainty in neural coding and computation," *Trends in Neurosciences*, vol. 27, no. 12, pp. 712–719, 2004.

[92] M. Colombo and P. Series, "Bayes in the Brain–On Bayesian Modelling in Neuroscience," *British Journal for the Philosophy of Science*, vol. 63, pp. 697–723, 2012.

[93] J. X. O'Reilly, S. Jbabdi, and T. E. J. Behrens, "How can a Bayesian approach inform neuroscience?," *European Journal of Neuroscience*, vol. 35, no. 7, pp. 1169–1179, 2012.

[94] D. Kersten, P. Mamassian, and A. Yuille, "Object perception as Bayesian inference.," *Annual Review of Psychology*, vol. 55, pp. 271–304, 2004.

[95] D. Mortimer, J. Feldner, T. Vaughan, I. Vetter, Z. Pujic, W. J. Rosoff, K. Burrage, P. Dayan, L. J. Richards, and G. J. Goodhill, "Bayesian model predicts the response of axons to molecular gradients.," *Proceedings of the National Academy of Sciences of the United States of America*, vol. 106, no. 25, pp. 10296–10301, 2009.

[96] B. Hu, W. Chen, W. J. Rappel, and H. Levine, "Physical limits on cellular sensing of spatial gradients," *Physical Review Letters*, vol. 105, pp. 1–4, 2010.

[97] B. Hu, W. Chen, H. Levine, and W.-J. Rappel, "Quantifying information transmission in eukaryotic gradient sensing and chemotactic response.," *Journal of Statistical Physics*, vol. 142, no. 6, pp. 1167–1186, 2011.

[98] B. Hu, W. Chen, W.-j. Rappel, and H. Levine, "How geometry and internal bias affect the accuracy of eukaryotic gradient sensing," *Physical Review E*, vol. 83, pp. 0219171–9, 2011.

[99] A. Baba, T. Hiraiwa, and T. Shibata, "Directional sensing of deformed cells under faint gradients," *Physics Review E*, vol. 86, no. 6, p. 60901, 2012.

[100] T. J. Diefenbach, P. B. Guthrie, and S. B. Kater, "Stimulus History Alters Behavioral Responses of Neuronal Growth Cones," *Journal of Neuroscience*, vol. 20, no. 4, pp. 1484–1494, 2000.

[101] C. A. Mason and L. C. Wang, "Growth cone form is behavior-specific and, consequently, position-specific along the retinal axon pathway.," *Journal of Neuroscience*, vol. 17, no. 3, pp. 1086–100, 1997.

[102] P. Devreotes and C. Janetopoulos, "Eukaryotic chemotaxis: distinctions between directional sensing and polarization.," *Journal of Biological Chemistry*, vol. 278, no. 23, pp. 20445–8, 2003.

[103] F. Wang, "The signaling mechanisms underlying cell polarity and chemotaxis.," *Cold Spring Harbor Perspectives in Biology*, vol. 1, no. 4, pp. 1–16, 2009.

[104] M. J. Wang, Y. Artemenko, W. J. Cai, P. A. Iglesias, and P. N. Devreotes, "The Directional Response of Chemotactic Cells Depends on a Balance between Cytoskeletal Architecture and the External Gradient," *Cell Reports*, vol. 9, no. 3, pp. 1110–1121, 2014.

[105] A. Kusumi, C. Nakada, K. Ritchie, K. Murase, K. Suzuki, H. Murakoshi, R. S. Kasai, J. Kondo, and T. Fujiwara, "Paradigm shift of the plasma membrane concept from the two-dimensional continuum fluid to the partitioned fluid: high-speed single-molecule tracking of membrane molecules.," *Annual Review of Biophysics and Biomolecular Structure*, vol. 34, pp. 351–378, 2005.

[106] A. Einstein, "Investigations on the Theory of the Brownian Movement," *Annalen der Physik*, vol. 17, p. 549, 1905.

[107] K. Przibram, "Über die ungeordnete Bewegung niederer Tiere," *Pflüger's Archiv für die gesamte Physiologie*, vol. 153, p. 401, 1913.

[108] R. Furth, "Einige Untersuchungen über Brownsche Bewegung an einem Einzelteilchen," *Annalen der Physik*, vol. 53, p. 177, 1917.

[109] C. S. Patlak, "Random walk with persistence and external bias," *Bulletin of Mathematical Biophysics*, vol. 15, pp. 311–338, 1953.

[110] M. H. Gail and C. W. Boone, "The locomotion of mouse fibroblasts in tissue culture.," *Biophysical Journal*, vol. 10, pp. 980–993, 1970.

[111] R. L. Hall, "Amoeboid movement as a correlated walk.," *Journal of Mathematical Biology*, vol. 4, pp. 327–335, 1977.

[112] D. S. Johnson, D. S. Johnson, J. M. London, J. M. London, M.-A. Lea, M.-A. Lea, J. W. Durban, and J. W. Durban, "Continuous-time correlated random walk model for animal telemetry data.," *Ecology*, vol. 89, pp. 1208–15, 2008.

[113] D. W. Sims, E. J. Southall, N. E. Humphries, G. C. Hays, C. J. a. Bradshaw, J. W. Pitchford, A. James, M. Z. Ahmed, A. S. Brierley, M. a. Hindell, D. Morritt, M. K. Musyl, D. Righton, E. L. C. Shepard, V. J. Wearmouth, R. P. Wilson, M. J. Witt, and J. D. Metcalfe, "Scaling laws of marine predator search behaviour.," *Nature*, vol. 451, pp. 1098–1102, 2008.

[114] L. Li, S. F. Nø rrelkke, and E. C. Cox, "Persistent cell motion in the absence of external signals: A search strategy for eukaryotic cells," *PLoS ONE*, vol. 3, 2008.

[115] N. A. Hill and D. P. Hader, “A biased random walk model for the trajectories of swimming micro-organisms.,” *Journal of Theoretical Biology*, vol. 186, pp. 503–526, 1997.

[116] W. Alt, “Biased random walk models for chemotaxis and related diffusion approximations.,” *Journal of Mathematical Biology*, vol. 9, pp. 147–177, 1980.

[117] P. J. M. van Haastert and M. Postma, “Biased random walk by stochastic fluctuations of chemoattractant-receptor interactions at the lower limit of detection.,” *Biophysical Journal*, vol. 93, pp. 1787–1796, 2007.

[118] P. S. Lovely and F. W. Dahlquist, “Statistical measures of bacterial motility and chemotaxis.,” *Journal of Theoretical Biology*, vol. 50, pp. 477–496, 1975.

[119] H. C. Berg and D. A. Brown, “Chemotaxis in Escherichia coli analysed by three-dimensional tracking.,” *Nature*, vol. 239, pp. 500–504, 1972.

[120] R. Nossal and S. H. Zigmond, “Chemotropism indices for poly-morphonuclear leukocytes,” *Biophysical Journal*, vol. 16, no. 1923, pp. 1171–82, 1976.

[121] M. J. Katz, E. B. George, and L. J. Gilbert, “Axonal elongation as a stochastic walk.,” *Cell Motility*, vol. 4, pp. 351–370, 1984.

[122] M. J. Katz, “How straight do axons grow?,” *Journal of Neuroscience*, vol. 5, no. 3, pp. 589–595, 1985.

[123] Y. E. Pearson, E. Castronovo, T. A. Lindsley, and D. A. Drew, “Mathematical Modeling of Axonal Formation Part I: Geometry,” *Bulletin of Mathematical Biology*, vol. 73, pp. 2837–2864, 2011.

[124] S. M. Maskery, H. M. Buettner, and T. Shinbrot, “Growth cone pathfinding: a competition between deterministic and stochastic events.,” *BMC Neuroscience*, vol. 5, p. 22, 2004.

[125] D. J. Odde and H. M. Buettner, “Time series characterization of simulated microtubule dynamics in the nerve growth cone,” *Annals of Biomedical Engineering*, vol. 23, pp. 268–286, 1995.

[126] R. Borisyuk, T. Cooke, and A. Roberts, "Stochasticity and functionality of neural systems: mathematical modelling of axon growth in the spinal cord of tadpole.," *BioSystems*, vol. 93, no. 1-2, pp. 101–14, 2008.

[127] A. Gierer, "Model for the retino-tectal projection.," *Proceedings of the Royal Society of London. Series B, Biological Sciences*, vol. 218, no. 1210, pp. 77–93, 1983.

[128] H. M. Buettner, "Nerve growth dynamics. Quantitative models for nerve development and regeneration.," *Annals of the New York Academy of Sciences*, vol. 745, pp. 210–221, 1994.

[129] H. M. Buettner, R. N. Pittman, and J. K. Ivins, "A model of neurite extension across regions of nonpermissive substrate: simulations based on experimental measurement of growth cone motility and filopodial dynamics.," *Developmental Biology*, vol. 163, pp. 407–422, 1994.

[130] D. J. Odde, E. M. Tanaka, S. S. Hawkins, and H. M. Buettner, "Stochastic dynamics of the nerve growth cone and its microtubules during neurite outgrowth.," *Biotechnology and Bioengineering*, vol. 50, no. 4, pp. 452–61, 1996.

[131] G. H. Li, C. Qin, and L. W. Wang, "Computer Model of Growth Cone Behavior and Neuronal Morphogenesis," *Journal of Theoretical Biology*, vol. 174, pp. 381–389, 1995.

[132] M. Aeschlimann and L. Tettoni, "Biophysical model of axonal pathfinding," *Neurocomputing*, vol. 2, no. 3, pp. 87–92, 2001.

[133] G. J. Goodhill, M. Gu, and J. S. Urbach, "Predicting axonal response to molecular gradients with a computational model of filopodial dynamics.," *Neural Computation*, vol. 16, no. 11, pp. 2221–43, 2004.

[134] J. Xu, W. J. Rosoff, J. S. Urbach, and G. J. Goodhill, "Adaptation is not required to explain the long-term response of axons to molecular gradients.," *Development*, vol. 132, pp. 4545–4552, 2005.

[135] T. Kobayashi, K. Terajima, M. Nozumi, M. Igarashi, and K. Akazawa, "A stochastic model of neuronal growth cone guidance regulated by multiple sensors.," *Journal of Theoretical Biology*, vol. 266, no. 4, pp. 712–22, 2010.

[136] H. G. E. Hentschel and A. van Ooyen, "Models of axon guidance and bundling during development.," *Proceedings of the Royal Society B: Biological Sciences*, vol. 266, pp. 2231–2238, 1999.

[137] J. K. Krottje and A. van Ooyen, "A mathematical framework for modeling axon guidance," *Bulletin of Mathematical Biology*, vol. 69, pp. 3–31, 2007.

[138] H. G. E. Hentschel and A. van Ooyen, "Dynamic mechanisms for bundling and guidance during neural network formation," *Physica A: Statistical Mechanics and its Applications*, vol. 288, no. 1-4, pp. 369–379, 2000.

[139] D. Mortimer, Z. Pujic, T. Vaughan, A. W. Thompson, J. Feldner, I. Vetter, and G. J. Goodhill, "Axon guidance by growth-rate modulation.," *Proceedings of the National Academy of Sciences of the United States of America*, vol. 107, pp. 5202–5207, 2010.

[140] Z. Pujic, D. Mortimer, J. Feldner, and G. J. Goodhill, "Assays for eukaryotic cell chemotaxis.," *Combinatorial Chemistry & High Throughput Screening*, vol. 12, pp. 580–588, 2009.

[141] I. Dupin, M. Dahan, and V. Studer, "Investigating axonal guidance with microdevice-based approaches.," *Journal of Neuroscience*, vol. 33, pp. 17647–55, 2013.

[142] S. Boyden, "The chemotactic effect of mixtures of antibody and antigen on polymorphonuclear leucocytes.," *Journal of Experimental Medicine*, vol. 115, pp. 453–466, 1962.

[143] S. H. Zigmond, "Ability of polymorphonuclear leukocytes to orient in gradients of chemotactic factors," *Journal of Cell Biology*, vol. 75, pp. 606–616, 1977.

[144] D. Zicha, G. A. Dunn, and A. F. Brown, "A new direct-viewing chemotaxis chamber.," *Journal of Cell Science*, vol. 99 (4), pp. 769–775, 1991.

[145] F. J. Hughes and C. A. McCulloch, "Quantification of chemotactic response of quiescent and proliferating fibroblasts in Boyden chambers by computer-assisted image analysis.," *Journal of Histochemistry and Cytochemistry*, vol. 39, no. 2, pp. 243–246, 1991.

[146] G. Pelz, A. Schettler, and H. Tschesche, "Granulocyte chemotaxis measured in a Boyden chamber assay by quantification of neutrophil elastase.," *European Journal of Clinical Chemistry and Clinical Biochemistry*, vol. 31, no. 10, pp. 651–656, 1993.

[147] W. Falk, R. H. Goodwin, and E. J. Leonard, “A 48-well micro chemotaxis assembly for rapid and accurate measurement of leukocyte migration.,” *Journal of Immunological Methods*, vol. 33, no. 3, pp. 239–247, 1980.

[148] N. S. Brown and R. Bicknell, “Cell migration and the Boyden chamber,” *Methods in Molecular Medicine*, vol. 58, pp. 47–54, 2001.

[149] L. J. Cox, U. Hengst, N. G. Gurskaya, K. A. Lukyanov, and S. R. Jaffrey, “Intra-axonal translation and retrograde trafficking of CREB promotes neuronal survival,” *Nature Cell Biology*, vol. 10, no. 2, pp. 149–159, 2008.

[150] M. Kobayashi, A. C. Wilson, M. V. Chao, and I. Mohr, “Control of viral latency in neurons by axonal mTOR signaling and the 4E-BP translation repressor,” *Genes and Development*, vol. 26, no. 14, pp. 1527–1532, 2012.

[151] H. Rubin and S. Ravid, “Polarization of myosin II heavy chain-protein kinase C in chemotaxing Dictyostelium cells,” *Journal of Biological Chemistry*, vol. 277, no. 39, pp. 36005–36008, 2002.

[152] G. Fabro, R. A. Rovasio, S. Civalero, A. Frenkel, S. R. Caplan, M. Eisenbach, and L. C. Giojalas, “Chemotaxis of capacitated rabbit spermatozoa to follicular fluid revealed by a novel directionality-based assay,” *Biology of Reproduction*, vol. 67, no. 5, pp. 1565–1571, 2002.

[153] D. M. Veltman and P. J. M. Van Haastert, “Guanylyl cyclase protein and cGMP product independently control front and back of chemotaxing Dictyostelium cells,” *Molecular Biology of the Cell*, vol. 17, no. 9, pp. 3921–3929, 2006.

[154] J. Adler, “Chemotaxis in bacteria.,” *Journal of Supramolecular Structure*, vol. 4, no. 3, pp. 305–317, 1976.

[155] R. W. Gundersen and J. N. Barrett, “Neuronal chemotaxis: chick dorsal-root axons turn toward high concentrations of nerve growth factor.,” *Science*, vol. 206, pp. 1079–1080, 1979.

[156] V. H. Höpker, D. Shewan, M. Tessier-Lavigne, M. Poo, and C. Holt, “Growth-cone attraction to netrin-1 is converted to repulsion by laminin-1.,” *Nature*, vol. 401, pp. 69–73, 1999.

[157] Y. Xiang, Y. Li, Z. Zhang, K. Cui, S. Wang, X.-B. Yuan, C.-P. Wu, M.-M. Poo, and S. Duan, "Nerve growth cone guidance mediated by G protein-coupled receptors.," *Nature Neuroscience*, vol. 5, pp. 843–848, 2002.

[158] G. C. R. Ellis-Davies, "Caged compounds: photorelease technology for control of cellular chemistry and physiology," *Nature Methods*, vol. 4, no. 8, pp. 619–628, 2007.

[159] B. Sun and D. T. Chiu, "Spatially and temporally resolved delivery of stimuli to single cells," *Journal of the American Chemical Society*, vol. 125, no. 13, pp. 3702–3703, 2003.

[160] H. Kress, J.-G. Park, C. O. Mejean, J. D. Forster, J. Park, S. S. Walse, Y. Zhang, D. Wu, O. D. Weiner, T. M. Fahmy, and E. R. Dufresne, "Cell stimulation with optically manipulated microsources," *Nature Methods*, vol. 6, no. 12, pp. 905–909, 2009.

[161] H. Akiyama, T. Matsu-ura, K. Mikoshiba, and H. Kamiguchi, "Control of neuronal growth cone navigation by asymmetric inositol 1,4,5-trisphosphate signals.," *Science Signaling*, vol. 2, no. 79, p. ra34, 2009.

[162] G. Pinato, D. Cojoc, L. T. Lien, A. Ansuini, J. Ban, E. D'Este, and V. Torre, "Less than 5 Netrin-1 molecules initiate attraction but 200 Sema3A molecules are necessary for repulsion," *Scientific Reports*, vol. 2, 2012.

[163] A. G. Lumsden and A. M. Davies, "Earliest sensory nerve fibres are guided to peripheral targets by attractants other than nerve growth factor.," *Nature*, vol. 306, no. 5945, pp. 786–788.

[164] R. Z. Kuang, M. Merline, and K. Kalil, "Topographic specificity of corticospinal connections formed in explant coculture.," *Development*, vol. 120, no. 7, pp. 1937–1947, 1994.

[165] E. K. Messersmith, E. D. Leonardo, C. J. Shatz, M. Tessier-Lavigne, C. S. Goodman, and A. L. Kolodkin, "Semaphorin III can function as a selective chemorepellent to pattern sensory projections in the spinal cord.," *Neuron*, vol. 14, no. 5, pp. 949–959, 1995.

[166] W. J. Rosoff, J. S. Urbach, M. A. Esrick, R. G. McAllister, L. J. Richards, and G. J. Goodhill, "A new chemotaxis assay shows the extreme sensitivity of axons to molecular gradients.," *Nature Neuroscience*, vol. 7, pp. 678–682, 2004.

[167] P. Nasarre, S. Kusy, B. Constantin, V. Castellani, H. A. Drabkin, D. Bagnard, and J. Roche, “Semaphorin SEMA3F has a repulsing activity on breast cancer cells and inhibits E-cadherin-mediated cell adhesion.,” *Neoplasia*, vol. 7, no. 2, pp. 180–189, 2005.

[168] P. C. Letourneau, “Cell-to-substratum adhesion and guidance of axonal elongation.,” *Developmental Biology*, vol. 44, no. 1, pp. 92–101, 1975.

[169] J. A. Hammarback and P. C. Letourneau, “Neurite extension across regions of low cell-substratum adhesivity: implications for the guidepost hypothesis of axonal pathfinding.,” *Developmental Biology*, vol. 117, no. 2, pp. 655–662, 1986.

[170] J. Walter, S. Henke-Fahle, and F. Bonhoeffer, “Avoidance of posterior tectal membranes by temporal retinal axons,” *Development*, vol. 101, no. 4, pp. 909–913, 1987.

[171] J. Walter, B. Kern-Veits, J. Huf, B. Stolze, and F. Bonhoeffer, “Recognition of position-specific properties of tectal cell membranes by retinal axons in vitro.,” *Development*, vol. 101, no. 4, pp. 685–696, 1987.

[172] H. Baier and F. Bonhoeffer, “Axon guidance by gradients of a target-derived component.,” *Science*, vol. 255, no. 5043, pp. 472–475, 1992.

[173] S. M. Rosentreter, R. W. Davenport, J. Löschinger, J. Huf, J. Jung, and F. Bonhoeffer, “Response of retinal ganglion cell axons to striped linear gradients of repellent guidance molecules.,” *Journal of Neurobiology*, vol. 37, no. 4, pp. 541–562, 1998.

[174] B. Knöll, C. Weinl, A. Nordheim, and F. Bonhoeffer, “Stripe assay to examine axonal guidance and cell migration.,” *Nature Protocols*, vol. 2, no. 5, pp. 1216–1224, 2007.

[175] F. Mann, V. Zhukareva, A. Pimenta, P. Levitt, and J. Bolz, “Membrane-associated molecules guide limbic and nonlimbic thalamocortical projections,” *Journal of Neuroscience*, vol. 18, no. 22, pp. 9409–9419, 1998.

[176] B. Knöll, K. Zarbalis, W. Wurst, and U. Drescher, “A role for the EphA family in the topographic targeting of vomeronasal axons.,” *Development*, vol. 128, no. 6, pp. 895–906, 2001.

[177] B. Knöll, O. Kretz, C. Fiedler, S. Alberti, G. Schütz, M. Frotscher, and A. Nordheim, "Serum response factor controls neuronal circuit assembly in the hippocampus.," *Nature Neuroscience*, vol. 9, no. 2, pp. 195–204, 2006.

[178] F. Turcu, K. Tratsk-Nitz, S. Thanos, W. Schuhmann, and P. Heiduschka, "Ink-jet printing for micropattern generation of laminin for neuronal adhesion," *Journal of Neuroscience Methods*, vol. 131, no. 1-2, pp. 141–148, 2003.

[179] P. Gustavsson, F. Johansson, M. Kanje, L. Wallman, and C. Eriksson Linsmeier, "Neurite guidance on protein micropatterns generated by a piezoelectric microdispenser," *Biomaterials*, vol. 28, no. 6, pp. 1141–1151, 2007.

[180] A. C. von Philipsborn, S. Lang, J. Loeschinger, A. Bernard, C. David, D. Lehnert, F. Bonhoeffer, and M. Bastmeyer, "Growth cone navigation in substrate-bound ephrin gradients," *Development*, vol. 133, no. 13, pp. 2487–2495, 2006.

[181] S. K. W. Dertinger, X. Jiang, Z. Li, V. N. Murthy, and G. M. Whitesides, "Gradients of substrate-bound laminin orient axonal specification of neurons.," *Proceedings of the National Academy of Sciences of the United States of America*, vol. 99, no. 20, pp. 12542–12547, 2002.

[182] C. B. Herbert, T. L. McLernon, C. L. Hypolite, D. N. Adams, L. Pikus, C. C. Huang, G. B. Fields, P. C. Letourneau, M. D. Distefano, and W. S. Hu, "Micropatterning gradients and controlling surface densities of photoactivatable biomolecules on self-assembled monolayers of oligo(ethylene glycol) alkanethiolates.," *Chemistry & Biology*, vol. 4, no. 10, pp. 731–737, 1997.

[183] D. Adams, E. Kao, C. Hypolite, M. Distefano, W. Hu, and P. Letourneau, "Growth cones turn and migrate up an immobilized gradient of the laminin IKVAV peptide," *Journal of Neurobiology*, vol. 62, no. 1, pp. 134–147, 2005.

[184] L. M. Y. Yu, J. H. Wosnick, and M. S. Shoichet, "Miniaturized system of neurotrophin patterning for guided regeneration," *Journal of Neuroscience Methods*, vol. 171, no. 2, pp. 253–263, 2008.

[185] J. M. Bélisle, J. P. Correia, P. W. Wiseman, T. E. Kennedy, and S. Costantino, “Patterning protein concentration using laser-assisted adsorption by photobleaching, LAPAP.,” *Lab on a Chip*, vol. 8, no. 12, pp. 2164–2167, 2008.

[186] S. H. Lee, J. J. Moon, and J. L. West, “Three-dimensional micropatterning of bioactive hydrogels via two-photon laser scanning photolithography for guided 3D cell migration,” *Biomaterials*, vol. 29, no. 20, pp. 2962–2968, 2008.

[187] G. M. Whitesides, “The origins and the future of microfluidics.,” *Nature*, vol. 442, pp. 368–373, 2006.

[188] N. Li Jeon, H. Baskaran, S. K. W. Dertinger, G. M. Whitesides, L. Van de Water, and M. Toner, “Neutrophil chemotaxis in linear and complex gradients of interleukin-8 formed in a microfabricated device.,” *Nature Biotechnology*, vol. 20, no. 8, pp. 826–830, 2002.

[189] K. T. Kotz, W. Xiao, C. Miller-Graziano, W.-J. Qian, A. Russom, E. A. Warner, L. L. Moldawer, A. De, P. E. Bankey, B. O. Petritis, D. G. Camp, A. E. Rosenbach, J. Goverman, S. P. Fagan, B. H. Brownstein, D. Irimia, W. Xu, J. Wilhelmy, M. N. Mindrinos, R. D. Smith, R. W. Davis, R. G. Tompkins, and M. Toner, “Clinical microfluidics for neutrophil genomics and proteomics.,” *Nature Medicine*, vol. 16, no. 9, pp. 1042–1047, 2010.

[190] L. Song, S. M. Nadkarni, H. U. Bödeker, C. Beta, A. Bae, C. Franck, W. J. Rappel, W. F. Loomis, and E. Bodenschatz, “Dictyostelium discoideum chemotaxis: Threshold for directed motion,” *European Journal of Cell Biology*, vol. 85, no. 9-10, pp. 981–989, 2006.

[191] D. I. Cattoni, J. B. Fiche, A. Valeri, T. Mignot, and M. Nöllmann, “Super-Resolution Imaging of Bacteria in a Microfluidics Device,” *PLoS ONE*, vol. 8, no. 10, 2013.

[192] G. M. Walker, M. S. Ozers, and D. J. Beebe, “Cell infection within a microfluidic device using virus gradients,” *Sensors and Actuators, B: Chemical*, vol. 98, no. 2-3, pp. 347–355, 2004.

[193] H. Zhang, T. Xu, C. W. Li, and M. Yang, “A microfluidic device with microbead array for sensitive virus detection and genotyping using quantum dots as fluorescence labels,” *Biosensors and Bioelectronics*, vol. 25, no. 11, pp. 2402–2407, 2010.

[194] W. Saadi, S. J. Wang, F. Lin, and N. L. Jeon, "A parallel-gradient microfluidic chamber for quantitative analysis of breast cancer cell chemotaxis," *Biomedical Microdevices*, vol. 8, no. 2, pp. 109–118, 2006.

[195] A.-E. Saliba, L. Saias, E. Psychari, N. Minc, D. Simon, F.-C. Bidard, C. Mathiot, J.-Y. Pierga, V. Fraisier, J. Salamero, V. Saada, F. Farace, P. Vielh, L. Malaquin, and J.-L. Viovy, "Microfluidic sorting and multimodal typing of cancer cells in self-assembled magnetic arrays.," *Proceedings of the National Academy of Sciences of the United States of America*, vol. 107, no. 33, pp. 14524–14529, 2010.

[196] B. G. Chung, L. A. Flanagan, S. W. Rhee, P. H. Schwartz, A. P. Lee, E. S. Monuki, and N. L. Jeon, "Human neural stem cell growth and differentiation in a gradient-generating microfluidic device.," *Lab on a Chip*, vol. 5, no. 4, pp. 401–406, 2005.

[197] K.-I. Kamei, S. Guo, Z. T. F. Yu, H. Takahashi, E. Gschweng, C. Suh, X. Wang, J. Tang, J. McLaughlin, O. N. Witte, K.-B. Lee, and H.-R. Tseng, "An integrated microfluidic culture device for quantitative analysis of human embryonic stem cells.," *Lab on a Chip*, vol. 9, no. 4, pp. 555–563, 2009.

[198] B. S. Cho, T. G. Schuster, X. Zhu, D. Chang, G. D. Smith, and S. Takayama, "Passively driven integrated microfluidic system for separation of motile sperm," *Analytical Chemistry*, vol. 75, no. 7, pp. 1671–1675, 2003.

[199] D. B. Seo, Y. Agca, Z. C. Feng, and J. K. Critser, "Development of sorting, aligning, and orienting motile sperm using microfluidic device operated by hydrostatic pressure," *Microfluidics and Nanofluidics*, vol. 3, no. 5, pp. 561–570, 2007.

[200] J. Wang, L. Ren, L. Li, W. Liu, J. Zhou, W. Yu, D. Tong, and S. Chen, "Microfluidics: a new cosset for neurobiology.," *Lab on a Chip*, vol. 9, no. 5, pp. 644–652, 2009.

[201] L. J. Millet and M. U. Gillette, "New perspectives on neuronal development via microfluidic environments," *Trends in Neurosciences*, vol. 35, pp. 752–761, 2012.

[202] J. Mai, L. Fok, H. Gao, X. Zhang, and M.-M. Poo, "Axon initiation and growth cone turning on bound protein gradients.," *Journal of Neuroscience*, vol. 29, no. 23, pp. 7450–7458, 2009.

[203] J. C. Wang, X. Li, B. Lin, S. Shim, G.-L. Ming, and A. Levchenko, "A microfluidics-based turning assay reveals complex growth cone responses to integrated gradients of substrate-bound ECM molecules and diffusible guidance cues.," *Lab on a Chip*, vol. 8, pp. 227–237, 2008.

[204] S. K. W. Dertinger, D. T. Chiu, Noo Li Jeon, and G. M. Whitesides, "Generation of gradients having complex shapes using microfluidic networks," *Analytical Chemistry*, vol. 73, pp. 1240–1246, 2001.

[205] B. M. Friedrich and F. Jülicher, "Chemotaxis of sperm cells.," *Proceedings of the National Academy of Sciences of the United States of America*, vol. 104, no. 33, pp. 13256–13261, 2007.

[206] H. C. Berg and E. M. Purcell, "Physics of chemoreception.," *Biophysical Journal*, vol. 20, no. 2, pp. 193–219, 1977.

[207] W. Bialek and S. Setayeshgar, "Physical limits to biochemical signaling.," *Proceedings of the National Academy of Sciences of the United States of America*, vol. 102, no. 29, pp. 10040–10045, 2005.

[208] M. Ueda and T. Shibata, "Stochastic signal processing and transduction in chemotactic response of eukaryotic cells.," *Biophysical Journal*, vol. 93, no. July, pp. 11–20, 2007.

[209] H. Nguyen, P. Dayan, and G. J. Goodhill, "The influence of receptor positioning on chemotactic information.," *Journal of Theoretical Biology*, pp. 1–7, 2014.

[210] K. G. N. Suzuki, "Lipid rafts generate digital-like signal transduction in cell plasma membranes," *Biotechnology Journal*, vol. 7, no. 6, pp. 753–761, 2012.

[211] S. C. Shibata, K. Hibino, T. Mashimo, T. Yanagida, and Y. Sako, "Formation of signal transduction complexes during immobile phase of NGFR movements," *Biochemical and Biophysical Research Communications*, vol. 342, pp. 316–322, 2006.

[212] A. Callegari, S. Luin, L. Marchetti, A. Duci, A. Cattaneo, and F. Beltram, "Single particle tracking of acyl carrier protein (ACP)-tagged TrkA receptors in PC12nnr5 cells," *Journal of Neuroscience Methods*, vol. 204, no. 1, pp. 82–86, 2012.

[213] L. Marchetti, A. Callegari, S. Luin, G. Signore, A. Viegi, F. Beltram, and A. Cattaneo, "Ligand signature in the membrane dynamics of single TrkA receptor molecules.," *Journal of Cell Science*, vol. 126, no. Pt 19, pp. 4445–56, 2013.

[214] Y. Miyanaga, S. Matsuoka, and M. Ueda, "Single-molecule imaging techniques to visualize chemotactic signaling events on the membrane of living Dictyostelium cells.," *Methods in Molecular Biology*, vol. 571, pp. 417–35, 2009.

[215] B. Treanor, D. Depoil, A. Gonzalez-Granja, P. Barral, M. Weber, O. Dushek, A. Bruckbauer, and F. D. Batista, "The Membrane Skeleton Controls Diffusion Dynamics and Signaling through the B Cell Receptor," *Immunity*, vol. 32, no. 2, pp. 187–199, 2010.

[216] D. Mortimer, P. Dayan, K. Burrage, and G. J. Goodhill, "Optimizing chemotaxis by measuring unbound-bound transitions," *Physica D: Nonlinear Phenomena*, vol. 239, no. 9, pp. 477–484, 2010.

[217] D. Fuller, W. Chen, M. Adler, A. Groisman, H. Levine, W.-J. Rappel, and W. F. Loomis, "External and internal constraints on eukaryotic chemotaxis.," *Proceedings of the National Academy of Sciences of the United States of America*, vol. 107, no. 21, pp. 9656–9659, 2010.

[218] R. G. Endres and N. S. Wingreen, "Maximum likelihood and the single receptor," *Physical Review Letters*, vol. 103, no. 15, pp. 1–4, 2009.

[219] T. Mora and N. S. Wingreen, "Limits of sensing temporal concentration changes by single cells," *Physical Review Letters*, vol. 104, no. JUNE, pp. 1–4, 2010.

[220] V. Tolmachev, Z. Varasteh, H. Honarvar, S. Hosseinimehr, O. Eriksson, P. Jonasson, F. Frejd, L. Abrahmsen, and A. Orlova, "Imaging of platelet-derived growth factor receptor beta expression in glioblastoma xenografts using affibody molecule 111In-DOTA-Z09591," *Journal of Nuclear Medicine*, vol. 55, pp. 294–300, 2014.

[221] P. Ljungquist-Hoddelius, M. Lirvall, A. Wasteson, and K. E. Magnusson, "Lateral diffusion of PDGF beta-receptors in human fibroblasts," *Bioscience Reports*, vol. 11, no. 1, pp. 43–52, 1991.

[222] B. N. Kholodenko, O. V. Demin, G. Moehren, and J. B. Hoek, "Quantification of short term signaling by the epidermal growth factor receptor.," *Journal of Biological Chemistry*, vol. 274, no. 42, pp. 30169–30181, 1999.

[223] Hiroshima and Sako, "Single-Molecule Kinetic Analysis of Receptor Protein Tyrosine Kinases," *Cell Signaling Reactions*, pp. 1–32, 2011.

[224] S. T. Low-Nam, K. A. Lidke, P. J. Cutler, R. C. Roovers, P. M. P. van Bergen en Henegouwen, B. S. Wilson, and D. S. Lidke, "ErbB1 dimerization is promoted by domain co-confinement and stabilized by ligand binding.," *Nature Structural & Molecular Biology*, vol. 18, no. 11, pp. 1244–9, 2011.

[225] F. van Hemert, M. D. Lazova, B. E. Snaar-Jagaska, and T. Schmidt, "Mobility of G proteins is heterogeneous and polarized during chemotaxis.," *Journal of Cell Science*, vol. 123, no. Pt 17, pp. 2922–2930, 2010.

[226] C. Bouzigues, M. Morel, A. Triller, and M. Dahan, "Asymmetric redistribution of GABA receptors during GABA gradient sensing by nerve growth cones analyzed by single quantum dot imaging.," *Proceedings of the National Academy of Sciences of the United States of America*, vol. 104, no. 27, pp. 11251–11256, 2007.

[227] G. Orr, D. Hu, S. Ozçelik, L. K. Opresko, H. S. Wiley, and S. D. Colson, "Cholesterol dictates the freedom of EGF receptors and HER2 in the plane of the membrane.," *Biophysical Journal*, vol. 89, no. 2, pp. 1362–1373, 2005.

[228] G. Iyengar and M. Rao, "A cellular solution to an information-processing problem.," *Proceedings of the National Academy of Sciences of the United States of America*, vol. 111, no. 34, pp. 1406608111–, 2014.

[229] B. W. Andrews and P. a. Iglesias, "An information-theoretic characterization of the optimal gradient sensing response of cells," *PLoS Computational Biology*, vol. 3, no. 8, pp. 1489–1497, 2007.

[230] D. Mortimer, P. Dayan, K. Burrage, and G. J. Goodhill, "Bayes-optimal chemotaxis.," *Neural Computation*, vol. 23, no. 2, pp. 336–373, 2011.

[231] H. Mao, P. S. Cremer, and M. D. Manson, "A sensitive, versatile microfluidic assay for bacterial chemotaxis.," *Proceedings of the National Academy of Sciences of the United States of America*, vol. 100, no. 9, pp. 5449–54, 2003.

[232] Z. Xiao, N. Zhang, D. B. Murphy, and P. N. Devreotes, "Dynamic distribution of chemoattractant receptors in living cells during chemotaxis and persistent stimulation," *Journal of Cell Biology*, vol. 139, no. 2, pp. 365–374, 1997.

[233] G. Servant, O. D. Weiner, E. R. Neptune, J. W. Sedat, and H. R. Bourne, "Dynamics of a chemoattractant receptor in living neutrophils during chemotaxis.," *Molecular biology of the cell*, vol. 10, no. 4, pp. 1163–1178, 1999.

[234] M. Bailly, J. Wyckoff, B. Bouzahzah, R. Hammerman, V. Sylvestre, M. Cammer, R. Pestell, and J. E. Segall, "Epidermal growth factor receptor distribution during chemotactic responses.," *Molecular Biology of the Cell*, vol. 11, no. 11, pp. 3873–83, 2000.

[235] C. Guirland, S. Suzuki, M. Kojima, B. Lu, and J. Q. Zheng, "Lipid rafts mediate chemotropic guidance of nerve growth cones," *Neuron*, vol. 42, no. 1, pp. 51–62, 2004.

[236] J. Yang, "Directional sensing by cooperative chemoreceptor arrays modeled as Monod-Wyman-Changeux clusters," *Physical Review E - Statistical, Nonlinear, and Soft Matter Physics*, vol. 87, pp. 1–9, 2013.

[237] V. Sourjik, "Receptor clustering and signal processing in E. coli chemotaxis," *Trends in Microbiology*, vol. 12, no. 12, pp. 569–576, 2004.

[238] G. Aquino, D. Clausznitzer, S. Tollis, and R. G. Endres, "Optimal receptor-cluster size determined by intrinsic and extrinsic noise," *Physical Review E - Statistical, Nonlinear, and Soft Matter Physics*, vol. 83, no. 2, pp. 22–24, 2011.

[239] T. Shibata and M. Ueda, "Noise generation, amplification and propagation in chemotactic signaling systems of living cells.," *BioSystems*, vol. 93, no. 1-2, pp. 126–32, 2008.

[240] Z. Pujic, C. E. Giacomantonio, D. Unni, W. J. Rosoff, and G. J. Goodhill, "Analysis of the growth cone turning assay for studying axon guidance," *Journal of Neuroscience Methods*, vol. 170, pp. 220–228, 2008.

[241] P. T. Yam, S. D. Langlois, S. Morin, and F. Charron, “Sonic Hedgehog Guides Axons through a Noncanonical, Src-Family-Kinase-Dependent Signaling Pathway,” *Neuron*, vol. 62, pp. 349–362, 2009.

[242] C. R. Kothapalli, E. van Veen, S. de Valence, S. Chung, I. K. Zervantonakis, F. B. Gertler, and R. D. Kamm, “A high-throughput microfluidic assay to study neurite response to growth factor gradients.,” *Lab on a Chip*, vol. 11, pp. 497–507, 2011.

[243] M. Morel, V. Shynkar, J. C. Galas, I. Dupin, C. Bouzigues, V. Studer, and M. Dahan, “Amplification and temporal filtering during gradient sensing by nerve growth cones probed with a microfluidic assay,” *Biophysical Journal*, vol. 103, pp. 1648–1656, 2012.

[244] H. Lu, L. Y. Koo, W. M. Wang, D. A. Lauffenburger, L. G. Griffith, and K. F. Jensen, “Microfluidic shear devices for quantitative analysis of cell adhesion,” *Analytical Chemistry*, vol. 76, no. 18, pp. 5257–5264, 2004.

[245] M. A. Day, “The no-slip condition of fluid dynamics,” *Erkenntnis*, vol. 33, no. 3, pp. 285–296, 1990.

[246] N. Bhattacharjee, N. Li, T. M. Keenan, and A. Folch, “A neuron-benign microfluidic gradient generator for studying the response of mammalian neurons towards axon guidance factors.,” *Integrative Biology*, vol. 2, no. 11-12, pp. 669–79, 2010.

[247] K. Campbell and A. Groisman, “Generation of complex concentration profiles in microchannels in a logarithmically small number of steps.,” *Lab on a Chip*, vol. 7, no. 2, pp. 264–272, 2007.

[248] D. H. Geschwind and P. Levitt, “Autism spectrum disorders: developmental disconnection syndromes,” *Current Opinion in Neurobiology*, vol. 17, pp. 103–111, 2007.

[249] L. Lin, T. G. Lesnick, D. M. Maraganore, and O. Isacson, “Axon guidance and synaptic maintenance: preclinical markers for neurodegenerative disease and therapeutics,” *Trends in Neurosciences*, vol. 32, pp. 142–149, 2009.

[250] E. T. Stoeckli, “What does the developing brain tell us about neural diseases?,” *European Journal of Neuroscience*, vol. 35, pp. 1811–1817, 2012.

[251] A. L. Kolodkin and M. Tessier-Lavigne, “Mechanisms and molecules of neuronal wiring: A primer,” *Cold Spring Harbor Perspectives in Biology*, vol. 3, pp. 1–14, 2011.

[252] G.-l. Ming, S. T. Wong, J. Henley, X.-b. Yuan, H.-j. Song, N. C. Spitzer, and M.-m. Poo, “Adaptation in the chemotactic guidance of nerve growth cones.,” *Nature*, vol. 417, pp. 411–418, 2002.

[253] A. W. Thompson, Z. Pujic, L. J. Richards, and G. J. Goodhill, “Cyclic nucleotide-dependent switching of mammalian axon guidance depends on gradient steepness,” *Molecular and Cellular Neuroscience*, vol. 47, pp. 45–52, 2011.

[254] C. B. Kent, T. Shimada, G. B. Ferraro, B. Ritter, P. T. Yam, P. S. McPherson, F. Charron, T. E. Kennedy, and A. E. Fournier, “14-3-3 proteins regulate protein kinase a activity to modulate growth cone turning responses.,” *Journal of Neuroscience*, vol. 30, pp. 14059–14067, 2010.

[255] I. Dudanova, G. Gatto, and R. Klein, “GDNF acts as a chemoattractant to support ephrina-induced repulsion of limb motor axons,” *Current Biology*, vol. 20, pp. 2150–2156, 2010.

[256] C. Ruiz de Almodovar, P. J. Fabre, E. Knevels, C. Coulon, I. Segura, P. C. G. Haddick, L. Aerts, N. Delattin, G. Strasser, W. J. Oh, C. Lange, S. Vinckier, J. Haigh, C. Fouquet, C. Gu, K. Alitalo, V. Castellani, M. Tessier-Lavigne, A. Chedotal, F. Charron, and P. Carmeliet, “VEGF Mediates Commissural Axon Chemoattraction through Its Receptor Flk1,” *Neuron*, vol. 70, pp. 966–978, 2011.

[257] I. Dudanova, T.-J. Kao, J. E. Herrmann, B. Zheng, A. Kania, and R. Klein, “Genetic Evidence for a Contribution of EphA:EphrinA Reverse Signaling to Motor Axon Guidance,” *Journal of Neuroscience*, vol. 32, pp. 5209–5215, 2012.

[258] A. M. Taylor, S. Menon, and S. L. Gupton, “Passive microfluidic chamber for long-term imaging of axon guidance in response to soluble gradients,” *Lab Chip*, vol. 15, pp. 2781–2789, 2015.

[259] T. F. W. Sloan, M. A. Qasaimeh, D. Juncker, and P. T. Yam, “Integration of Shallow Gradients of Shh and Netrin-1 Guides Commissural Axons,” *PLoS Biology*, vol. 13, no. 3, p. e1002119, 2015.

[260] D. Bray, “Branching patterns of individual sympathetic neurons in culture.,” *Journal of Cell Biology*, vol. 56, pp. 702–712, 1973.

[261] D. Bray, “Mechanical tension produced by nerve cells in tissue culture.,” *Journal of Cell Science*, vol. 37, pp. 391–410, 1979.

[262] D. Bray, “Axonal growth in response to experimentally applied mechanical tension.,” *Developmental Biology*, vol. 102, pp. 379–389, 1984.

[263] J. Zheng, P. Lamoureux, V. Santiago, T. Dennerll, R. E. Buxbaum, and S. R. Heidemann, “Tensile regulation of axonal elongation and initiation.,” *Journal of Neuroscience*, vol. 11, pp. 1117–1125, 1991.

[264] K. Franze and J. Guck, “The biophysics of neuronal growth,” *Reports on Progress in Physics*, vol. 73, no. 9, p. 094601, 2010.

[265] T. Betz, D. Koch, Y.-B. Lu, K. Franze, and J. A. Käs, “Growth cones as soft and weak force generators.,” *Proceedings of the National Academy of Sciences of the United States of America*, vol. 108, no. 33, pp. 13420–13425, 2011.

[266] A. I. Athamneh and D. M. Suter, “Quantifying mechanical force in axonal growth and guidance,” *Frontiers in Cellular Neuroscience*, 2015.

[267] I. Kaverina, O. Krylyshkina, and J. V. Small, “Regulation of substrate adhesion dynamics during cell motility,” *International Journal of Biochemistry and Cell Biology*, vol. 34, no. 7, pp. 746–761, 2002.

[268] E. A. Codling, M. J. Plank, and S. Benhamou, “Random walk models in biology.,” *Journal of the Royal Society Interface*, vol. 5, pp. 813–834, 2008.

[269] C. Wetmore and L. Olson, “Neuronal and nonneuronal expression of neurotrophins and their receptors in sensory and sympathetic ganglia suggest new intercellular trophic interactions.,” *Journal of Comparative Neurology*, vol. 353, no. 1, pp. 143–59, 1995.

[270] V. M. Verge, J. P. Merlio, J. Grondin, P. Ernfors, H. Persson, R. J. Riopelle, T. Hökfelt, and P. M. Richardson, “Colocalization of NGF binding sites, trk mRNA, and low-affinity NGF receptor mRNA in primary sensory neurons: responses to injury and infusion of NGF.,” *Journal of Neuroscience*, vol. 12, no. 10, pp. 4011–4022, 1992.

[271] T. Wehrman, X. He, B. Raab, A. Dukipatti, H. Blau, and K. C. Garcia, "Structural and mechanistic insights into nerve growth factor interactions with the TrkA and p75 receptors.," *Neuron*, vol. 53, no. 1, pp. 25–38, 2007.

[272] H. Ohta, M. Nishizuka, Y. Arai, and H. Saito, "Effect of nerve growth factor (NGF) on survival of superior cervical ganglion (SCG) transplanted into the third ventricle in rats," *Japanese Journal of Pharmacology*, vol. 53, no. 1, pp. 11–18, 1990.

[273] H. D. Simpson, E. M. Kita, E. K. Scott, and G. J. Goodhill, "A quantitative analysis of branching, growth cone turning, and directed growth in zebrafish retinotectal axon guidance," *Journal of Comparative Neurology*, vol. 521, no. 6, pp. 1409–1429, 2013.

[274] D. M. Suter and K. E. Miller, "The emerging role of forces in axonal elongation," *Progress in Neurobiology*, vol. 94, no. 2, pp. 91–101, 2011.

[275] S. Chang, V. I. Rodionov, G. G. Borisy, and S. V. Popov, "Transport and turnover of microtubules in frog neurons depend on the pattern of axonal growth.," *Journal of Neuroscience*, vol. 18, no. 3, pp. 821–9, 1998.

[276] J. Rajagopalan, A. Tofangchi, and T. a. Saif, "Drosophila neurons actively regulate axonal tension in vivo," *Biophysical Journal*, vol. 99, no. 10, pp. 3208–3215, 2010.

[277] S. R. Heidemann, P. Lamoureux, and R. E. Buxbaum, "Cytomechanics of axonal development.," *Cell Biochemistry and Biophysics*, vol. 27, no. 3, pp. 135–155, 1995.

[278] P. Letourneau, "Axonal pathfinding: Extracellular matrix role," in *Encyclopedia of Neuroscience* (L. Spire, ed.), pp. 1139–1145, Oxford: Academic Press, 2009.

[279] E. Robles and T. M. Gomez, "Focal adhesion kinase signaling at sites of integrin-mediated adhesion controls axon pathfinding.," *Nature Neuroscience*, vol. 9, no. 10, pp. 1274–1283, 2006.

[280] D. K. Cullen, J. Vukasinovic, A. Glezer, and M. C. Laplaca, "Microfluidic engineered high cell density three-dimensional neural cultures.," *Journal of Neural Engineering*, vol. 4, no. 2, pp. 159–172, 2007.

[281] D. Mortimer, *Bayesian model of axon guidance.* Phd thesis, University of Queensland, 2012.

[282] B. R. Caré and H. A. Soula, “Impact of receptor clustering on ligand binding.,” *BMC Systems Biology*, vol. 5, no. 1, p. 48, 2011.

[283] K. Kaizu, W. De Ronde, J. Paijmans, K. Takahashi, F. Tostevin, and P. R. T. Wolde, “The berg-purcell limit revisited,” *Biophysical Journal*, vol. 106, no. 4, pp. 976–985, 2014.

[284] B. Bicknell, P. Dayan, and G. J. Goodhill, “The limits of chemosensation vary across dimensions,” *Nature Communications*, vol. 6, pp. 1–8, 2015.

[285] T. Jin, N. Zhang, Y. Long, C. A. Parent, and P. N. Devreotes, “Localization of the G protein betagamma complex in living cells during chemotaxis.,” *Science*, vol. 287, no. 5455, pp. 1034–1036, 2000.

[286] P. C. Kerstein, R. H. Nichol Iv, and T. M. Gomez, “Mechanochemical regulation of growth cone motility,” *Frontiers in Cellular Neuroscience*, vol. 9, p. 244, 2015.

[287] R. O. Karlstrom, T. Trowe, and F. Bonhoeffer, “Genetic analysis of axon guidance and mapping in the zebrafish,” *Trends in Neurosciences*, vol. 20, no. 1, pp. 3–8, 1997.

[288] W. Andrews, A. Liapi, C. Plachez, L. Camurri, J. Zhang, S. Mori, F. Murakami, J. G. Parnavelas, V. Sundaresan, and L. J. Richards, “Robo1 regulates the development of major axon tracts and interneuron migration in the forebrain.,” *Development*, vol. 133, no. 11, pp. 2243–2252, 2006.

[289] D. L. Chao, L. Ma, and K. Shen, “Transient cell-cell interactions in neural circuit formation.,” *Nature Reviews. Neuroscience*, vol. 10, no. 4, pp. 262–71, 2009.

[290] I. Dudanova and R. Klein, “Integration of guidance cues: parallel signaling and crosstalk.,” *Trends in Neurosciences*, vol. 36, no. 5, pp. 295–304, 2013.

[291] E. Stein and M. Tessier-Lavigne, “Hierarchical organization of guidance receptors: silencing of netrin attraction by slit through a Robo/DCC receptor complex.,” *Science*, vol. 291, no. 5510, pp. 1928–1938, 2001.

[292] X. Cao and M. S. Shoichet, “Investigating the synergistic effect of combined neurotrophic factor concentration gradients to guide axonal growth,” *Neuroscience*, vol. 122, pp. 381–389, 2003.

[293] G.-L. Ming, H.-J. Song, B. Berninger, N. Inagaki, M. Tessier-Lavigne, and M.-M. Poo, “Phospholipase C-γ and Phosphoinositide 3-Kinase Mediate Cytoplasmic Signaling in Nerve Growth Cone Guidance,” *Neuron*, vol. 23, no. 1, pp. 139–148, 1999.

[294] C. Gebhardt, M. Bastmeyer, and F. Weth, “Balancing of ephrin/Eph forward and reverse signaling as the driving force of adaptive topographic mapping.,” *Development*, vol. 139, no. 2, pp. 335–45, 2012.

[295] A. P. Balgude, X. Yu, A. Szymanski, and R. V. Bellamkonda, “Agarose gel stiffness determines rate of DRG neurite extension in 3D cultures,” *Biomaterials*, vol. 22, no. 10, pp. 1077–1084, 2001.

[296] P. Srinivasan, I. K. Zervantonakis, and C. R. Kothapalli, “Synergistic effects of 3D ECM and chemogradients on neurite outgrowth and guidance: a simple modeling and microfluidic framework.,” *PloS One*, vol. 9, no. 6, p. e99640, 2014.